# CHAPTER-3

# RESULTS AND DISCUSSION

## 3.1. 5-arylpyrimido-[4, 5-b] quinoline-diones as corrosion inhibitors

Quinoline and aryl pyrimidine as well as their derivatives possess potential applications in the synthesis of pharmacologically active compounds. These derivatives have been used as anti-microbial, analgesic, anti-viral, anti-inflammatory, anti- HIV, anti-tubercular, anti-tumor, anti-neoplastic, anti-malaria, diuretic, cardiovascular agents DNA binding capabilities, antitumor, DNA- intercalating carrier etc. [Deshmukh *et al.* (2009); Kappe (2000); Mojtahedi *et al.* (2002)].

In view of above, the present work describes the corrosion inhibition efficiency of four 5-aryl-pyrimido [4,5-b] quinoline-dione derivatives (APQDs) on mild steel in 1 M HCl using weight loss, electrochemical impedance spectroscopy (EIS), potentiodynamic polarization, scanning electron microscopy (SEM), quantum chemical calculations and molecular dynamics simulation methods. The novelty of the work is that the 5-arylpyrimido-[4, 5-b] quinoline-diones (APQDs) and similar compounds have not been previously investigated as metallic corrosion inhibitors. Further, a careful survey of literature revealed that 5-arylpyrimido-[4, 5-b] quinoline-diones derivatives synthesized in our lab, quinoline moiety fused with aryl pyrimidine moieties showed better inhibition efficiency than quinoline [Ebenso *et al.* (2010a); Achary *et al.* (2008); Song-mei *et al.* (2007)] and aryl pyrimidine derivatives [Soltani *et al.* (2015); Caliskan and Akbas (2011); Mahgoub *et al.* (2010); Masoud *et al.* (2010)] synthesized and investigated by other researchers. The higher inhibition efficiencies of the investigated inhibitors are attributed due to the presence of aromatic rings and double bonds in addition to the several nitrogen

(N) and oxygen (O) atoms which act as adsorption centers. The choice of these compounds as corrosion inhibitors is based on the fact that they can: (a) be easily synthesized using green starting materials with high yield, (b) exhibit high inhibition efficiency even at very low concentrations, (c) strongly adsorb on metal surface through polar functional groups (-OH $-NO_2$, -CN, $-NH_2$) and aromatic rings and thereby inhibit corrosion effectively. The molecular structure, IUPAC name and abbreviation of the inhibitors used are given in Table 3.1.1.

### 3.1.1. Gravimetric measurement

The weight loss experiments on mild steel in 1M HCl in the absence and presence of different concentrations of APQDs was carried out for an immersion period of three hours at 308K. The values of weight loss parameters such as corrosion rate ($C_R$), inhibition efficiency ($\eta$%), and surface coverage ($\theta$) obtained from weight loss measurements are given in Table 3.1.2. The weight loss measurements show that $\eta$% increases with increasing concentration for all the inhibitors and attain a maximum value of 92.17% for APQD-1, 95.21% for APQD-2, 96.52% for APQD-3, and 97.82 for APQD-4, at 20 $mgL^{-1}$. Further increase in concentration did not cause any significant change in the inhibition performance suggesting that 20 $mgL^{-1}$ is the optimum concentration. The inhibitor molecules adsorb onto the metallic surface perpendicularly because of the electrostatic repulsion function at higher concentration [Jiang *et al.* (2005)]. And therefore, compared with paralleled adsorption, adsorbed inhibitor molecules with perpendicular adsorption would occupy either similar or even smaller surface area which resulted in no significant change in the inhibition performance beyond 20 $mgL^{-1}$ concentration [Satapathy *et al.* (2009); Gunasekaran and Chauhan (2004)].

**Table 3.1.1:** IUPAC name, molecular structure and abbreviation of the studied inhibitor molecules (APQDs)

| S.No. | IUPAC name of Inhibitor | chemical Structure | Abbreviation |
|---|---|---|---|
| 1 | 5-(4-nitrophenyl)-5,10-dihydropyrimido[4,5-b]quinoline-2,4(1H,3H)-dione | 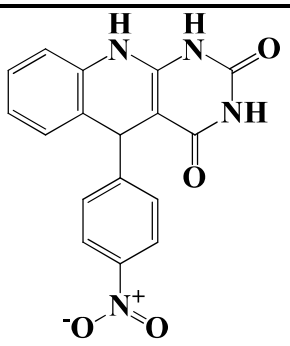 | **APQD-1** |
| 2 | 5-phenyl-5,10-dihydropyrimido[4,5-b]quinoline-2,4(1H,3H)-dione | 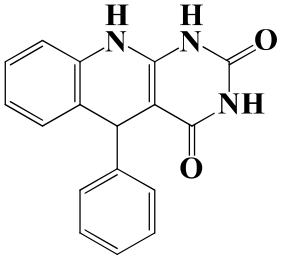 | **APQD-2** |
| 3 | 5-(4-hydroxyphenyl)-5,10-dihydropyrimido[4,5-b]quinoline-2,4(1H,3H)-dione | 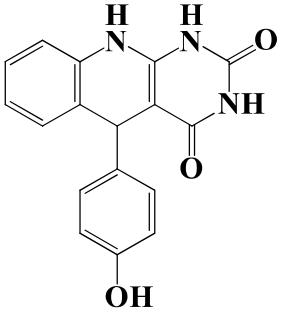 | . **APQD-3** |
| 4 | 5-(2,4-dihydroxyphenyl)-5,10-dihydropyrimido[4,5-b]quinoline-2,4(1H,3H)-dione | 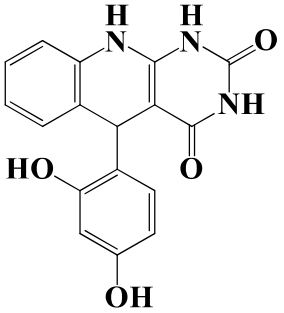 | **APQD-4** |

**Table 3.1.2:** The weight loss parameters obtained for mild steel in 1 M HCl containing different concentrations of APQDs

| Inhibitor | Conc (mg/L) | Weight loss (mg) | $C_R$ (mg $cm^{-2}$ $h^{-1}$) | Inhibition efficiency ($\eta$ %) |
|---|---|---|---|---|
| **Blank** | 0.0 | 230 | 7.66 | --- |
| **APQD-1** | 5 | 104 | 3.46 | 54.78 |
| | 10 | 50 | 1.66 | 78.26 |
| | 15 | 28 | 0.93 | 87.82 |
| | 20 | 18 | 0.60 | 92.17 |
| **APQD-2** | 5 | 88 | 2.93 | 61.73 |
| | 10 | 40 | 1.33 | 82.60 |
| | 15 | 22 | 0.73 | 90.43 |
| | 20 | 14 | 0.46 | 93.91 |
| **APQD-3** | 5 | 81 | 2.70 | 64.78 |
| | 10 | 32 | 1.06 | 86.08 |
| | 15 | 17 | 0.56 | 92.60 |
| | 20 | 11 | 0.33 | 95.65 |
| **APQD-4** | 5 | 68 | 2.26 | 70.43 |
| | 10 | 26 | 0.86 | 88.69 |
| | 15 | 13 | 0.43 | 94.34 |
| | 20 | 8 | 0.26 | 96.52 |

The increased inhibition efficiency upon increasing concentration of APQDs is attributed to increase in the extent of surface coverage by the inhibitor molecules. From the weight loss results it is observed that the inhibition efficiency of the studied APQDs follows the order: APQD-4 > APQD-3 > APQD-2 > APQD-1.

The lower inhibition efficiency of the APQD-1 could be as a result of electron withdrawing nature of the nitrophenyl group at position 5 of the pyrimido-quinoline-dione ring, which decreases the electron density on the adjacent phenyl rings. Conversely, the high inhibition performances of the APQD-3 and APQD-4 can be attributed to the electron releasing effect of the hydroxyl phenyl group(s) at position 5 of the pyrimido-quinoline-dione ring. Similar observations have been made by previously by several

authors [Yadav and Quraishi (2012); Verma *et al.* (2015a)]. The highest inhibition efficiency of APQD-4 is attributed due to the presence of two hydroxyl groups at second and fourth position of the aromatic ring of aldehydic moiety.

### 3.1.2. Effect of temperature

The influence of temperature was studied by performing the weight loss experiments in the absence and presence of optimum concentrations of the APQDs for 3 h immersion time in the temperature range of 308-338 K. The values of the inhibition efficiency ($\eta$%) and corrosion rate ($C_R$) derived from the weight loss experiments at different temperatures are presented in Table 3.1.3. From the results depicted in Table 3.1.3 it is seen that an increase in temperature causes about 20% decrease in the $\eta$% and increase in the $C_R$. The decreased $\eta$% and increased $C_R$ with increasing temperatures may due to desorption of the adsorbed inhibitor molecules leading to greater surface area of mild steel exposed to the acidic solution [Wadhwani *et al.* (2015)]. Moreover, rapid etching, desorption, and decomposition and/or rearrangement of inhibitor molecules might also be responsible for the decrease in the inhibition performance at elevated temperatures [Bai et al. (2015)].

**Table 3.1.3:** Variation of $C_R$ and $\eta$ % with temperature in absence and presence of optimum concentration of APQDs in 1M HCl

| **Temperature (K)** | **Corrosion rate ($C_R$) (mg cm$^{-2}$ h$^{-1}$) and Inhibition efficiency ($\eta$%)** | | | | | | | | | |
|---|---|---|---|---|---|---|---|---|---|---|
| | **Blank** | | **APQD-1** | | **APQD-2** | | **APQD-3** | | **APQD-4** | |
| | $C_R$ | $\eta$% | $C_R$ | $\eta$% | $C_R$ | $\eta$% | $C_R$ | $\eta$% | $C_R$ | $\eta$% |
| **308** | 7.66 | --- | 0.60 | 92.16 | 0.46 | 93.99 | 0.33 | 95.69 | 0.26 | 96.60 |
| **318** | 11.0 | --- | 1.36 | 87.63 | 1.13 | 89.72 | 0.90 | 91.81 | 0.73 | 93.36 |
| **328** | 14.3 | --- | 2.60 | 81.81 | 2.23 | 84.40 | 1.90 | 86.71 | 1.63 | 88.60 |
| **338** | 18.6 | --- | 5.20 | 72.04 | 4.73 | 74.56 | 4.46 | 76.02 | 4.06 | 78.17 |

The temperature dependency of $C_R$ can be expressed with the aid of Arrhenius equation, where the natural logarithm of $C_R$ is a linear function of $1/T$ [Verma *et al.* (2015b); Verma *et al.* (2013)]. The values of $E_a$ were calculated from the slope of Arrhenius plots ($-\Delta E_a/2.303R$) [Figure 3.1.1(a)] for all studied APQDs. The calculated values of $E_a$ were 61.52 kJmol$^{-1}$, 65.88 kJmol$^{-1}$, 73.70kJmol$^{-1}$ and 77.49 kJmol$^{-1}$ for APQD-1, APQD-2, APQD-3 and APQD-4, respectively. Obviously, the values of activation energy are higher in the presence of the APQDs ranging from 61.52 to 77.49 kJmol$^{-1}$ compared to 28.48 kJmol$^{-1}$ observed in the absence of the inhibitors. A larger increase in activation energy is observed for the more efficient inhibitor. The higher values of $E_a$ suggested that more energy barrier have been achieved in presence of inhibitors and the rate of mild steel dissolution is reduced due to the formation of inhibitors–Fe complex [Schmid and Huang 1980].

### 3.1.3. Adsorption isotherm

Adsorption isotherm is very important topic in corrosion inhibition studies for understanding the mechanism of adsorption process. The adsorption isotherms provide structural as well as thermodynamic information of the adsorbed double layer. Commonly used isotherms include Langmuir, Frumkin, and Temkin were tested among which the Langmuir isotherm showed the best fit with regression coefficient ($R^2$) values close to unity for all studied compounds. The Temkin, Frumkin, and Langmuir isotherms were tested among which the Langmuir isotherm [Figure 3.1.1(b)] gave the best fit because in this case the values of $R^2$ are most close to unity for all inhibitors whereas for Frumkin and Temkin isotherms, the values of $R^2$ were much apart from unity. Further, although the values of $R^2$ in Langmuir adsorption isotherm were close to one. However, slight deviation of the slope from unity indicated that the Langmuir isotherm could not be strictly applied.

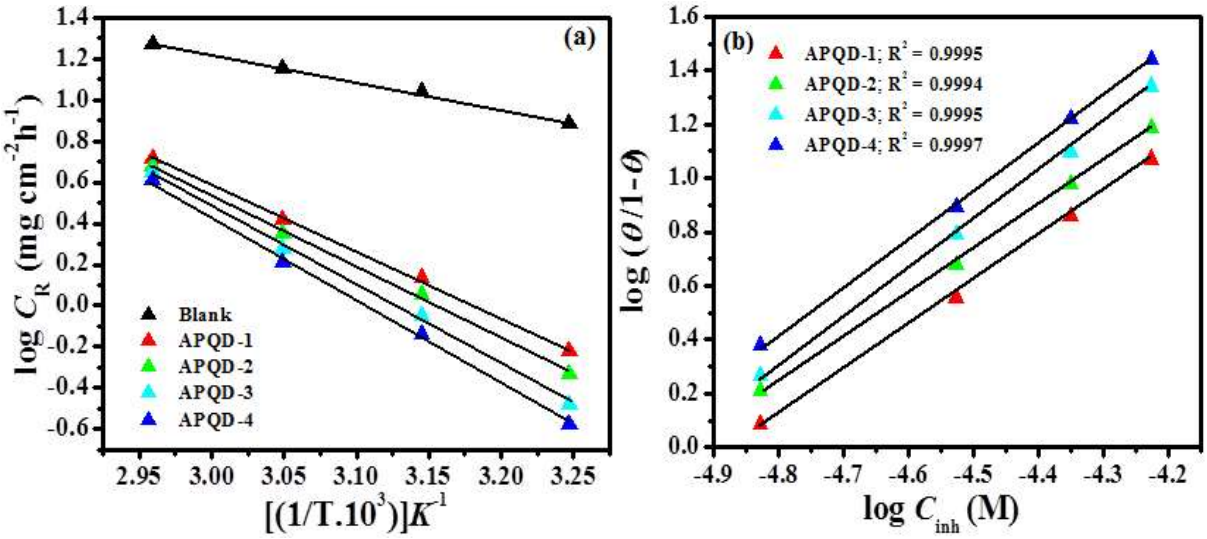


**Figure 3.1.1:** (a) Arrhenius plots for the corrosion of mild steel in 1 M HCl (b) Langmuir adsorption isotherm plots for the adsorption of APQDs on mild steel surface in 1M HCl

The deviation of slope values from unity is attributed due to intermolecular interactions of adsorbed species which causes mutual repulsion or attraction [Obot *et al.* (2009); Karthikaiselvi and Subhashini (2014)]. Moreover, the deviation of the slope could also be a result of the changes in the adsorption heat with increasing surface coverage which has not been considered during derivation of Langmuir adsorption isotherm [Oguzie *et al.* (2004; Ghareba and Omanovic (2010)]. The value of equilibrium constant, $K_{ads}$ was calculated from the intercept of the straight line of the Langmuir isotherm plots for all studied compounds at different temperatures. The calculated values of $K_{ads}$ and $\Delta G^0_{ads}$ at each studied temperature in presence of optimum concentration of APQDs are given in Table 3.1.4. In general, values of $\Delta G^0_{ads}$ up to -20 kJ mol$^{-1}$or more positive are consistent with electrostatic interactions taking place between the charged inhibitor molecules and the charged metal surface (physisorption), while those around -40 kJ mol$^{-1}$ or more negative are assumed to involve the sharing of charges between the inhibitor molecules and the metal surface to form a coordinate type of bond (chemisorption) [Goulart *et al.* (2013); Amin and Ibrahim (2011)].

**Table 3.1.4:** The values of $K_{ads}$ and $\Delta G^{\circ}_{ads}$ for mild steel in the absence and presence of optimum concentration of APQDs in 1M HCl at different temperatures

| Inhibitor | $K_{ads}$ ($10^4$ $M^{-1}$) | | | | $-\Delta G^{\circ}_{ads}$ (k $Jmol^{-1}$) | | | |
|---|---|---|---|---|---|---|---|---|
| | 308 | 318 | 328 | 338 | 308 | 318 | 328 | 338 |
| **APQD-1** | 1.60 | 0.84 | 0.54 | 0.31 | 35.09 | 34.53 | 34.40 | 33.89 |
| **APQD-2** | 1.85 | 1.04 | 0.65 | 0.35 | 35.45 | 35.09 | 34.90 | 34.25 |
| **APQD-3** | 2.63 | 1.34 | 0.78 | 0.38 | 36.36 | 35.76 | 35.42 | 34.47 |
| **APQD-4** | 3.32 | 1.67 | 0.93 | 0.43 | 36.96 | 36.35 | 35.89 | 34.81 |

In the present study, the large negative values of $\Delta G^{0}_{ads}$ (-33.31 $kJmol^{-1}$ to -38.19 kJ $mol^{-1}$) for the investigated inhibitors suggest that the inhibitors can adsorb spontaneously on mild steel surface to form highly stable adsorption film [Issaadi *et al.* (2011), Amin *et al.* (2011)]. Furthermore, the observed range of $\Delta G^{0}_{ads}$ values suggest that the adsorption of the inhibitors on mild steel surface is of "mixed mode", which implies that the adsorption of the studied inhibitors on mild steel in 1 M HCl solution involves both, physisorption and chemisorption processes [Amin *et al.* (2011); Bentiss *et al.* (2005)].

### 3.1.4. Potentiodynamic Polarization measurements

The potentiodynamic polarization measurements were undertaken in order to study the effect of investigated inhibitors (APQDs) on the anodic mild steel dissolution and cathodic hydrogen evolution reactions. The polarization curves for mild steel dissolution in the absence and presence of different concentrations of the studied inhibitors are shown in Figure 3.1.2. Extrapolation of the linear segments of cathodic and anodic Tafel curves furnished essential corrosion parameters such as corrosion potential ($E_{corr}$), corrosion current density ($i_{corr}$) and anodic and cathodic Tafel slopes ($\beta_a$ and $\beta_c$

respectively). These polarization parameters along with calculated inhibition efficiency ($\eta$%) are presented in Table 3.1.5. Examination of the results in Table 3.1.5 show that with the addition of inhibitors to the acid solution, the values of $i_{corr}$ decreases significantly with slight shift in the values of $E_{corr}$. The maximum shift in the value of $E_{corr}$ in the present study was 75 mV which is less than 85 mV. Therefore, the studied compounds can be classified as mixed-type inhibitor, which implies the inhibitors reduce the anodic mild steel dissolution and also retard the cathodic hydrogen evolution reactions [Yıldız *et al.* (2014); Mourya *et al.* (2014); Solmaz (2014)]. From the results depicted in Table 3.1.5 it is also noted that in presence of APQDs, the values of both $\beta_a$ and $\beta_c$ change irregularly but the change in values of $\beta_c$ is somewhat more prominent compared to that of $\beta_a$ suggesting that studied compounds act as mixed-type inhibitors but predominantly act as cathodic inhibitors.

**3.1.5: Electrochemical impedance spectroscopy (EIS) studies**

The effect of the synthesized compounds on the corrosion behavior of mild steel in 1 M HCl was also investigated by means of EIS method. The Nyquist plots obtained for mild steel in 1 M HCl in the absence and presence of different concentrations of the studied inhibitors are shown in Figure 3.1.3. It is obvious that the EIS spectra of the inhibitors free solution and containing inhibitors show similar characteristics suggesting that mechanism of mild steel corrosion is similar in both the cases. The impedance spectra at different concentrations of the investigated APQDs showed single capacitive loop which suggests that the adsorption of these inhibitors takes place through simple surface coverage and these corrosion inhibitors behave as primary interface inhibitors [Chevalier *et al.* (2014)].

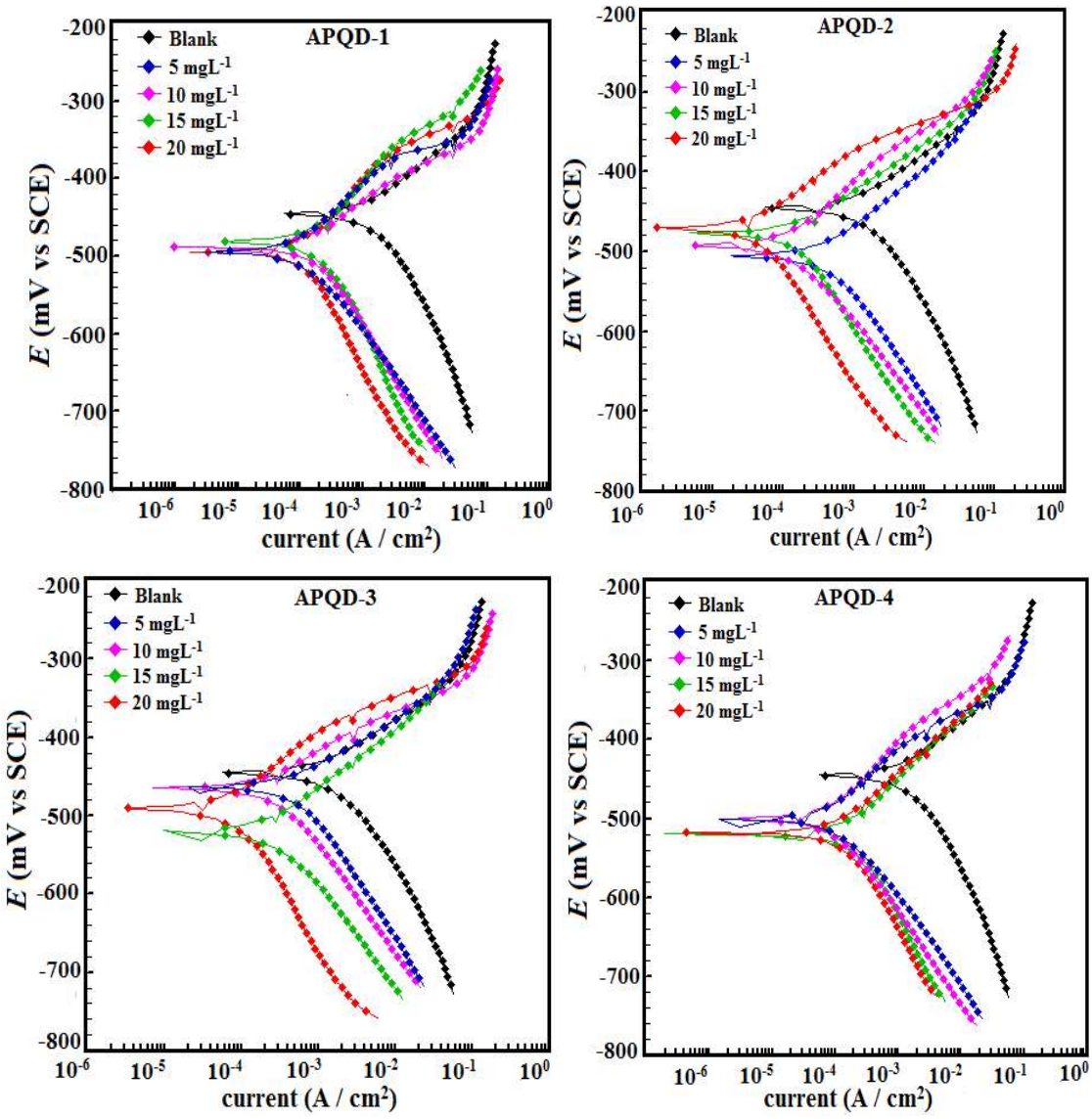


**Figure 3.1.2:** Polarization curves for mild in absence and presence of different concentrations APQDs

It is also evident from Figure 3.1.3 that the diameter of the Nyquist plots increases with increasing inhibitors concentration which is attributed to the formation of protective film on mild steel surface leading to successful retardation of the corrosion process [Eddy *et al.* (2015)]. For a metallic system corroding in acid solution, the replacement of capacitance by CPE gives a better approximation [Verma *et al.* (2015c)]. The impedance parameters were derived from the EIS spectra of the studied compounds using a

previously described equivalent circuit [Verma *et al.* (2015d)], and the results are presented in Table 3.1.6.

**Table 3.1.5:** Tafel polarization parameters for mild steel in 1 M HCl solution in absence and presence of different concentrations of APQDs

| Inhibitor | Conc mg/L | $E_{corr}$ (mV/SCE) | $\beta_a$ ($\mu A/cm^2$) | $\beta_c$ (mV/dec) | $i_{corr}$ (mV/dec) | $\eta$% |
|---|---|---|---|---|---|---|
| **Blank** | --- | -445 | 70.5 | 114.6 | 1150 | ---- |
| **APQD-1** | 5 | -492 | 83.7 | 162.3 | 489.6 | 57.42 |
| | 10 | -486 | 93.8 | 209.3 | 263.5 | 77.08 |
| | 15 | -478 | 55.6 | 100.3 | 146.4 | 87.26 |
| | 20 | -494 | 70.3 | 125.8 | 84.6 | 92.64 |
| **APQD-2** | 5 | -505 | 82.2 | 115.8 | 430.7 | 62.54 |
| | 10 | -493 | 65.9 | 156.9 | 173.4 | 84.92 |
| | 15 | -477 | 83.6 | 93.8 | 109.2 | 90.50 |
| | 20 | -471 | 71.5 | 126.7 | 58.6 | 94.90 |
| **APQD-3** | 5 | -464 | 70.5 | 111.6 | 397.3 | 65.45 |
| | 10 | -466 | 95.5 | 152.3 | 142.7 | 87.59 |
| | 15 | -521 | 53.8 | 54.7 | 78.6 | 93.16 |
| | 20 | -496 | 38.5 | 35.9 | 42.8 | 96.27 |
| **APQD-4** | 5 | -501 | 79.3 | 93.6 | 346.4 | 69.87 |
| | 10 | -505 | 94.4 | 109.3 | 132.6 | 88.46 |
| | 15 | -518 | 64.1 | 47.9 | 90.4 | 92.13 |
| | 20 | -520 | 38.5 | 35.9 | 23.7 | 97.93 |

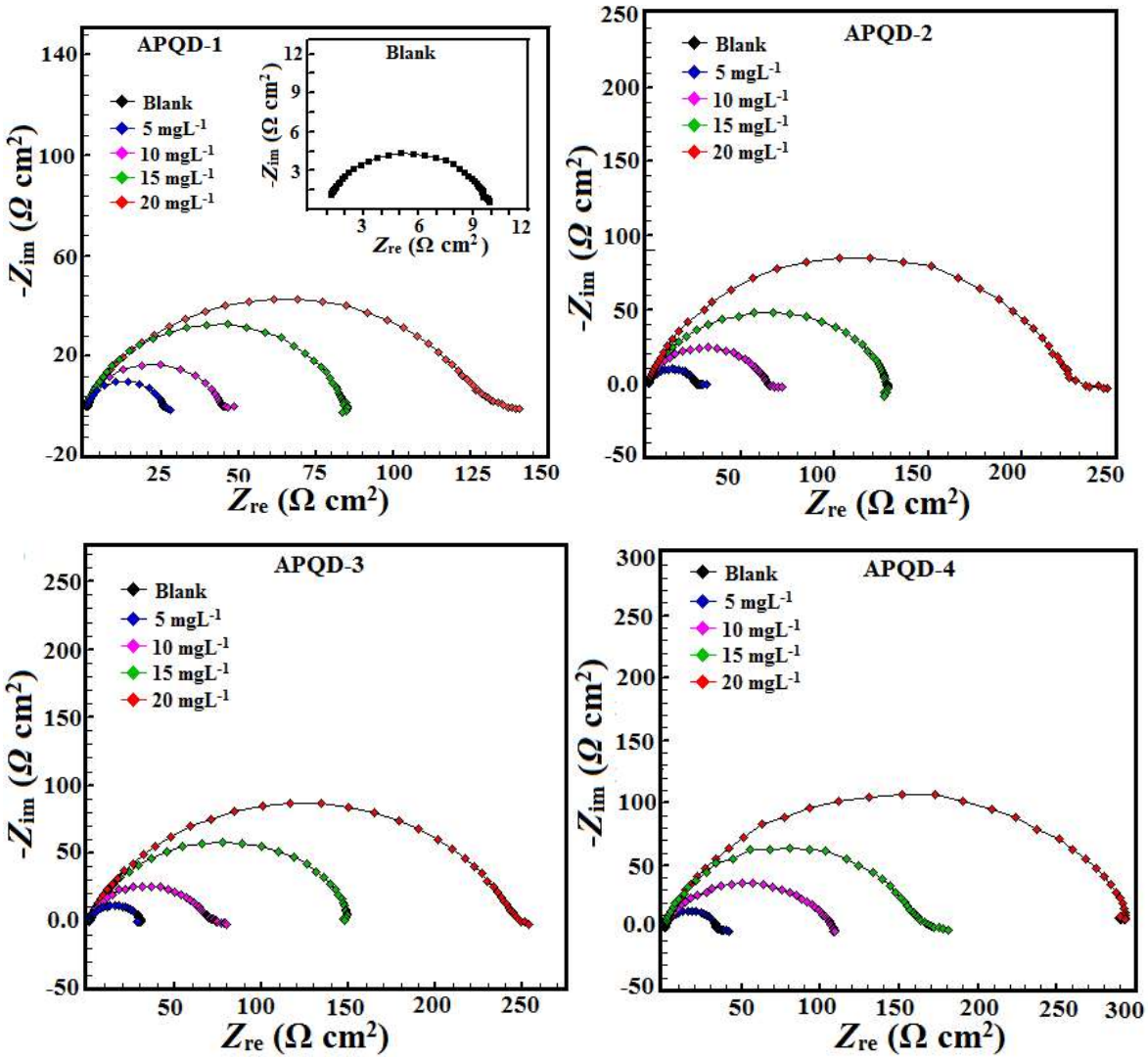


**Figure 3.1.3:** Nyquist curves for mild in absence and presence of different concentrations of APQDs

A careful inspection of the data in Table 3.1.6 reveals that the presence of different concentrations of the studied inhibitors increases the values of $R_{ct}$ which could be as a result of increased surface coverage on mild steel by the inhibitor molecules [Roy *et al.* (2014); Verma *et al.* (2015a)]. It can be observed from the results depicted in Table 3.1.6 that the values of $C_{dl}$ significantly decreased in the presence of various concentrations of the studied APQDs which could be as result of the decrease in dielectric constant and enhancement of the thickness of the electrical double layer. The values of

'*n*' are almost constant and close to unity suggesting that the interface is of capacitive characteristics.

**Table 3.1.6:** EIS parameters obtained for mild steel in 1 M HCl in absence and presence of different concentrations of APQDs

| Inh | Conc mg/L | $R_s$ ($\Omega$ cm$^2$) | $R_{ct}$ ($\Omega$ cm$^2$) | $N$ | $C_{dl}$ ($\mu F$ cm$^{-2}$) | $\eta$% |
|---|---|---|---|---|---|---|
| **Blank** | --- | 1.12 | 9.58 | 0.827 | 106.21 | ---- |
| **APQD-1** | 5 | 0.997 | 21.96 | 0.859 | 77.41 | 56.37 |
| | 10 | 0.716 | 43.34 | 0.833 | 66.65 | 77.89 |
| | 15 | 0.567 | 83.88 | 0.829 | 56.27 | 88.57 |
| | 20 | 0.608 | 129.69 | 0.857 | 22.51 | 92.61 |
| **APQD-2** | 5 | 0.844 | 25.25 | 0.837 | 56.54 | 62.05 |
| | 10 | 0.96 | 62.82 | 0.857 | 51.74 | 84.75 |
| | 15 | 0.83 | 125.67 | 0.846 | 33.12 | 92.37 |
| | 20 | 0.766 | 232.03 | 0.842 | 21.12 | 95.87 |
| **APQD-3** | 5 | 1.09 | 27.63 | 0.857 | 55.04 | 65.32 |
| | 10 | 0.976 | 69.07 | 0.846 | 43.65 | 86.13 |
| | 15 | 0.802 | 141.54 | 0.837 | 28.28 | 93.23 |
| | 20 | 0.838 | 244.56 | 0.832 | 18.11 | 96.08 |
| **APQD-4** | 5 | 0.922 | 33.42 | 0.869 | 54.56 | 71.33 |
| | 10 | 0.98 | 104.12 | 0.856 | 42.99 | 90.79 |
| | 15 | 0.82 | 166.58 | 0.842 | 24.75 | 94.24 |
| | 20 | 0.819 | 295.38 | 0.836 | 16.79 | 96.75 |

The Bode angle plots recorded for the mild steel electrode immersed in 1 M HCl in the absence and presence of various concentrations of APQDs are shown in Figure 3.1.4. As described earlier, the metal/electrolyte interface involved in present study is of a capacitive behaviour. An ideal capacitive behaviour would result if a slope value attains −1 and a phase

angle value of −90° [Ebenso *et al.* (2012a)]. However, in our present study, in the intermediate frequency zone, a linear relationship between log |*Z*| vs log *f* with a slope near −0.84 and the phase angle approaching −70° has been observed.

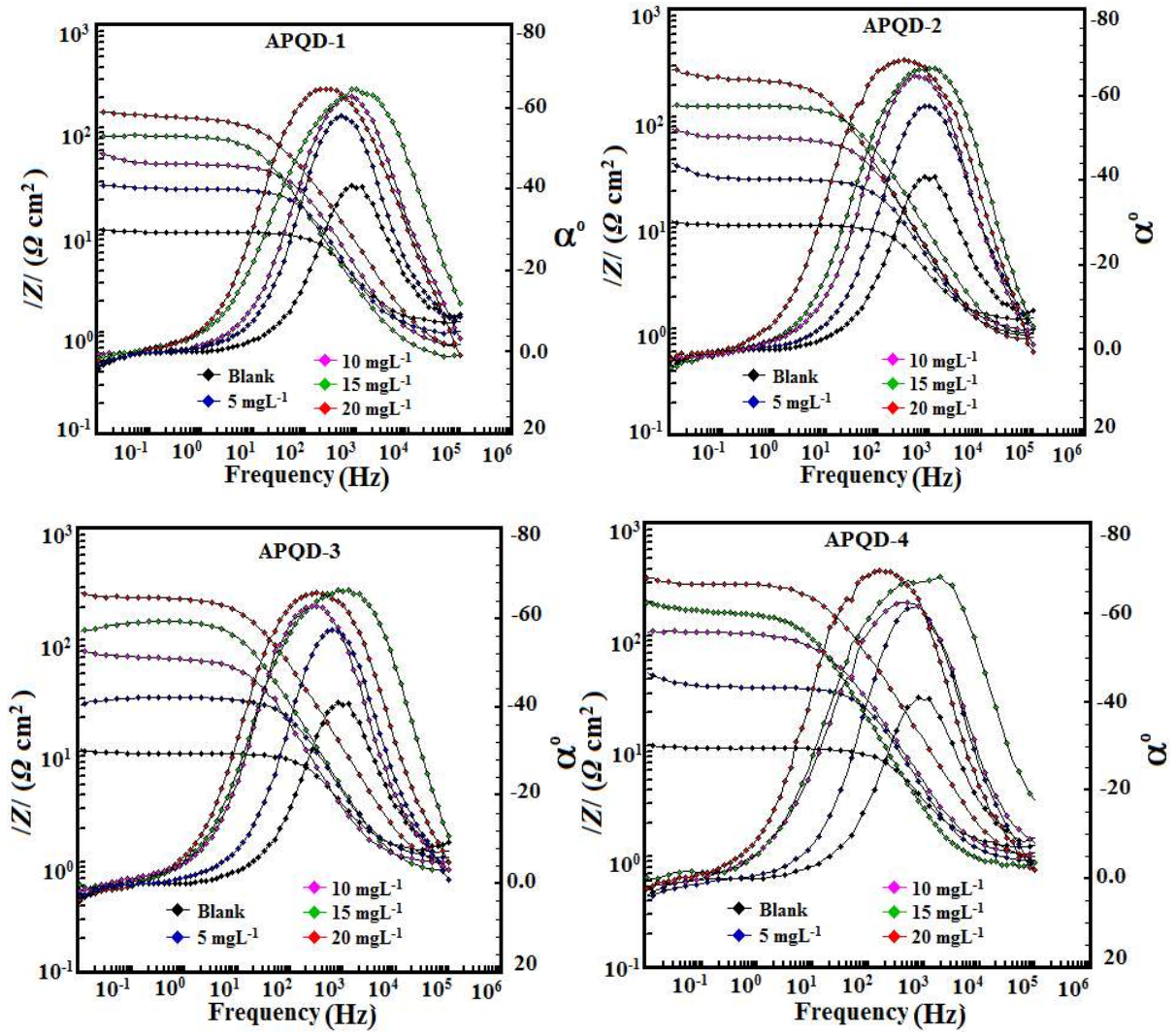


**Figure 3.1.4:** Bode impedance modulus (log *f* vs log |*Z*|) and phase angle (log *f* vs $\alpha^0$) plots for mild steel in 1 M HCl in absence and different of different concentrations of (a) APQD-1, (b) APQD-2, (c) APQD-3 and (d) APQD-4.

The deviation from the ideal capacitive behavior can be attributed to the roughness of electrode surface which occurred as a result of corrosion, and surface inhomogeneity

attributable to structural and interfacial origin. However, examination of the Bode plots depicted in Figure 3.1.4 reveals that the values of phase angle increased due to the formation of protective surface film. Furthermore, Bode plots give one time constant, sigma maxima in the intermediate frequency region. The broadening of this maximum in the Bode plots is attributed due to the adsorption and formation of protective film by inhibitors at the metal/ electrolyte interface.

**3.1.6: Scanning electron microscopy (SEM)**

The SEM images of mild steel specimens exposed to 1 M HCl for 3 h in the absence and presence of optimum concentration of the investigated inhibitors are shown in Figure 3.1.5. It can be seen from Figure 3.1.5(a) that the mild steel surface was badly corroded and damaged due to free acid attack. However, in presence of the studied inhibitors, the metallic surfaces are smother and less (Figure 3.1.5(b-e)). The improved morphology of the mild steel surface is attributed to the formation of protective film by the inhibitors over the metallic surface. This observation suggests that the APQDs used as corrosion inhibitors in the present study adsorb on mild steel surface and protect mild steel specimens from corrosion.

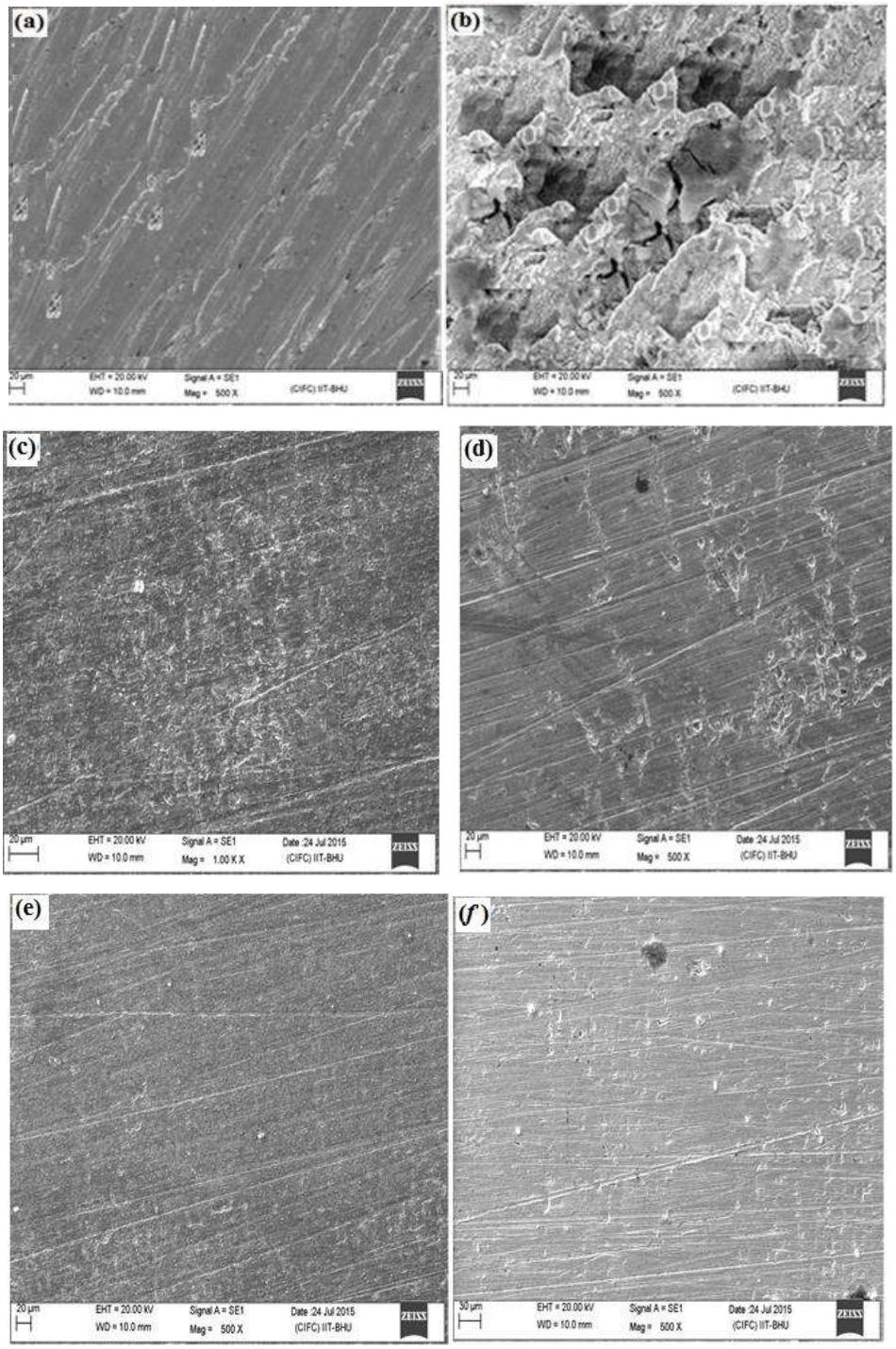


**Figure 3.1.5:** SEM images of mild steel surfaces: abraded (a), in 1 M HCl in the absence of APQDs (b), and in 1 M HCl in the presence of 20 $mgL^{-1}$ of APQD-1 (c), APQD-2 (d), APQD-3 (e) and APQD-4 (f)

### 3.1.7: Atomic force microscopy (AFM) study

Figure 3.1.6 and Figure 3.1.6 (b-e) show AFM image of mild steel surface in the absence and presence of optimum concentration of studied inhibitors, respectively.

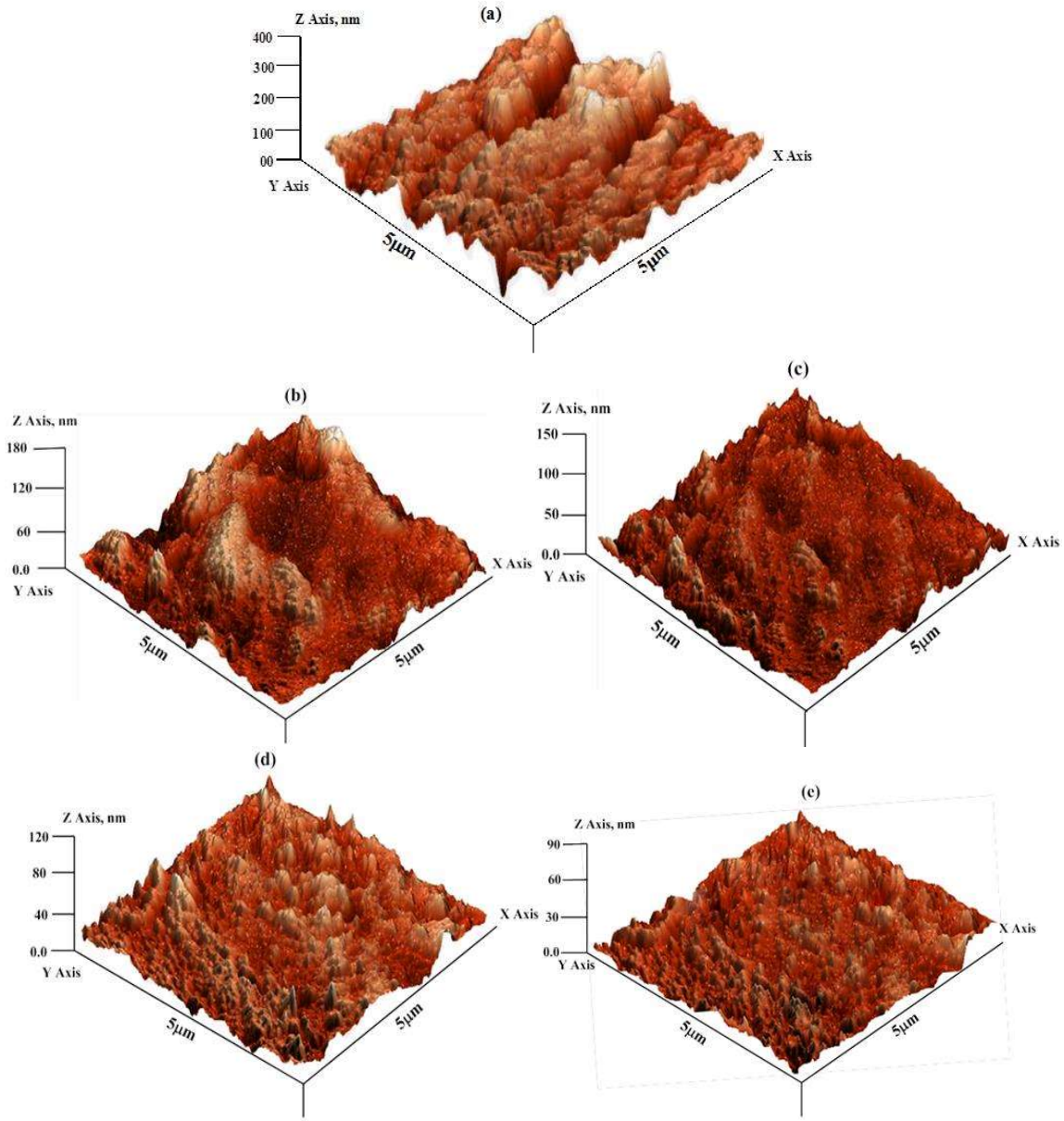


**Figure 3.1.6:** AFM images of mild steel: (a) in absence of APQDs and in the presence of 20 $mgL^{-1}$ of (b) APQD-1, (c) APQD-2, and (d) APQD-3 (e) APQD-4.

In the absence of inhibitors, average surface roughness was 392 nm while in presence of optimum concentration of inhibitors; average surface roughnesses were 162, 146, 118, and 96 nm for APQD-1, APQD-2, APQD-3 and APQD-4, respectively. These

observations further suggest the formation of protective film by inhibitor, which isolates the metal from aggressive acid attack.

### 3.1.8: Quantum chemical calculations

The optimized molecular structures of 5-arylpyrimido-[4, 5-b] quinoline-diones and their respective HOMO and LUMO electron density surfaces of the studied compounds are shown in Figures 3.1.7 and 3.1.8. The optimized structures show that for all the four compounds, the phenyl groups are non-coplanar with respect to the pyrimido-quinoline-dione ring.

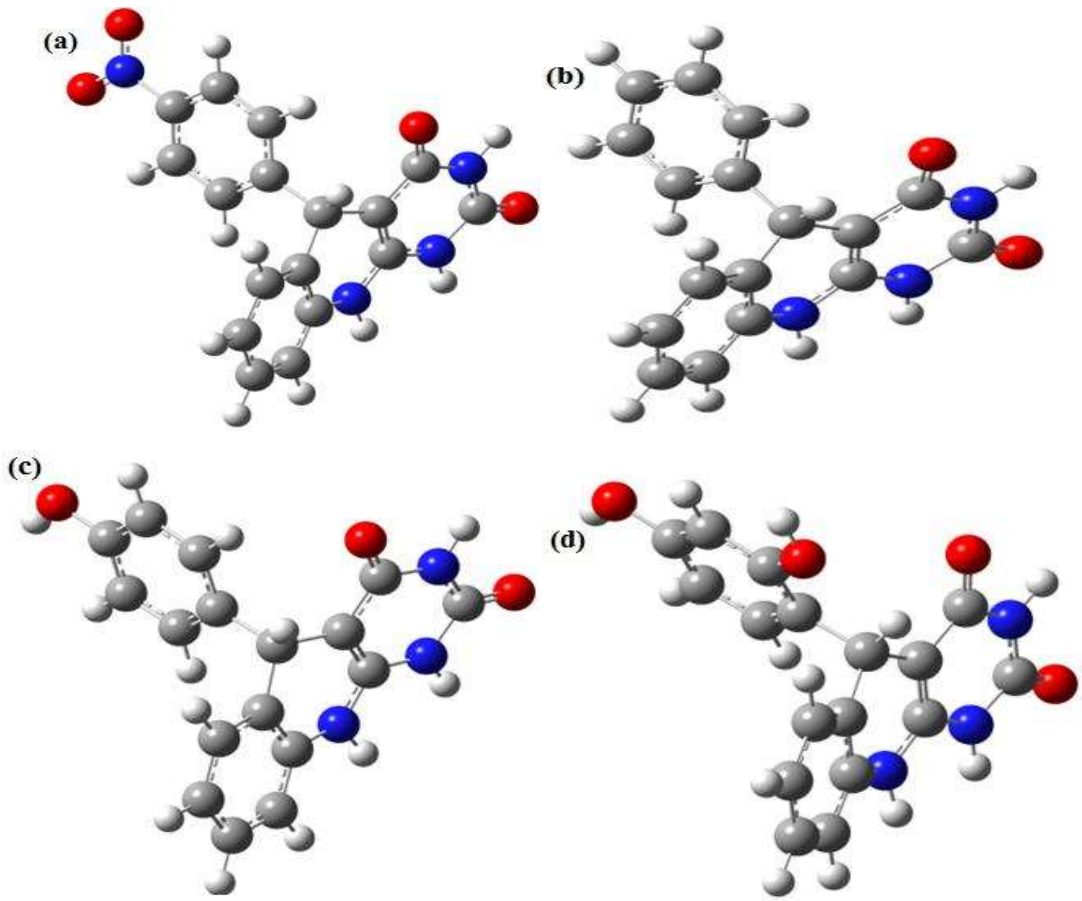


**Figure 3.1.7:** Optimized molecular structures of (a) APQD-1, (b) APQD-2, (c) APQD-3 and (d) APQD-4

The HOMO electron density distribution provides information about the sites or fragments of the molecule that are most likely to donate electrons to the appropriate orbital of an acceptor species, while the LUMO electron density distribution is a pointer

to the sites of the molecule that possess higher chances of accepting electrons from a donor species [Chiter *et al.* (2015), Gece (2008)]. As shown in Figure 3.1.8, the electron density of the HOMO is delocalized over the entire molecular atoms/rings for APQD-3 and APQD-4, while the 4-nitrophenyl group and the phenyl group at position 5 of the pyrimido-quinoline-dione ring in APQD-1 and APQD-2 respectively are not completely involved in the HOMO distributions. The involvement of the hydroxyl-substituted phenyl groups in APQD-3 and APQD-4 in the HOMO distribution is due to the electron donating effect of the hydroxyl group(s) adjacent to the phenyl ring. Similarly, the low participation of the 4-nitrophenyl group in APQD-1 in the HOMO electron density distribution is due to the electron withdrawing effect of the nitro group, which decreases the electron density on the adjacent phenyl ring [Verma *et al.* (2015b); Gece (2008)]. This observation was also supported by the LUMO electron density distributions, which is concentrated on the 4-nitrophenyl group in APQD-1, indicating the high tendency of electron acceptance by the group. The LUMO is also completely delocalized over the entire pyrimido-quinoline-dione rings in APQD-2, APQD-3 and APQD-4 with somewhat reduced electron density on the atoms of the phenyl group. The –OH groups in APQD-3 and APQD-4 make very little contributions to the LUMO, which indicate that the molecules are not likely to accept electrons through these sites. The values of some quantum chemical parameters for the studied compounds are listed in Table 3.1.7. The $E_{HOMO}$ is a measure of the tendency of a molecule to donate its HOMO electrons to the appropriate vacant orbital of the receiving species, such that the higher the $E_{HOMO}$ the better the chance of electron donation by the molecule [Chiter *et al.* (2014); Lebrini *et al.* (2005)]. The values of the $E_{HOMO}$ for the studied inhibitors are in the order: APQD-4 > APQD-3 > APQD-2 > APQD-1, which agrees with the order of the experimental inhibition efficiencies (Table 3.1.7). The $E_{LUMO}$ on the other hand is a measure of the

affinity of a molecule to accept electrons to its LUMO, such that the lower the $E_{LUMO}$ the higher the propensity of the inhibitor molecule to accept electrons from the appropriate occupied orbitals of iron.

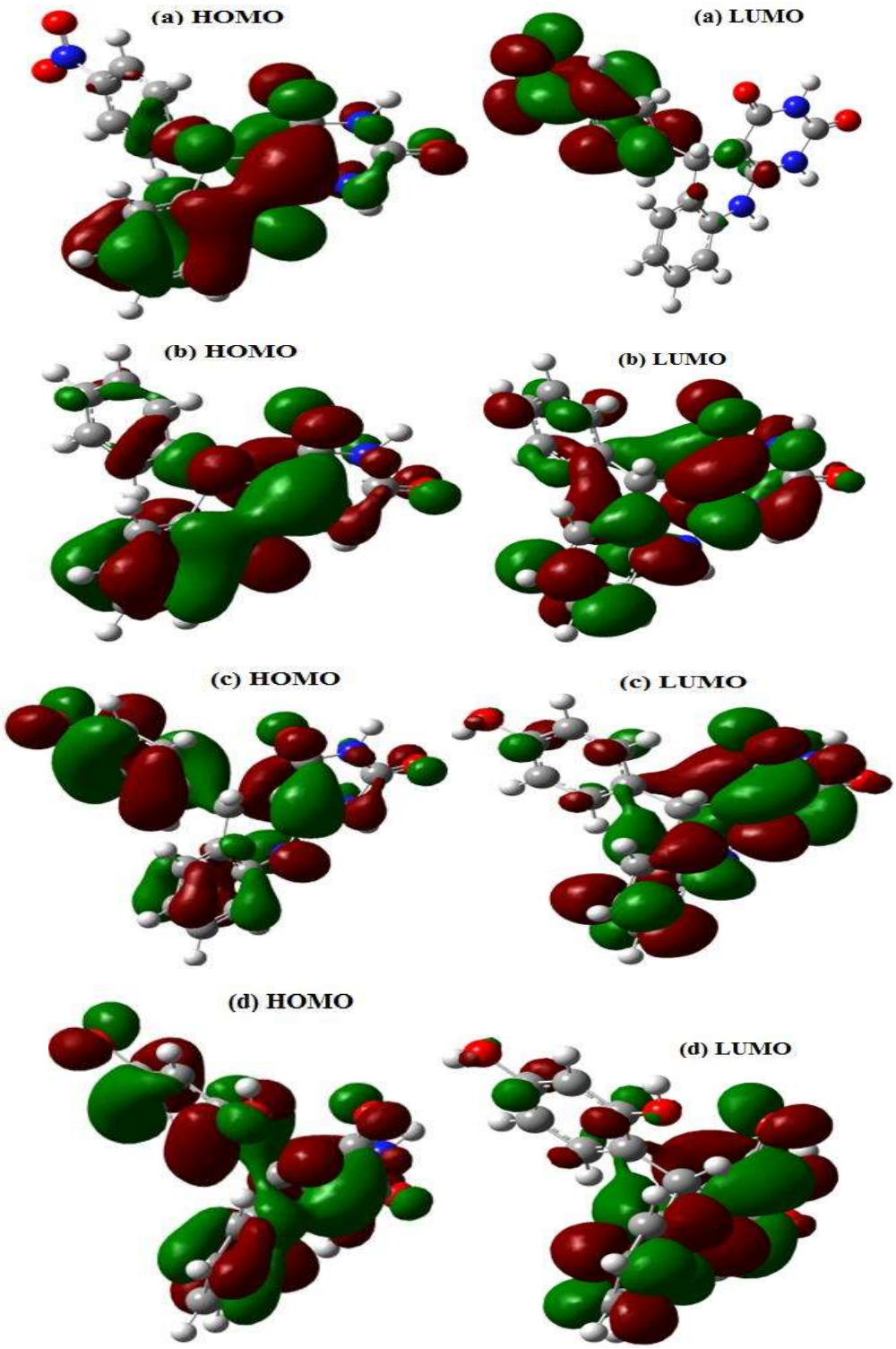


**Figure 3.1.8:** The frontier molecular orbital (left-hand side: HOMO; and right-hand side: LUMO) of the studied APQDs (a) APQD-1 (b) APQD-2, (c) APQD-3, and (d) APQD-4

The results of the $E_{LUMO}$ in Table 3.1.7 do not agree with the trend of the observed inhibition efficiencies. This suggests that the $E_{LUMO}$ may not be a good descriptor for the relative inhibition efficiency of the studied molecules. The energy gap, $\Delta E$ is another index of reactivity of molecules for which a molecule with lower $\Delta E$ is usually more reactive and possesses higher inhibition efficiency [Saha *et al.* (2015)]. The trend of the $\Delta E$ values obtained for the studied compounds is also not in agreement with the experimental inhibition efficiencies. The global electronegativity, $\chi$ is another reactivity index that predicts the extent to which a molecule holds on to its electrons. The higher the $\chi$ value the lower the chance of electron donation by the molecule and vice versa. The trend of the values of $\chi$ in Table 3.1.7 is APQD-4< APQD-3< APQD-2< APQD-1, which suggests that APQD-4 has the highest possibility of donating electrons to an electrophilic center such as the iron surface that is populated by positive charges. The trend of $\chi$ is in agreement with the experimental inhibition efficiencies. The values of $\Delta N$, the fraction of electrons transferred from the inhibitor molecule to the metal as reported in Table 3.1.7 also corroborate the trend of the experimental inhibition efficiencies.

**Table 3.1.7:** Quantum chemical parameters derived from the B3LYP/6-31+G(d,p) method

| **Parameters→ Compounds↓** | $E_{HOMO}$ **(eV)** | $E_{LUMO}$ **(eV)** | $\Delta E$ **(eV)** | $\chi$ **(eV)** | $\Delta N$ |
|---|---|---|---|---|---|
| **APQD-1** | -6.518 | -2.763 | 3.755 | 4.640 | 0.629 |
| **APQD-2** | -6.155 | -1.316 | 4.838 | 3.735 | 0.675 |
| **APQD-3** | -6.058 | -1.282 | 4.776 | 3.670 | 0.697 |
| **APQD-4** | -6.022 | -1.173 | 4.848 | 3.598 | 0.702 |

The $\Delta N$ values suggest that the fraction of electrons transferred from the inhibitor molecule to iron is in the order: APQD-4 > APQD-3 > APQD-2 > APQD-1. All the

quantum chemical parameters reported in Table 3.1.7 are in support of the assumption that the mode of adsorption of the studied molecules on the steel surface is predominantly via electron donation from the high electron density sites of the molecules to the iron. This assumption is also related to the fact that the surface of mild steel in acidic medium is reportedly populated by positive charges [Saha *et al* (2015); Verma *et al.* (2015d)], and interaction of inhibitor molecules with the positively charged steel surface is a favorable process.

The Fukui indices, $f_k^+$ and $f_k^-$ were calculated to predict the most probable atomic sites for nucleophilic and electrophilic attacks respectively. The electron density surfaces of the $f_k^+$ and $f_k^-$ are shown in Figure 3.1.9. The regions of the molecules with higher values of $f_k^+$ are more susceptible to attack by electron rich species, while the sites of the molecules with higher values of $f_k^-$ are more disposed to interactions with electron deficient species. It is apparent from the distributions of the differential change in electron density for the $f_k^+$ shown in Figure 3.1.9 that the site of the nitro group in APQD-1 is mostly likely to interact with negatively charged steel surface if such exists during the adsorption process, while the corresponding most probable sites for possible interactions with negatively charged centers in APQD-2, APQD-3 and APQD-4 involve only some of the atoms in the pyrimido-quinoline-dione rings. The electron density surfaces for the $f_k^-$ of the studied molecules also revealed that all the studied compounds have high tendencies of interacting with a positively charged iron surface via the pi-electron sites shared by the condensed pyrimido and the quinoline rings. The N- and O- atoms in the molecules except the nitro group in APQD-1 also have good chances of nucleophilic interactions.

### 3.1.9: Molecular dynamics (MD) simulations

Recently, the molecular dynamics simulations approach has emerged as a modern tool that aids the study of the interactions between inhibitor molecules and metal surface [Xu *et al*. (20140)].

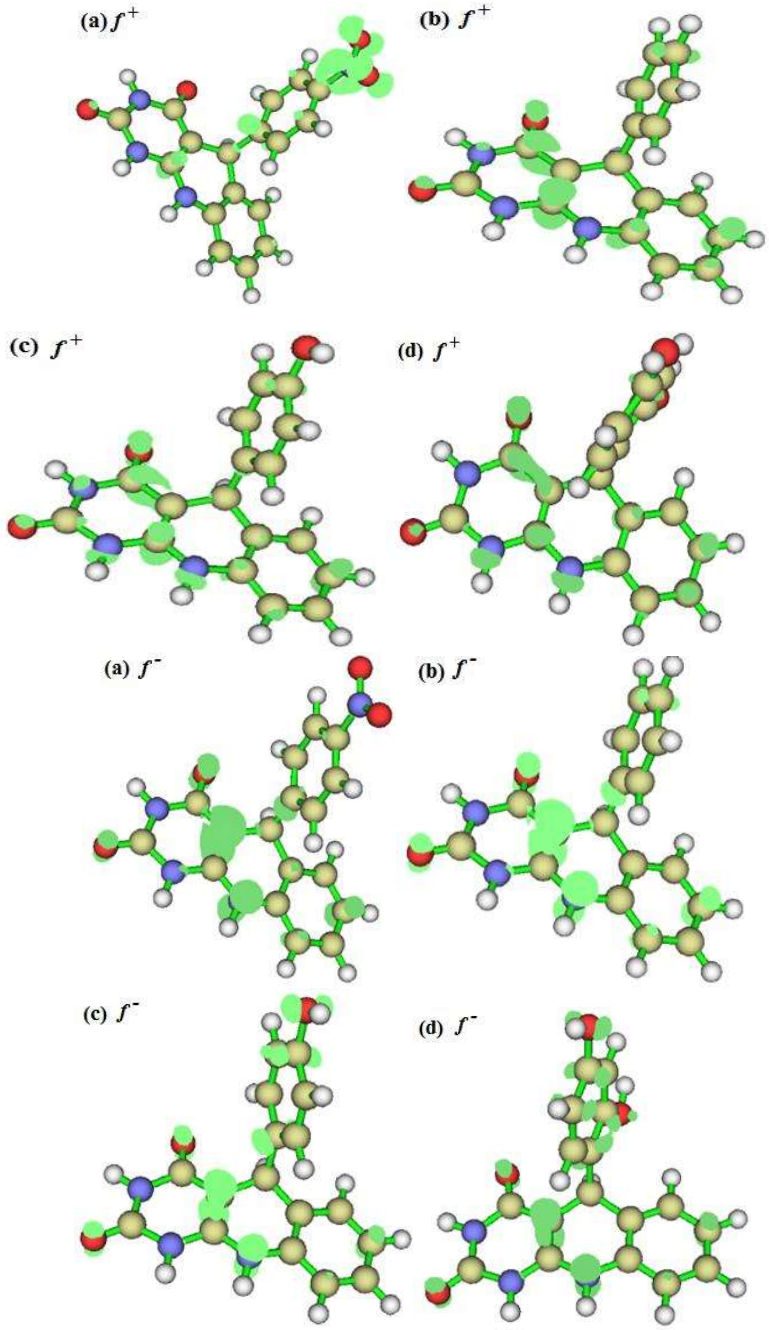


**Figure 3.1.9:** Fukui indices for the electrophilic ( $f_k^+$ ) and nucleophilic ( $f_k^-$ ) sites for (a) APQD-1, (b) APQD-2, (c) APQD-3, and (d) APQD-4. (All the surfaces were visualized at isosurface value of 0.004, except for the $f_k^+$ of (c) APQD-3, and (d) APQD-4 for which isosurface value of 0.0028 and 0.0025 respectively, were used for better visualization).

In the present study, the MD simulations studies were undertaken to predict the binding strength of the APQDs with mild steel surface.

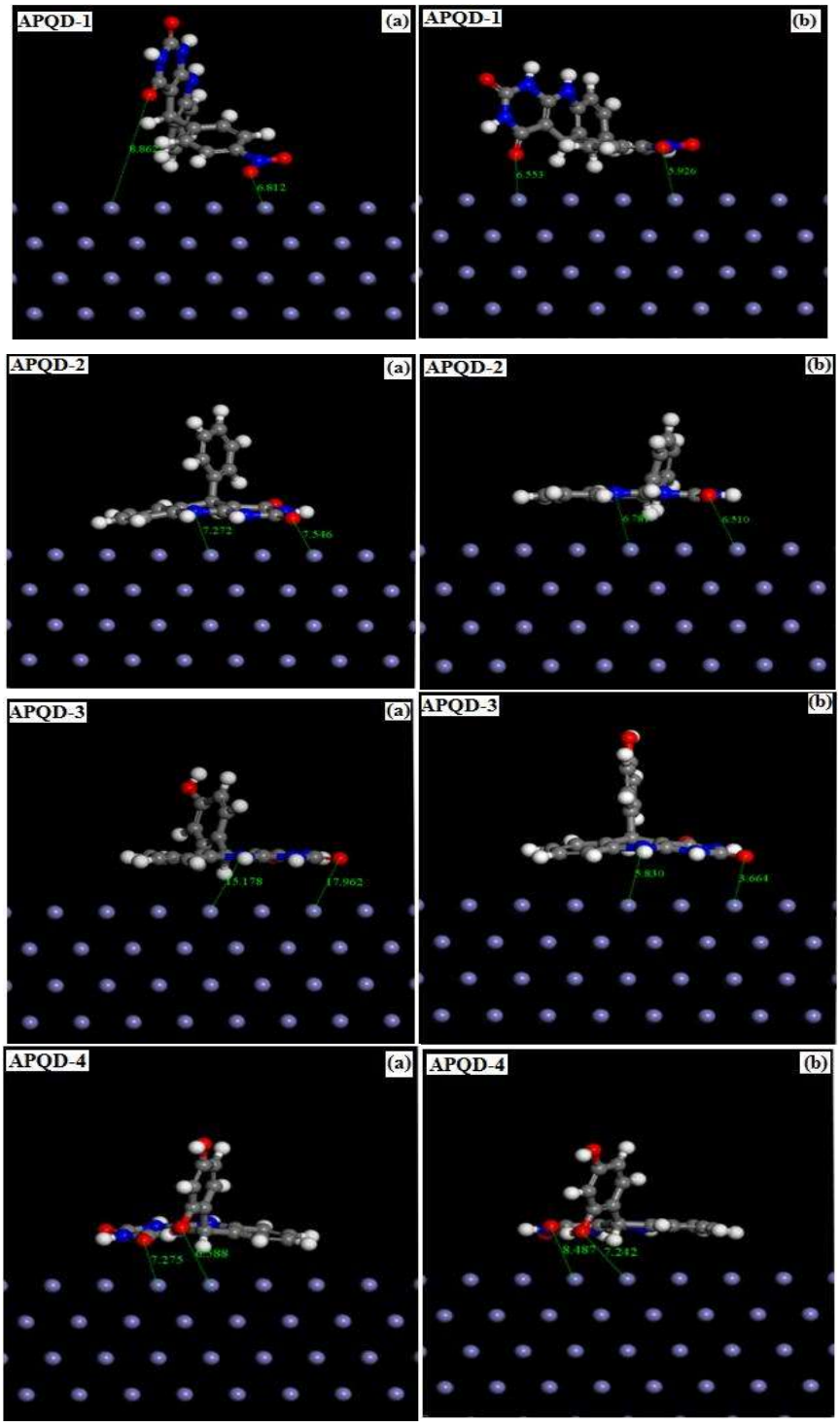


**Figure 3.1.10:** Side view equilibrium adsorption of APQD-1, APQD-2, APQD-3and APQD-4on Fe (110) surface (a) before and (b) after molecular dynamics simulations.

Figure 3.1.10 represents the side view equilibrium adsorption of all the studied inhibitors before and after molecular dynamics simulations. It can be seen from the Figure 3.1.10 that all the studied compounds are adsorbed on mild steel surface with a flat or parallel orientation through several potential binding sites as previously pointed out in the quantum chemical study (*vide supra*). By considering that the Fe (110) surface as clean and ions free, the values of the interaction energy ($E_{interaction}$) and binding energy ($E_{binding}$) were calculated for all the studied inhibitors and the results are presented in Table 3.1.8. The results in Table 3.1.8 showed that the $E_{interaction}$ between the studied APQDs and Fe (110) surface are negative indicating spontaneous adsorption of the APQDs molecules on the Fe surface. A more negative value of $E_{interaction}$ between an organic molecule and a metal surface is a reflection of high $E_{binding}$ [Verma *et al.* (2016a)]. Apparently, the high positive values of $E_{binding}$ for the investigated inhibitors indicate that the compounds adsorbed strongly on the Fe surface, which matches with the experimentally observed high inhibition efficiency. The $E_{binding}$ values (in kJ/mol) of the studied inhibitors follow the order: APQD-4 (484.42) > APQD-3 (448.94) > APQD-2 (391.71) > APQD-1 (349.11) which is in accordance with the order of the observed inhibition efficiency. The APQD-4 gives the maximum value of $E_{binding}$ among all the four APQDs studied during the simulation process suggesting the highest inhibition efficiency of APQD-4 among the studied inhibitors [Olasunkanmi *et al.* (2015)].

**Table 3.1.8:** Interaction energies between the inhibitors and Fe (110) surface (in $kJmol^{-1}$)

| Systems | $E_{interaction}$ | $E_{binding}$ |
|---|---|---|
| **Fe (110) + APQD-1** | -83.44 | 83.44 |
| **Fe(110) + APQD-2** | -93.62 | 93.62 |
| **Fe(110) + APQD-3** | -107.30 | 107.30 |
| **Fe(110) + APQD-4** | -115.78 | 115.78 |

## 3.2. 2-amino-4-arylquinoline-3-carbonitriles as corrosion inhibitors

Quinoline and its derivatives possess potential applications for synthesis of biologically important compounds such as DNA binding capabilities, antitumor and DNA-intercalating carrier [Ebenso *et al.* (2010b)]. Previously, a few reports have been published on quinoline and its derivatives as useful metallic corrosion inhibitors [Ebenso *et al.* (2010c)]; Li *et al.* (2007); Lamaka *et al.* (2007); Achary *et al.* (2008); Popova *et al.* (2011); Pavithra *et al.* (2010); Wang *et al.* (2012); Ebenso *et al.* (2012a)]. The main objective of present work was to compare the corrosion inhibition efficiency of three synthesized 2-amino-4-arylquinoline-3-carbonitriles (AACs) namely, 2-amino-4-(4-nitrophenyl) quinoline-3-carbonitrile (AAC-1), 2-amino-4-phenylquinoline-3-carbonitrile (AAC-2) and 2-amino-4-(4-hydroxyphenyl) quinoline-3-carbonitrile (AAC-3) on mild steel corrosion in 1M HCl. Several methods such as weight loss, electrochemical impedance spectroscopy (EIS), scanning electron microscopy (SEM), atomic force microscopy (AFM), and quantum chemical techniques were used for this purpose. The selection criteria of these compounds as corrosion inhibitors is based on the facts that they: (a) can be easily synthesized from commercially available cheap and green starting materials in high yields (b) they are expected to exhibit good inhibition efficiency due to presence of aromatic rings and several heteroatoms in form of polar functional groups (-OH $-NO_2$, -CN, $-NH_2$) through which they can adsorb on the metal surface (c) they are soluble solubility in testing medium. Perusal of literature reveals that no work has been reported earlier on 2-amino-4-arylquinoline-3-carbonitriles (AACs) as corrosion inhibitors. The molecular structure and IUPAC name of the inhibitors used are given in Table 3.2.1.

### 3.2.1. Gravimetric measurements

The Effect of AACs concentrations on mild steel corrosion at 308 K after 3 immersion time were investigated by weight loss method.

**Table 3.2.1:** IUPAC name, molecular structure, and abbreviation of the studies inhibitors

| S.No. | IUPAC name | chemical Structure | Abbreviation |
|---|---|---|---|
| 1 | 2-amino-4-(4-nitrophenyl) quinoline-3-carbonitrile | 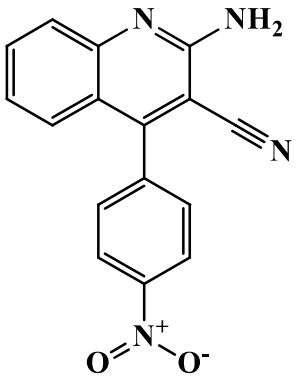 | AAC-1 |
| 2 | 2-amino-4-phenylquinoline-3-carbonitrile | 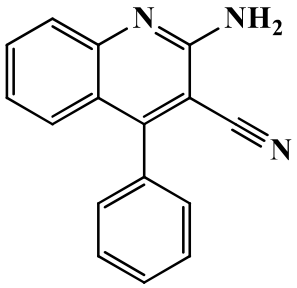 | AAC-2 |
| 3 | 2-amino-4-(4-hydroxyphenyl ) quinoline-3-carbonitrile | 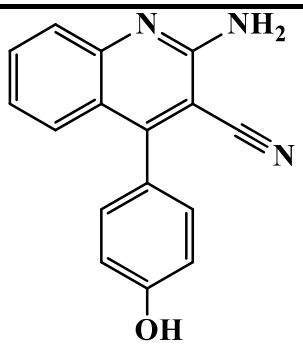 | AAC-3 |

Variation of the inhibition efficiency with AACs concentration is shown in Figure 3.2.1(a) and corrosion parameters such as corrosion rate ($C_R$), inhibition efficiency ($\eta$%), and surface coverage ($\theta$) are given in Table 3.2.2. From the results it is seen that the values of weight loss (mg) and corrosion rate ($C_R$) were decreased with an increased in AACs

concentration and maximum efficiency was observed at 40 $mgL^{-1}$ concentration. The AAC-1, AAC-2 and AAC-3 showed maximum efficiency of 94.78%, 95.65% and 96.52%, respectively at 40 $mgL^{-1}$ concentration and 308 K temperature. The increased AACs concentration causes increased adsorption and surface coverage due to availability of large number of inhibitor molecules therefore increases inhibition efficiency [Yadav *et al.* (2013); Aouniti *et al.* (2013)]. The AAC-3 attained the highest inhibition efficiency among the studied compounds due to presence of additional electron releasing hydroxyl (-OH) group AAC-3. Whereas, AAC-1 exhibited the lowest inhibition efficiency which is attributed due to presence of electron withdrawing nitro ($-NO_2$).

**Table 3.2.2:** The weight loss parameters obtained for mild steel in 1 M HCl containing different concentrations of AACs.

| inhibitor | Conc ($mgL^{-1}$) | Weight loss (mg) | $C_R$ ($mg\ cm^{-2}\ h^{-1}$) | $\theta$ | $\eta$% |
|---|---|---|---|---|---|
| **Blank** | 0.0 | 230 | 7.66 | --- | --- |
| **AAC-1** | 10 | 86 | 2.86 | 0.626 | 62.6 |
| | 20 | 39 | 1.30 | 0.8304 | 83.04 |
| | 30 | 21 | 0.70 | 0.9086 | 90.86 |
| | 40 | 12 | 0.40 | 0.9478 | 94.78 |
| | 50 | 11 | 0.36 | 0.9521 | 95.21 |
| **AAC-2** | 10 | 64 | 2.13 | 0.7217 | 72.17 |
| | 20 | 28 | 0.93 | 0.8782 | 87.82 |
| | 30 | 17 | 0.56 | 0.9260 | 92.60 |
| | 40 | 10 | 0.33 | 0.9565 | 95.65 |
| | 50 | 9 | 0.30 | 0.9608 | 96.08 |
| **AAC-3** | 10 | 47 | 1.56 | 0.7956 | 79.56 |
| | 20 | 19 | 0.63 | 0.9173 | 91.73 |
| | 30 | 14 | 0.46 | 0.9391 | 93.91 |
| | 40 | 8 | 0.26 | 0.9652 | 96.52 |
| | 50 | 7 | 0.23 | 0.9695 | 96.95 |

**Table 3.2.3:** Variation of $C_R$ and $\eta$ % with temperature in absence and presence of optimum concentration of AACs in 1M HCl

| Temperature (K) | Corrosion rate ($C_R$) (mg cm$^{-2}$ h$^{-1}$) and Inhibition efficiency ($\eta\%$) | | | | | | | |
|---|---|---|---|---|---|---|---|---|
| | Blank | | AAC-1 | | AAC-2 | | AAC-3 | |
| | $C_R$ | $\eta\%$ | $C_R$ | $\eta\%$ | $C_R$ | $\eta\%$ | $C_R$ | $\eta\%$ |
| **308** | 7.66 | --- | 0.46 | 93.99 | 0.33 | 95.69 | 0.26 | 96.60 |
| **318** | 11.0 | --- | 1.30 | 88.81 | 1.00 | 90.90 | 0.80 | 92.72 |
| **328** | 14.3 | --- | 3.10 | 78.32 | 2.46 | 82.79 | 1.93 | 86.50 |
| **338** | 18.6 | --- | 6.50 | 65.05 | 5.43 | 70.80 | 4.86 | 73.87 |

### 3.2.2. Kinetic parameters: effect of temperature

Variation of inhibition efficiency ($\eta\%$) and corrosion rate ($C_R$) with electrolyte solution is given in Table 3.2.3 From the result depicted in Table 3.2.3 it seen that an increase in electrolyte temperature leads to an increase in the rate of mild steel dissolution and corrosion for inhibited and uninhibited acid solutions. The effect of temperature on metallic dissolution in inhibited solution is highly complex, because at elevated temperature several changes such as rapid etching, desorption of inhibitor and decomposition and/or rearrangement of inhibitor takes place [Bai *et al.* (2015)]. The Arrhenius equation is successfully used to establish the relationship between corrosion rate ($C_R$) and temperature where the natural logarithm of the corrosion rate ($C_R$) is a linear function with 1/ T. The Arrhenius plots [Figure 3.2.1(b)] give a straight line between log $C_R$ versus $1/T$. The values of activation energy ($E_a$) for mild steel dissolution were calculated from the slopes ($-\Delta E_a/2.303R$) of the Arrhenius plots. The values of apparent activation energies are higher in presence of AACs than in their absence (28.48 kJmol$^{-1}$). The higher values of apparent activation energy for AAC-1 (71.40 kJ mol$^{-1}$), AAC-2 (73.73 kJ mol$^{-1}$) and AAC-3 (75.65 kJ mol$^{-1}$) indicated the creation of energy barrier for mild steel dissolution in presence of AACs [Yadav and Quraishi (2012)]. Further, it is assumed that electrostatic interaction (physical adsorption) between charged inhibitors and

metal surface might cause increase in the values of apparent activation energy in presence of AACs [Ashassi-Sorkhabi *et al.* (2005)].

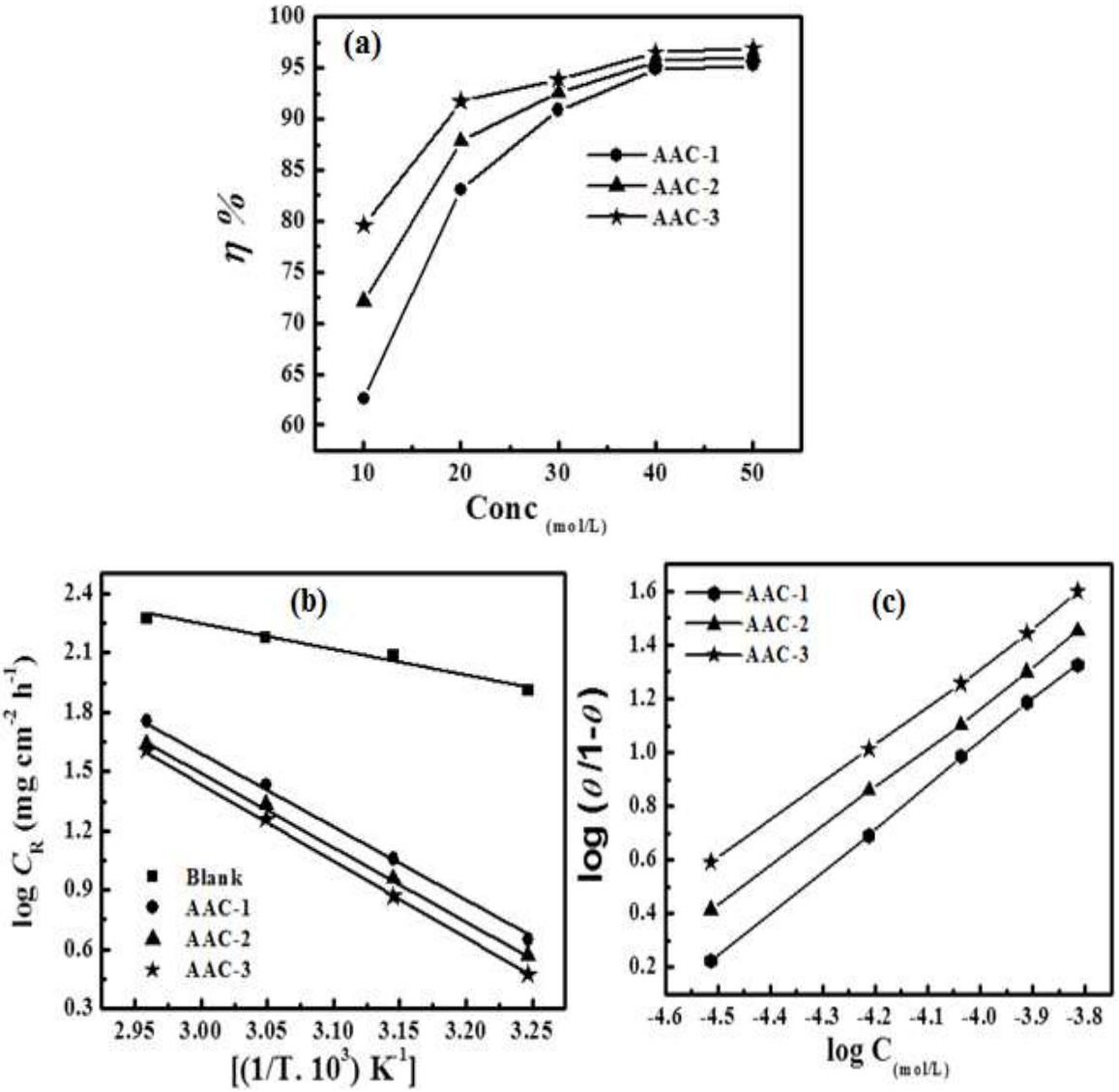


**Figure 3.2.1:** (a) Variation of inhibition efficiency with AACs concentration (b) Arrhenius plots of log $C_R$ vs. 1000/$T$ (c) Langmuir isotherm plot for the adsorption of the AACs on mild steel surface in 1M HCl.

### 3.2.3: Thermodynamic parameters: Adsorption isotherm

Several adsorption isotherms were tested but gave the best fit. The Langmuir isotherm [Figure 3.2.1(c)] gives a straight line between log $\theta$/1-$\theta$ versus log $C$ (molL$^{-1}$). The calculated values of $K_{ads}$ and $\Delta G^0_{ads}$ at each studied temperature in presence of optimum concentration of AACs are given in Table 3.2.4. The higher values of $K_{ads}$ in presence of AACs suggest that the AACs adsorbed easily and strongly on the mild steel surface [Ait Albrimi *et at.* (2015); Ghareba and Omanovic (2010); Negm *et al.* (2011)]. Inspection of the Table 3.2.4 reveals that the values of $\Delta G^0_{ads}$ varied from -34.62 kJ mol$^{-1}$ to -36.96 kJ mol$^{-1}$, which strongly suggest the physiochemical mode of adsorption by AACs on mild steel surface. Further, the negative sign of $\Delta G^0_{ads}$ validated the spontaneous nature of adsorption by the AACs on mild steel surface [Yıldız *et al.* (2014a); Yıldız *et al.* (2014b); Li *et al.* (2011)].

**Table 3.2.4:** The values of $K_{ads}$ and $\Delta G^\circ_{ads}$ for mild steel in absence and presence of optimum concentration of AACs in 1M HCl at different studied temperature

| **Inhibitor** | **$K_{ads}$ ($10^4$ M$^{-1}$)** | | | | **$-\Delta G^\circ_{ads}$ (k J mol$^{-1}$)** | | | |
|---|---|---|---|---|---|---|---|---|
| | 308 | 318 | 328 | 338 | 308 | 318 | 328 | 338 |
| **AAC-1** | 2.17 | 0.92 | 0.58 | 0.42 | 35.87 | 34.78 | 34.76 | 34.62 |
| **AAC-2** | 2.63 | 1.11 | 0.77 | 0.45 | 36.36 | 35.36 | 35.27 | 34.96 |
| **AAC-3** | 3.32 | 1.24 | 0.93 | 0.49 | 36.96 | 35.89 | 35.56 | 35.21 |

### 3.2.4: Potentiodynamic polarization studies

The polarization behavior of mild steel in the absence and presence of inhibitors is shown in Figure 3.2.2. Several electrochemical parameters such as corrosion potential ($E_{corr}$), corrosion current density ($i_{corr}$), anodic and cathodic Tafel slopes ($\beta_a$ and $\beta_c$), as well as corrosion inhibition efficiency ($\eta$%) are listed in Table 3.2.5. The results given in the

Table shows that all the studied compounds bring down the $i_{corr}$ values at all concentrations and maximum decreases in $i_{corr}$ value is obtained 50 $mgL^{-1}$ concentration. It is also found that the adsorption of these compounds do not show significant potential shift (< ± 85 mV) thereby behave as mixed type. It is also observed that cathodic reaction is more decreased than anodic reactions which demonstrate the cathodic predominance of the inhibitors [Saha *et al.* (2015)].

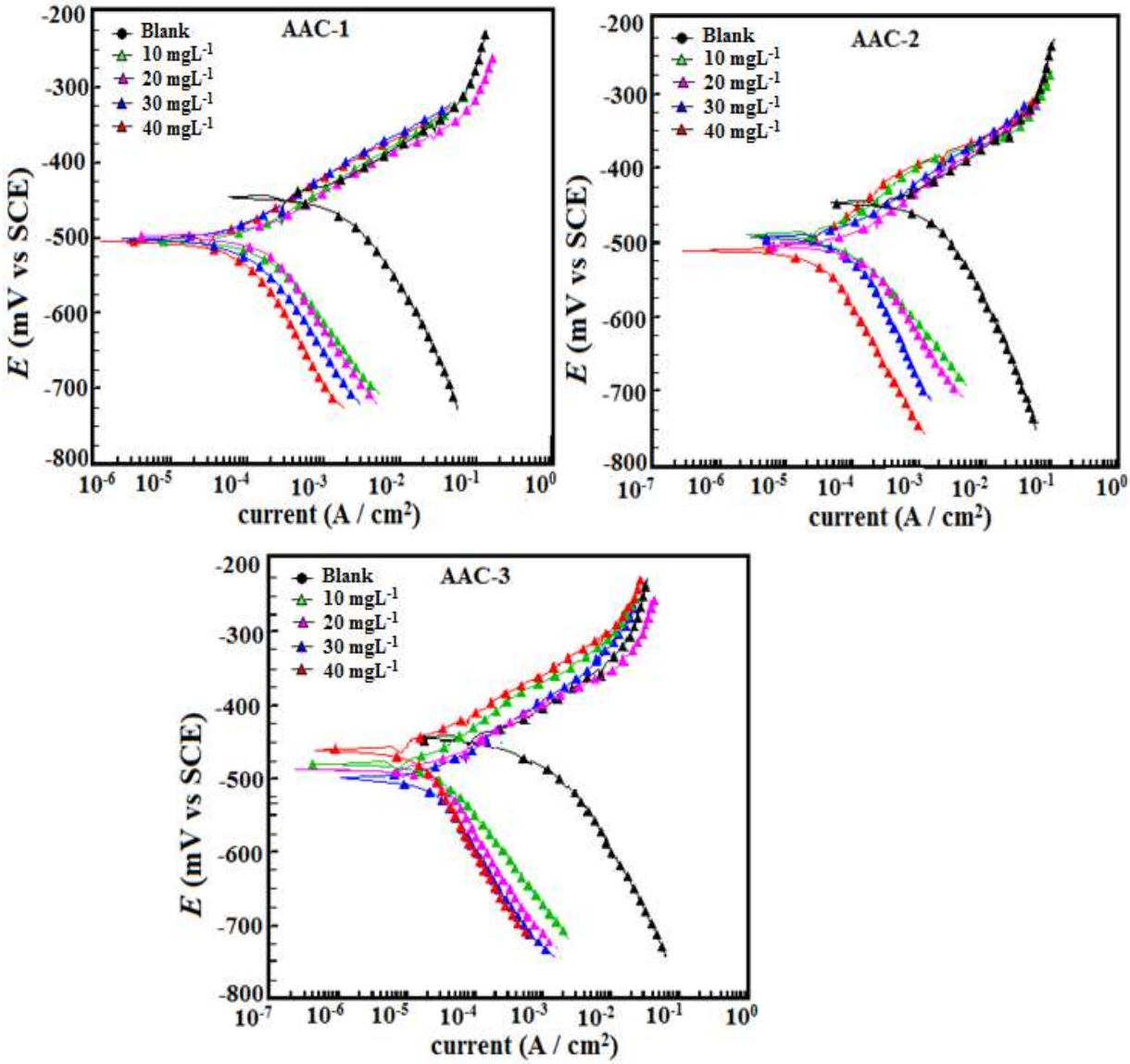


**Figure 3.2.2:** Polarization curves for mild in absence and presence of different concentration of AACs

From the polarization results depicted in Figure 3.2.2 and Table 3.2.5, it is observed that the presence of three inhibitors significantly reduced the values of corrosion

current densities without causing any substantial change in the values of $E_{corr}$. This finding suggests that investigated AACs inhibit mild steel corrosion in acid solution by forming a surface film without changing the mechanism of mild steel corrosion [Murulana *et al.* (2015)]. Further, the shift in $E_{corr}$ values is not very prominent, the maximum shift in $E_{corr}$ values were 59, 65 and 66 mV for AAC-1, AAC-2 and AAC-3, respectively, toward cathodic polarization suggesting that investigated inhibitors acted as mixed type inhibitors mainly cathodic inhibitors [Alkhathlan *et al.* (2015)].

**Table 3.2.5:** Tafel polarization parameters for mild steel in 1 M HCl solution in absence and at different concentrations of AACs.

| Inhibitor | Conc Mg/L | $E_{corr}$ (mV/SCE) | $\beta_a$ ($\mu A/cm^2$) | $\beta_c$ (mV/dec) | $i_{corr}$ (mV/dec) | $\eta$% |
|---|---|---|---|---|---|---|
| **Blank** | --- | -445 | 70.5 | 114.6 | 1150 | ---- |
| **AAC-1** | 10 | -489 | 79.2 | 146.4 | 436.6 | 62.03 |
| | 20 | -499 | 77.3 | 187.5 | 173.2 | 84.93 |
| | 30 | -504 | 77.3 | 127.8 | 93.7 | 91.85 |
| | 40 | -494 | 85.1 | 90.8 | 76.8 | 93.32 |
| **AAC-2** | 10 | -499 | 80.2 | 103.5 | 263.9 | 77.05 |
| | 20 | -458 | 39.6 | 52.0 | 128.3 | 88.84 |
| | 30 | -491 | 75.6 | 82.6 | 68.5 | 94.04 |
| | 40 | -510 | 80.7 | 116.7 | 47.1 | 95.90 |
| **AAC-3** | 10 | -504 | 72.2 | 119.8 | 213.5 | 81.43 |
| | 20 | -500 | 73.1 | 187.0 | 86.8 | 92.45 |
| | 30 | -479 | 72.1 | 103.3 | 53.9 | 95.31 |
| | 40 | -511 | 43.4 | 39.3 | 17.86 | 98.44 |

### 3.2.5: Electrochemical impedance spectroscopy (EIS) study

Nyquist plots for mild steel in the absence and presence of different concentration of the inhibitors are given in Figure 3.2.3. The impedance spectrum at each condition gives depressed capacitive imperfect semicircles in high frequency region which is attributed to the charge transfer process and the formation of a protective film by inhibitors on the metal surface [Xu *et al.* (2014)]. The imperfect semicircle of the impedance spectrum is attributed to the mass transfer processes, frequency dispersion as well as inhomogeneities and roughness of metal surface [Mert *et al.* (2014)]. Meanwhile, the diameter of the imperfect semicircles increases on increasing AACs concentrations. This finding suggests that the studied inhibitors strongly aggregate on the mild steel surface and block the active sites and therefore increases the charge transfer resistance as well as inhibition efficiency [Roy *et al.* (2014); Mourya *et al.* (2014)]. In the present case, the impedance nature of mild steel corrosion was studied using previously described simple electrical equivalent circuit consisting of a resistor of solution resistance ($R_s$), a resistor of charge transfer ($R_{ct}$), and a double layer capacitance [Verma *et al.* (2015c)]. The double layer capacitance was replaced by constant phase element (CPE) to find more precise and accurate fit of impedance data. Generally, the value of n related to the surface inhomogeneity. The electrochemical behavior of the CPE is related to the value of n. In general, the value of *n* equal to 0, 1, -1 and 0.5 associated with the resistance, capacitance, inductance and Warburg impedance nature of the metal / electrolyte interface, respectively. In our present work, the value of n varies from 0.777 to 0.998. Upon inspection of the data in Table 3.2.6 it can be seen that $R_{ct}$ increased with increase in the AACs concentration while values of $C_{dl}$ decreased with concentration signifying that the AACs functioned by adsorption at the metal/ electrolyte interfaces [Verma *et al.* (2015a)].

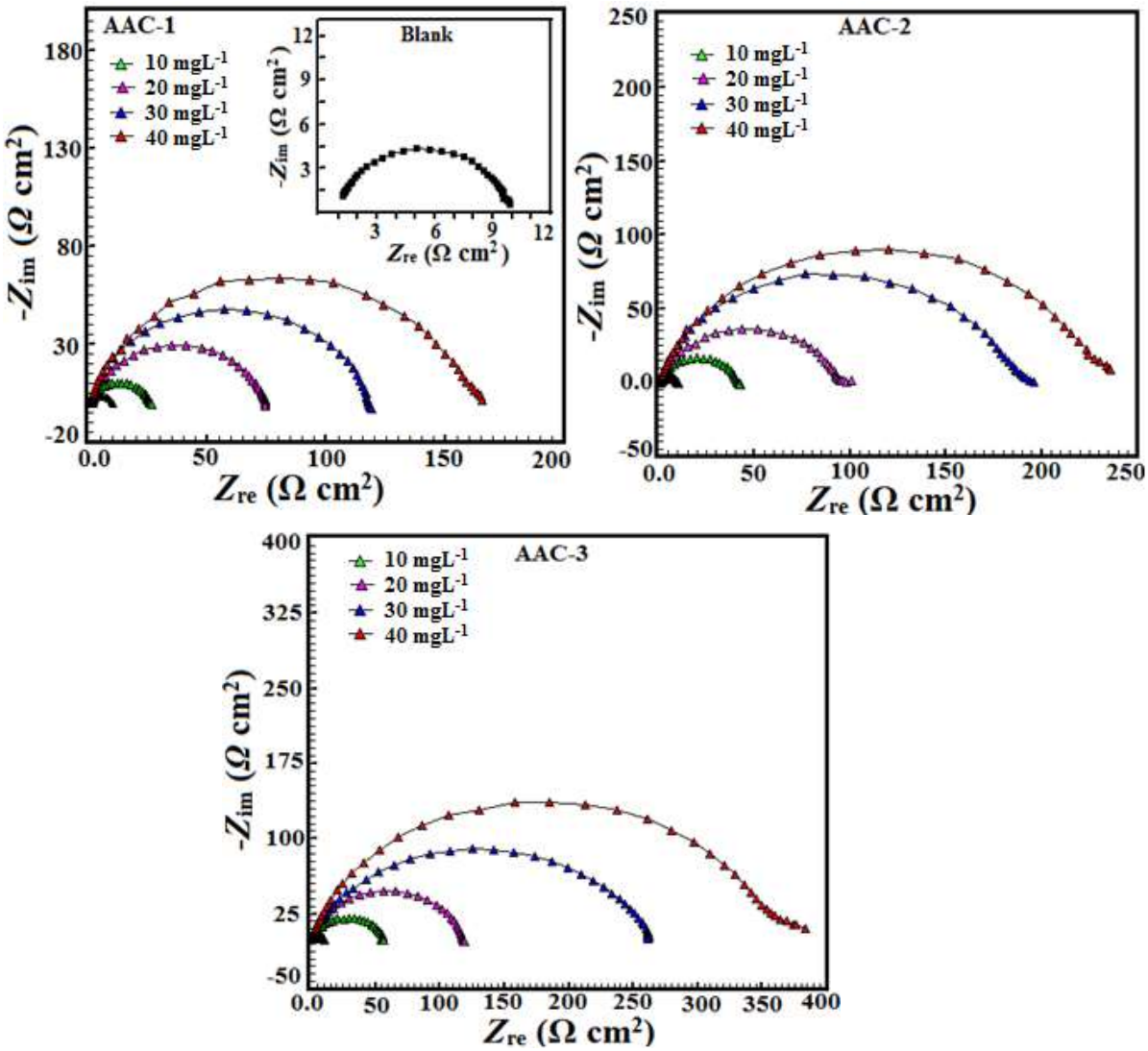


**Figure 3.2.3**: Nyquist plot for mild steel in 1 M HCl without and with different concentrations of AACs

The inhibition efficiency was calculated using equation (6) and maximum observed efficiencies were 94.27%, 96.08%, and 97.42 for AAC-1, AAC-2and AAC-3, respectively, at 40 $mgL^{-1}$ concentration and 308 K temperature.

The Bode plots, shown in Figure 3.2.4 exhibited three different segments in absence of AACs. In high frequency region the values of log /Z/ and phase angle ($\alpha^0$) tend to become zero which is a characteristics response of resistive behavior and corresponds to solution resistance enclosed between reference electrode (saturated calomel electrode) and working electrode (mild steel) [Kissi *et al*. (2006); Naderi *et al.* (2009)]. However, in

the medium frequency region, a linear relationship between log /Z/ against log *f*, with slop values close to -1 and the phase angle value tends to become $-70^0$, were observed.

**Table 3.2.6:** EIS parameters obtained for mild steel in 1 M HCl in absence and presence of different concentration of AACs

| Inhibitor | Conc mg/L | $R_s$ ($\Omega$ cm$^2$) | $R_{ct}$ ($\Omega$ cm$^2$) | $n$ | $C_{dl}$ ($\mu F$ cm$^{-2}$) | $\eta$% | $\theta$ |
|---|---|---|---|---|---|---|---|
| **Blank** | --- | 1.12 | 9.58 | 0.827 | 106.21 | ---- | ---- |
| **AAC-1** | 10 | 0.820 | 24.9 | 0.857 | 30.83 | 61.52 | 0.6152 |
| | 20 | 0.997 | 72.3 | 0.859 | 76.35 | 86.74 | 0.8674 |
| | 300 | 1.510 | 121.3 | 0.866 | 36.40 | 92.10 | 0.9210 |
| | 40 | 0.892 | 167.4 | 0.873 | 32.80 | 94.27 | 0.9427 |
| **AAC-2** | 10 | 0.719 | 40.1 | 0.859 | 64.56 | 76.10 | 0.7610 |
| | 20 | 1.160 | 94.7 | 0.860 | 34.99 | 89.88 | 0.8988 |
| | 30 | 0.649 | 195.5 | 0.869 | 32.15 | 95.09 | 0.9509 |
| | 40 | 0.810 | 244.4 | 0.885 | 29.52 | 96.08 | 0.9608 |
| **AAC-3** | 10 | 2.34 | 51.3 | 0.863 | 62.77 | 81.32 | 0.8132 |
| | 20 | 0.891 | 120.5 | 0.866 | 34.63 | 92.04 | 0.9204 |
| | 30 | 0.76 | 258.8 | 0.879 | 28.47 | 96.29 | 0.9629 |
| | 40 | 0.88 | 371.6 | 0.886 | 25.76 | 97.42 | 0.9742 |

This is a characteristics response of capacitive behavior. An ideal capacitor is associated with slope value of -1 and phase angle value of $-90^0$ [El-Lateef (2015)]. The deviation from ideal capacitive behavior in the presence study is attributed due to rough working electrode surface resulted due to corrosion.

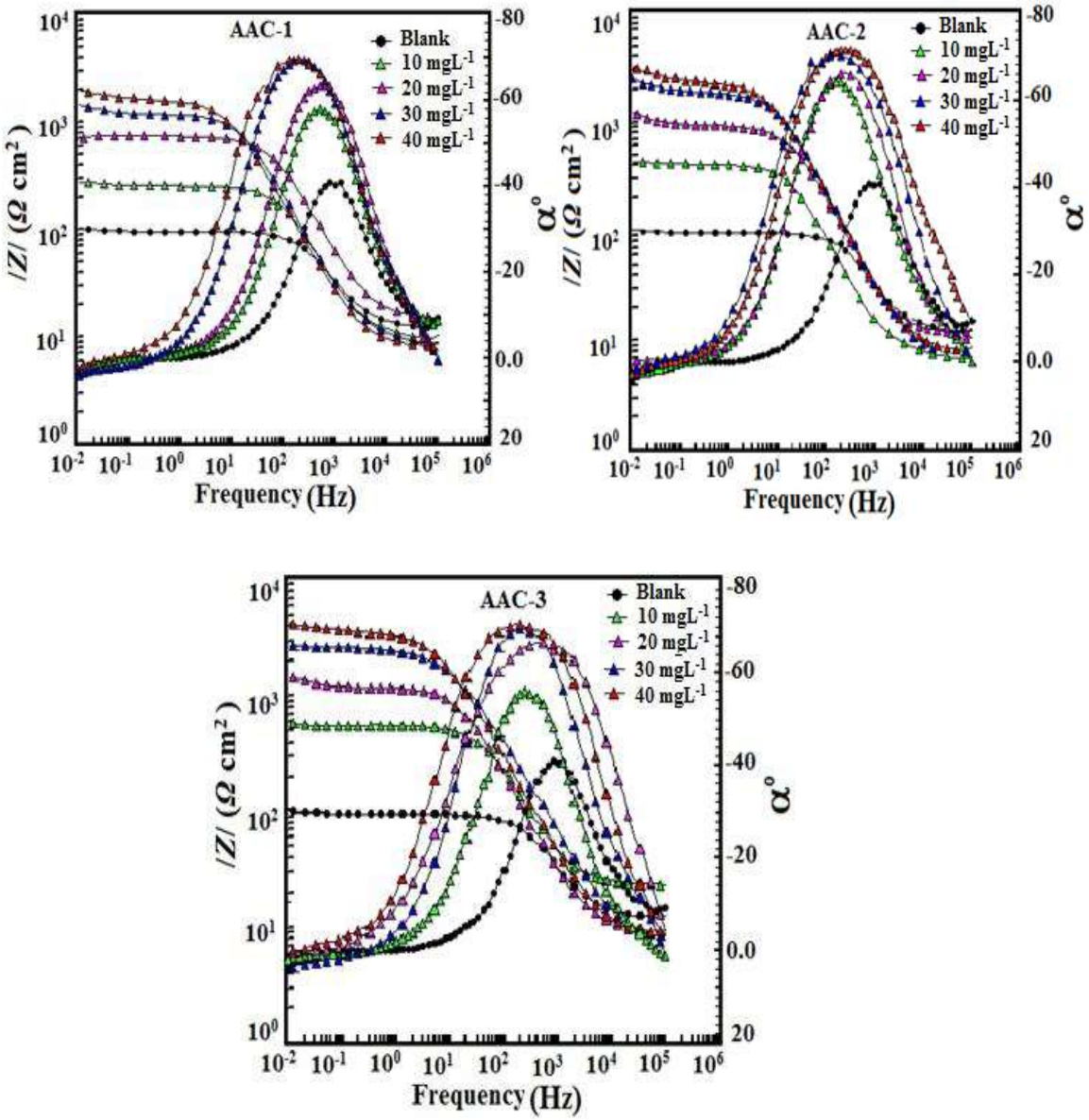


**Figure 3.2.4:** Bode (log *f* vs log |*Z*|) and phase angle (log *f* vs $\alpha^0$) plots for mild steel in 1 M HCl in absence and presence of different concentration of AACs.

The careful examination of the Bode plots reveal that the values of phase angle significantly increased and therefore, surface roughness remarkably decreased in presence of AACs due to formation of protective surface film [Liu *et al.* (2015)]. Further, Bode plots give one time constant, sigma maxima in the intermediate frequency region. The broadening of this maximum in the Bode plots is attributed due to the adsorption and

formation of protective film by inhibitors at the metal/ electrolyte interface [Behpour *et al.* (2009)].

### 3.2.6: Scanning electron microscopy (SEM) study

. Figure 3.2.5(a) reveals a SEM micrograph of mild steel surface before exposing to the test solution which clearly shows the abrading scratches on surface formed during abrading by SiC emery papers.

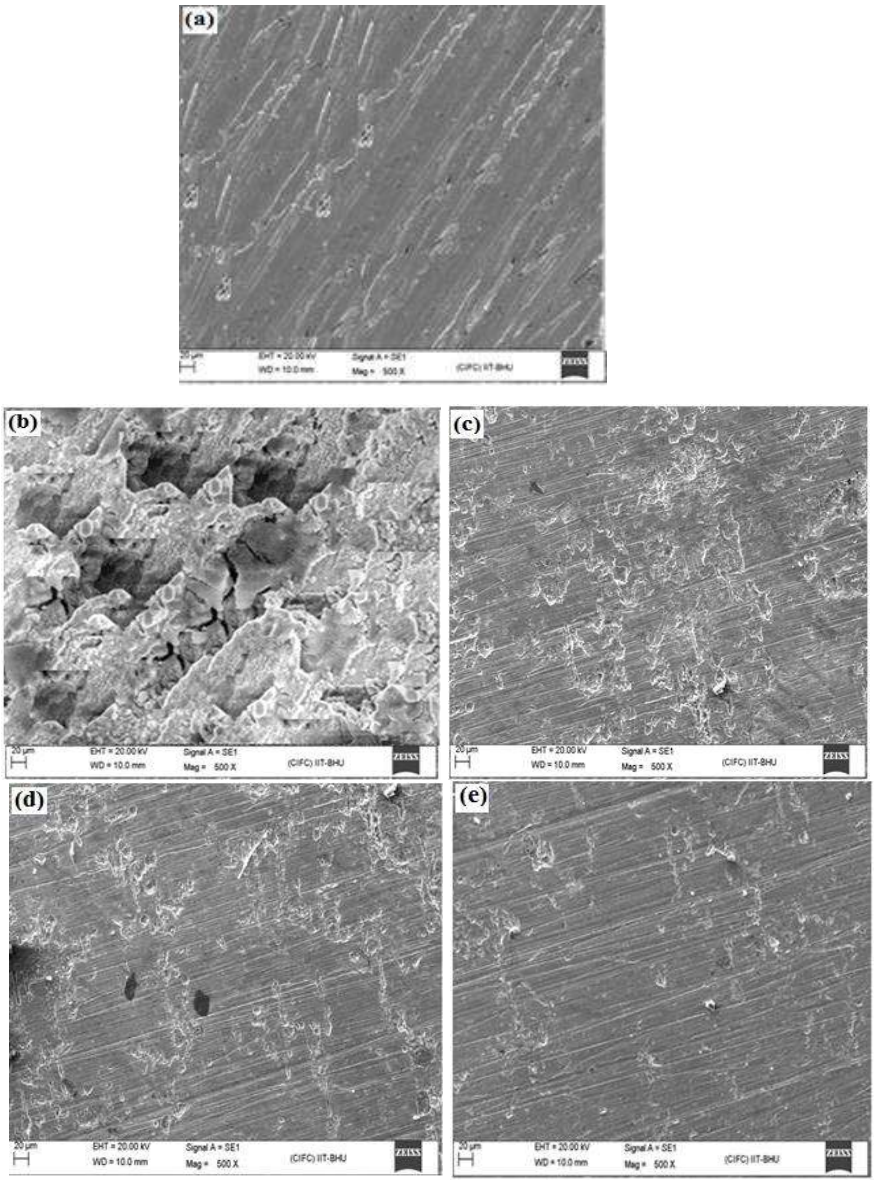


**Figure 3.2.5:** SEM images of mild steel surfaces: abraded (a), in absence of AACs (b) in the presence of 40 $mgL^{-1}$ of AAC-1(c), AAC-2(d), and AAC-3(e).

The morphology of mild steel specimen surface in Figure 3.2.5(b) in the absence of AACs, shows highly corroded and damaged surface which is attributed due to acid attack. However, in the presence of AACs, at their optimum concentration, the surface morphologies (Figure 3.2.5c-e) are remarkably smooth. By comparing the surface morphology of mild steel in absence and presence of AACs at same magnification (500x), it is seen that in presence of AACs the mild steel surfaces are relatively less corroded and less damaged, suggesting that the AACs inhibit mild steel corrosion in 1M HCl by forming a protecting surface film.

### 3.2.7. Energy dispersive X-ray (EDX) study

Figure 3.2.6 represents the EDX spectra of mild steel specimens in absence and presence of AACs at their optimum concentration. In absence of AACs the EDX spectrum shown in Figure 3.2.6(a) gives characteristics peaks of the elements (Fe, Carbon and Oxygen) constituting the mild steel specimen. The presence of low intensity signal corresponding to oxygen (O) might be due to formation of iron oxide after removal of the specimen from the uninhibited solution during SEM/EDX operation. However, in presence of optimum concentration of AACs (Figure 3.2.6b-d), the EDX spectra show additional signals for nitrogen suggesting that in the inhibited solution AACs adsorb on the metal surface and from protective surface film which is responsible for the appearances of peaks for the nitrogen in the EDX spectra of inhibited mild steel specimens. Moreover, the signals corresponding to the oxygen (O) for inhibited mild steel specimens show relatively high intensities as compared to uninhibited specimens. This

finding again suggests the adsorption of AACs on mild steel surface resulting into increased intensity of signals corresponds to the oxygen.

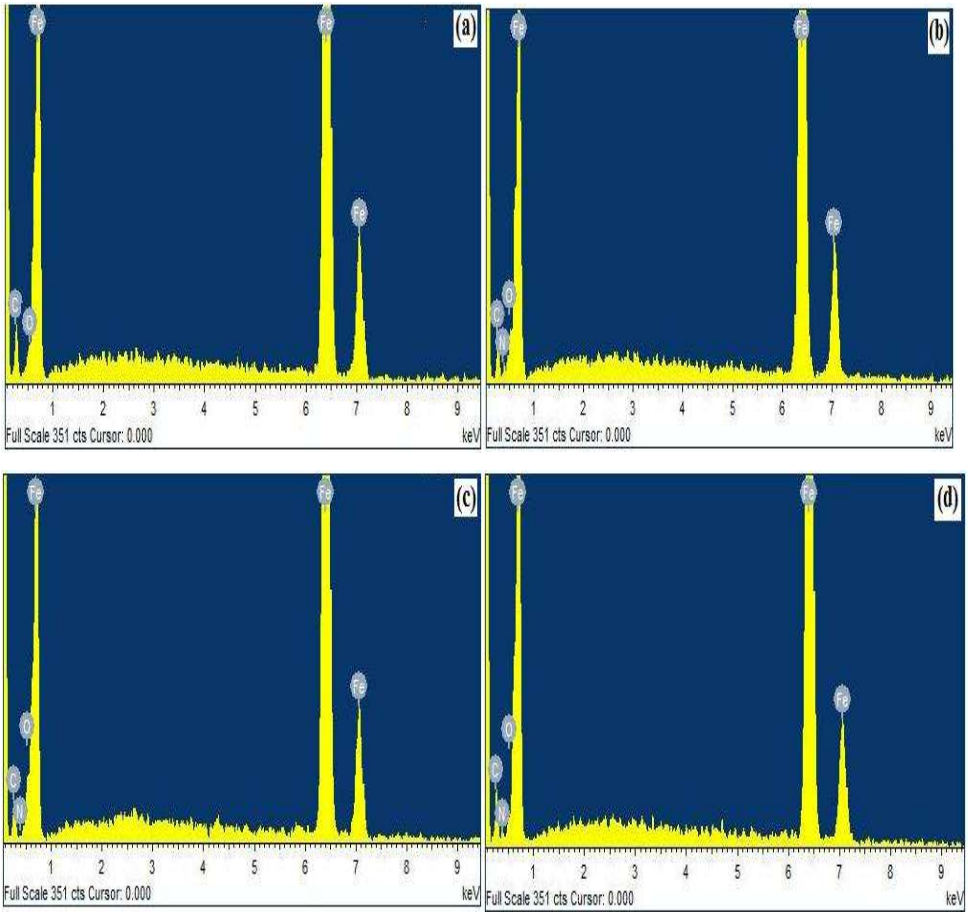


**Figure 3.2.6:** EDX images of mild steel: (a) in absence of AACs and in the presence of 40 $mgL^{-1}$ of (b) AAC-1, (c) AAC-2, and (d) AAC-3

The elemental composition of the mild steel surface obtained from EDX analysis is given in Table 3.2.7.

**Table 3.2.7:** Percentage atomic contents of elements obtained from EDX spectra for AACs

| Inhibitor | Fe | C | N | O |
|---|---|---|---|---|
| **Blank** | 62.27 | 34.94 | --- | 2.77 |
| **AAC-1** | 64.86 | 24.48 | 5.28 | 5.34 |
| **AAC-2** | 65.18 | 26.28 | 6.37 | 2.17 |
| **AAC-3** | 63.42 | 24.87 | 7.94 | 3.86 |

### 3.2.8. Atomic force microscopy (AFM) study

The 3D AFM micrographs of mild steel specimens after 3h immersion time in the absence and presence of AACs at their optimum concentration are shown in Figure 3.2.7. Figure 3.2.7a represents the surface morphology of the mild steel in absence of AACs which reveals a very rough surface. The calculated average surface roughness of the mild steel surface in absence of AACs was 392 nm.

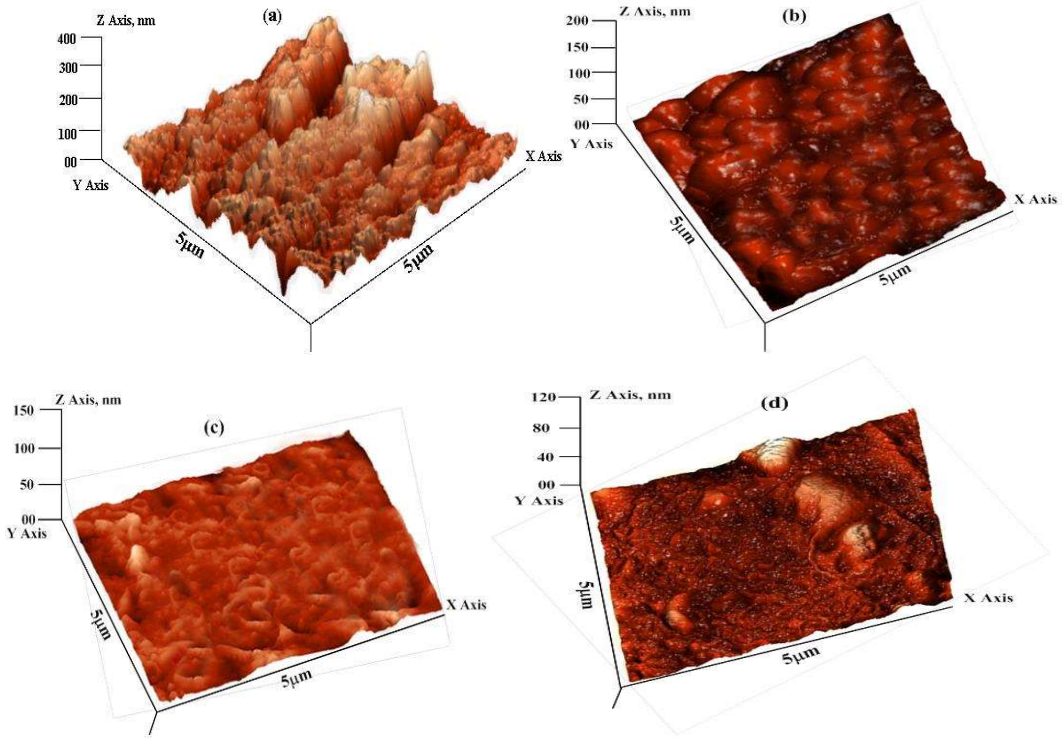


**Figure 3.2.7:** AFM images of mild steel: (a) in absence of AACs and in the presence of 40 $mgL^{-1}$ of (b) AAC-1, (c) AAC-2, and (d) AAC-3

However, in presence of AACs (Figure 3.2.7 b-d), the calculated average surface roughnesses were 194, 139 and 108 nm in presence of inhibitor AAC-1, AAC-2 and AAC-3, respectively.

### 3.2.9. Quantum chemical calculations

The optimized structures of the studied compounds showing the dihedral angles between the planes of the atoms labeled a, b, c, d are shown in Figure 3.2.8. It is apparent from Figure 3.2.8 that the phenyl group attached to the 4-position of the quinoline ring is not coplanar with the quinoline ring. Since the structural differences in the three AACs are mainly found on the 4-phenyl group substituent, it may be necessary to compare the degree of planarity/non-planarity of this phenyl group in the three compounds.

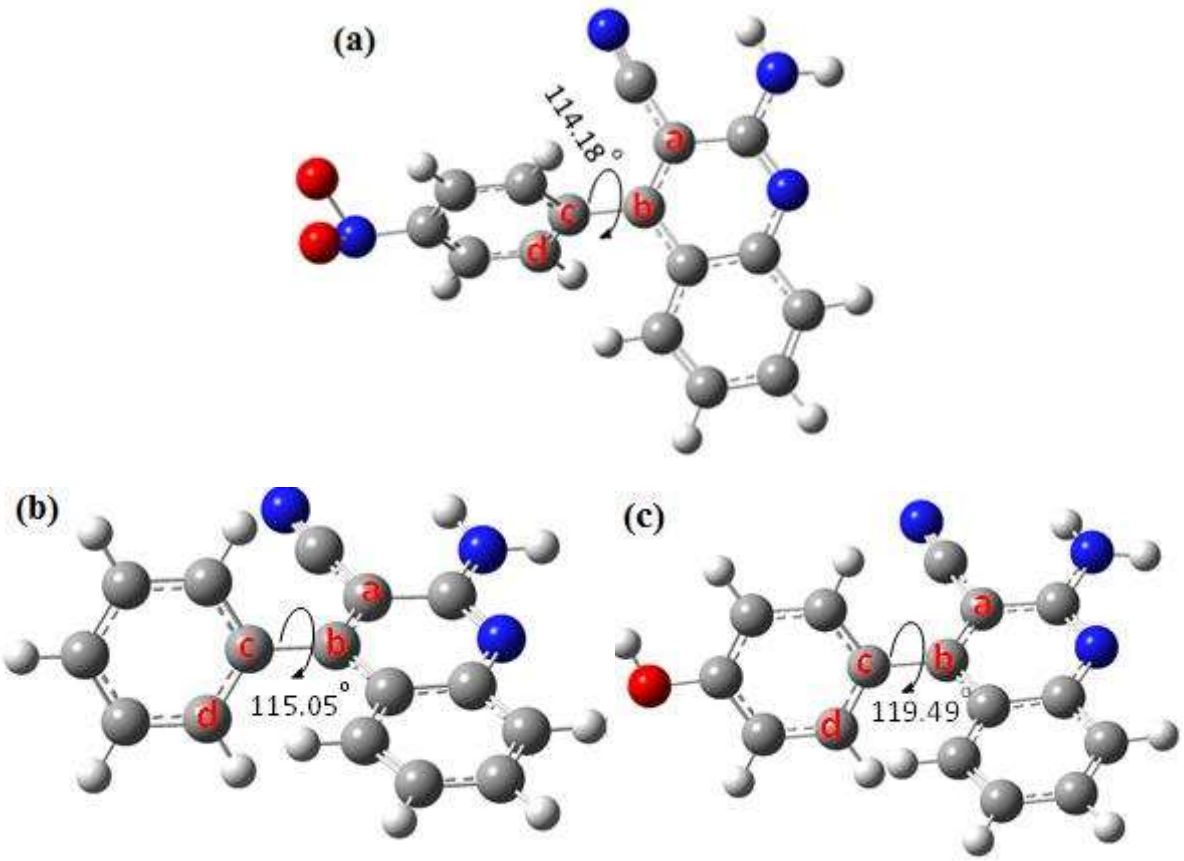


**Figure 3.2.8:** Optimized molecular structures of the studied compounds showing the dihedral angles a-b-c-d (in degrees).

This is because molecules with high degree of planarity are generally believed to exhibit higher inhibition efficiencies than their corresponding less (non)-planar analogues [Ebenso *et al.* (2012b); Arslan *et al.* (2009); Bentiss and Lagrenee (2011)]. A flat

molecule has the tendency to cover the surface of the metal optimally and also to offer enhanced electrostatic interactions between its coplanar atoms and the metallic atom.

The lower inhibition efficiency of AAC-1 is due to presence of electron-withdrawing nitro group of the 4-nitrophenyl, which reduces the electron density of the aromatic ring, and planarity of the 4-nitrophenyl group compared to AAC-2, which in turn lessens the possible electrostatic interactions between aromatic ring and metal atom [C. Verma *et al.* (2016b); C. Verma *et al.* (2015d)]. AAC-3 has electron releasing –OH substituent group at positions 4 making it better inhibitor than AAC-2 without any substituent. The frontier molecular orbitals provide information about the prospective sites of the molecules involved in donor-acceptor relationship between the inhibitor molecules and the metal atom. The HOMO and LUMO electron density distributions of the studied compounds are shown in Figure 3.2.9. The HOMO electron densities of AAC-1 and AAC-2 are essentially distributed on the atoms in the quinoline ring and extended to the N atom of the amino group attached to the position 2 of the ring. This suggests that the quinoline rings in AAC-1 and AAC-2 play a major role in donating π-electrons to the vacant d-orbital of Fe. There is also the tendency of the 2-amino group donating σ-electrons to the vacant d-orbital of the Fe. For AAC-3, the HOMO electron densities are distributed over the entire quinoline rings and extended to the 4-hydroxylphenyl and the 2-amino groups. This suggests that the quinoline ring, the 4-hydroxylphenyl and the 2-amino groups are likely to participate in donating electrons to the appropriate vacant orbitals of the Fe for effective corrosion inhibition. The LUMO electron densities in the three compounds are nearly distributed over the entire molecular areas. This suggests that the compounds are capable of accepting electrons from the appropriate occupied orbitals of the Fe atom during the donor-acceptor interactions. The calculated quantum chemical parameters are listed in Table 3.2.8.

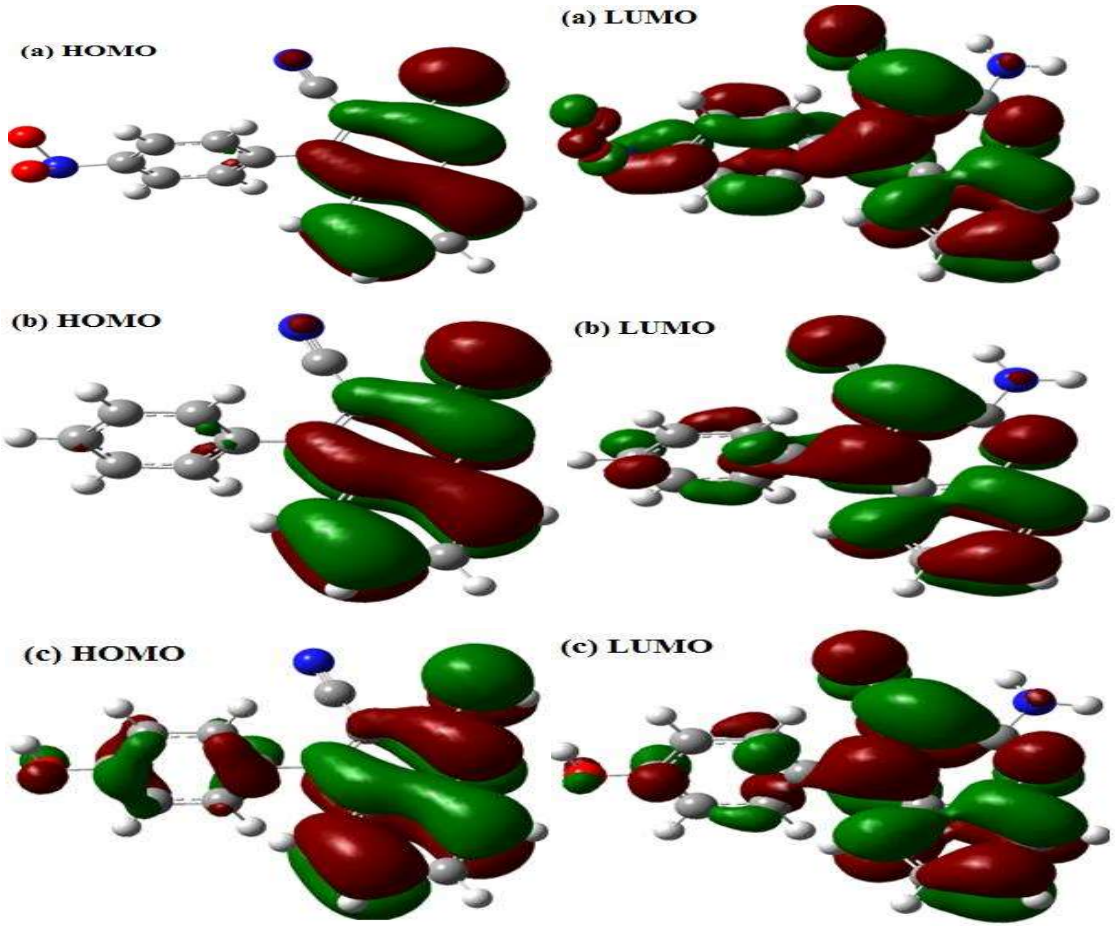


**Figure 3.2.9:** The frontier molecular orbital of studied AACs (a) AAC-1 (left, HOMO; right, LUMO), (b) AAC-2 (left, HOMO; right, LUMO) and (c) AAC-3 (left, HOMO; right, LUMO)

The $E_{HOMO}$ is a measure of the tendency of a molecule to donate its HOMO electrons to the appropriate vacant orbital of an electron-acceptor during the donor-acceptor interactions. The higher the value of the $E_{HOMO}$ the better will be chance of electron donation by the donor molecule. The results in Table 3.2.8 show that the trend of the $E_{HOMO}$ for the studied compounds is: AAC-3 > AAC-2 > AAC-1, which corresponds to the trend of the observed inhibition efficiency. The $E_{LUMO}$ on the other hand is a measure of the tendency of a molecule to accept electrons into its LUMO from the appropriate occupied orbital of an electron-donor. That is, the lower the value of the $E_{LUMO}$ the better the chance of electron acceptance by the acceptor molecule. The values of the $E_{LUMO}$ obtained for the studied compounds do not correlate with the observed $\eta$%.

The opposite trends of the $E_{LUMO}$ values and the $\eta$% suggest that the inhibition potentials of the studied AACs are not informed by their ability to receive electrons from the occupied orbitals of Fe. Similarly, the values of the energy gap ($\Delta E$) and the global hardness ($\eta$) often employed as indices of relative reactivity or stability of a molecule do not correlate with the observed $\eta$%. However, the values of the global electronegativity ($\chi$) show that AAC-3 has the least tendency to hold on to its electrons or the highest propensity to release its electrons in a favorable donor-acceptor mechanism. The trend of the $\chi$ results is in complete agreement with the observed η%. The fraction of electrons transferred ($\Delta N$) from an inhibitor molecule to the metal atom can be used as the gauge of the relative performance of a set of inhibitor molecules in electron transfer process. The results in Table 3.2.8 show that the trend of ΔN is AAC-3 > AAC-2 > AAC-1, which is in conformity with the trend of the observed $\eta$%.

According to Gomez et al., the change in energy ($\Delta E_T$) that accompanies the electron transfer process from an inhibitor to a metal atom can be used to predict the favorability of the donor-acceptor interactions between the interacting species. A negative value of $\Delta E_T$ though does not really predict the occurrence of back-donation; it is an indication that the charge transfer to a molecule, followed by a back-donation from the molecule is energetically favorable. Suppose there is any chance of charge transfer from Fe to the studied inhibitors and also retro-donation from the inhibitor molecules to the Fe, the more negative the value of $\Delta E_T$ the better the stabilization of the product of the donor-acceptor relationship. The results in Table 3.2.8 suggest that AAC-3 will form a more stable inhibitor-Fe complex compared to the AAC-1 and AAC-2, the trend of $\Delta E_T$ values is in agreement with the experimentally observed $\eta$%.

**Table 3.2.8:** Quantum chemical parameters derived from the B3LYP/6-31+G(d,p) method

| **Parameters→ Inhibitors↓** | $E_{HOMO}$ (eV) | $E_{LUMO}$ (eV) | $\Delta E$ (eV) | $\eta$ (eV) | $\chi$ (eV) | $\Delta N$ | $\Delta E_T$ |
|---|---|---|---|---|---|---|---|
| **AAC-1** | -6.456 | -2.584 | 3.872 | 1.936 | 4.520 | 0.640 | -0.484 |
| **AAC-2** | -6.225 | -2.257 | 3.968 | 1.984 | 4.241 | 0.695 | -0.496 |
| **AAC-3** | -6.114 | -2.121 | 3.993 | 1.996 | 4.117 | 0.722 | -0.499 |

## 3.3. 2, 4-diamino-5-(phenylthio)-5H-chromeno [2, 3-b] pyridine-3-carbonitriles as corrosion inhibitors

It is reported in literature that S- containing compounds show better inhibition efficiency in sulphuric acid solution, while N- containing compounds show better inhibition efficiency in hydrochloric acid solution [Fekry and Mohamed (2010)]. Whereas, compounds containing both N- and S- atoms generally give rise to even better inhibition efficiency [Soltani *et al.* (2015), Tang *et al.* (2010)]. In view of this, we studied the corrosion inhibition behavior of three chromenopyridines namely, 2,4-diamino-7-nitro-5-(phenylthio)-5H-chromeno[2,3-b]pyridine-3-carbonitrile (DHPC-1), 2,4-diamino-5-(phenylthio)-5H-chromeno[2,3-b]pyridine-3-carbonitrile (DHPC-2) and 2,4-diamino-7-hydroxy-5-(phenylthio)-5H-chromeno[2,3-b]pyridine-3-carbonitrile (DHPC-3) on corrosion of mild steel in 1 M HCl. The investigated chromenopyridines were synthesized by multicomponent reactions (MCRs). All inhibition tests were performed using weight loss, potentiodynamic polarization, and electrochemical impedance spectroscopy (EIS). Surface morphology was studied using scanning electron microscopy (SEM), and atomic force microscopy (AFM). Quantum chemical and molecular dynamics calculations were also performed to corroborate experimental results. The choice of these compounds as corrosion inhibitors is based on the consideration that they can be easily synthesized via green method using readily available chemicals in one step. These compounds are highly soluble in the test solution. Literature survey reveals that chromenopyridines has not been reported earlier, which portrays the compounds to be novel potential corrosion inhibitors. The IUPAC name, molecular structure, and abbreviation of the studied DHPCs are given in Table 3.3.1.

### 3.3.1. Gravimetric measurements

The weight loss experiments were carried out for 3 h immersion time at 308 K in the absence and presence of different concentrations of the studied compounds. The calculated weight loss parameters such as corrosion rate ($C_R$), surface coverage ($\theta$) and corresponding inhibition efficiencies ($\eta$%) are given in Table 3.3.2. From the results shown in Table 3.3.2 it can be seen that the inhibition efficiency of the three compounds increases with increasing concentration. The maximum inhibition efficiency was obtained at 12.70 x $10^{-5}$ molL$^{-1}$ concentration. Further increase in DHPCs concentration did not cause any significant change in the inhibition performance. The relative strengths of inhibition the studied compounds follow the order DHPC-3 > DHPC-2 > DHPC-1. The highest inhibition efficiency of the DHPC-3 among the studied inhibitors is attributed to the presence of the electron donating –OH group at position seven of the chromenopyridine ring. In contrast, the lowest inhibition efficiency of the DHPC-1 could be as a result of electron withdrawing nature of the -$NO_2$ group substituted at position seven of the chromenopyridine ring [Verma *et al.* (2015d)].

### 3.3.2. Effect of temperature

In order to study the influence of temperature on the corrosion inhibition efficiency of the investigated inhibitors, the weight loss experiments were carried out at different temperatures (308-338K) in the absence and presence of optimum concentration of the DHPCs. It is observed from the results depicted in Table 3.3.3 that the corrosion rate increases and inhibition efficiency decreases with increasing inhibitors concentration. The increased corrosion rate at elevated temperature could be as a result of increased average molecular speed of the inhibitor molecules that weakens the adsorption tendency of the inhibitors on the metallic surface [Ehsani *et al.* (2014)].

**Table 3.3.1:** IUPAC names, molecular structures, and abbreviations of the studied DHPCs.

| S.No. | IUPAC name | Chemical Structure | Abbreviation |
|---|---|---|---|
| **1** | 2,4-diamino-7-nitro-5-(phenylthio)-5Hchromeno[2,3-b]pyridine-3-carbonitrile | 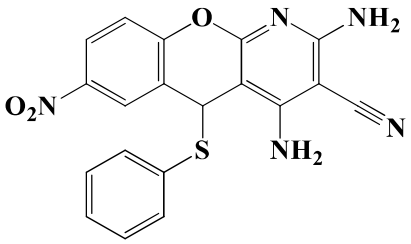 | **DHPC-1** |
| **2** | 2, 4-diamino-5-(phenylthio)-5H-chromeno [2, 3-b] pyridine-3-carbonitrile | 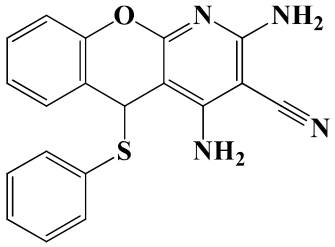 | **DHPC-2** |
| **3** | 2,4-diamino-7-hydroxy-5-(phenylthio)-5H-chromeno[2,3-b]pyridine-3-carbonitrile | 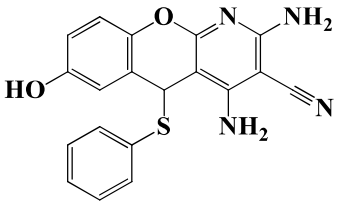 | **DHPC-3** |

The Arrhenius plots shown in Figure 3.3.1(a) give a straight line between log $C_R$ versus $1/T$ from the slopes ($-\Delta E_a/2.303R$) of which values of activation energies were calculated for all the inhibitors. In presence of DHPCs, $E_a$ values of 69.89 kJmol$^{-1}$ for

DHPC-1, 76.54 kJmol$^{-1}$ for DHPC-2, and 84.38 kJmol$^{-1}$ for DHPC-3, are respectively while the value of $E_a$ is $E_a$ = 28.48 kJmol$^{-1}$ in their absence.

**Table 3.3.2:** The weight loss parameters obtained for mild steel in 1 M HCl containing different concentrations of DHPCs

| inhibitor | Conc (mol/L) | $C_R$ (mg cm$^{-2}$ h$^{-1}$) | Inhibition efficiency ($\eta$ %) | ($\theta$) |
|---|---|---|---|---|
| **Blank** | 0.0 | 7.66 | --- | --- |
| **DHPC-1** | 2.55 x 10$^{-5}$ | 2.86 | 62.66 | 0.6266 |
| | 5.11 x 10$^{-5}$ | 1.20 | 84.33 | 0.8433 |
| | 7.67 x 10$^{-5}$ | 0.73 | 90.46 | 0.9046 |
| | 10.22 x 10$^{-5}$ | 0.53 | 93.08 | 0.9308 |
| | 12.70 x 10$^{-5}$ | 0.36 | 95.30 | 0.9530 |
| **DHPC-2** | 2.55 x 10$^{-5}$ | 2.46 | 67.88 | 0.6788 |
| | 5.11 x 10$^{-5}$ | 1.03 | 86.55 | 0.8655 |
| | 7.67 x 10$^{-5}$ | 0.60 | 92.16 | 0.9216 |
| | 10.22 x 10$^{-5}$ | 0.40 | 94.77 | 0.9477 |
| | 12.70 x 10$^{-5}$ | 0.26 | 96.60 | 0.9660 |
| **DHPC-3** | 2.55 x 10$^{-5}$ | 2.10 | 72.58 | 0.7258 |
| | 5.11 x 10$^{-5}$ | 0.86 | 88.77 | 0.8877 |
| | 7.67 x 10$^{-5}$ | 0.46 | 93.99 | 0.9399 |
| | 10.22 x 10$^{-5}$ | 0.33 | 95.69 | 0.9569 |
| | 12.70 x 10$^{-5}$ | 0.16 | 97.91 | 0.9791 |

**Table 3.3.3:** Variation of $C_R$ and $\eta$ % with temperature in the absence and presence of optimum concentration of DHPCs in 1M HCl

| Temperature (K | Corrosion rate ($C_R$) (mg cm$^{-2}$ h$^{-1}$) and Inhibition efficiency ($\eta$%) | | | | | | | |
|---|---|---|---|---|---|---|---|---|
| | Blank | | DHPC-1 | | DHPC-2 | | DHPC-3 | |
| | $C_R$ | $\eta$% | $C_R$ | $\eta$% | $C_R$ | $\eta$% | $C_R$ | $\eta$% |
| **308** | 7.66 | --- | 0.36 | 95.30 | 0.26 | 96.60 | 0.16 | 97.91 |
| **318** | 11.0 | --- | 0.96 | 91.27 | 0.76 | 93.09 | 0.46 | 95.81 |
| **328** | 14.3 | --- | 2.10 | 85.31 | 1.73 | 87.90 | 1.20 | 91.60 |
| **338** | 18.6 | --- | 4.23 | 77.25 | 3.80 | 79.56 | 3.23 | 82.63 |

It was further observed that the order of $E_a$ was consisted with order of inhibition efficiency i.e. a higher value of $E_a$ was observed for a more efficient inhibitor. The increased values of $E_a$ in the presence of DHPCs suggested that higher energy barrier has been established for the corrosion reactions due to the adsorption of the inhibitors on the metallic surface [Weder *et al.* (2016)].

### 3.3.3. Adsorption isotherm

In the present study, the calculated surface coverage at different concentrations of the investigated inhibitors was subjected to different adsorption isotherm models in order to find best adsorption isotherm. However, the Langmuir adsorption isotherm gives the best fit having values of regression coefficient ($R^2$) very close to unity.

The Langmuir isotherm [Figure 3.3.1(b)] gives straight lines for the plots of log $\theta$/1-$\theta$ versus log $C$ from which values of $K_{ads}$ were calculated for the studied inhibitors. The $K_{ads}$ is related to the Gibbs' free energy of adsorption according to the equation:

$$\Delta G^{o}_{ads} = -RT \ln(55.5 K_{ads}) \qquad (10)$$

where $T$ is the absolute temperature and R is the universal gas constant. The numerical value of 55.5 represents the molar concentration of water in acid solution. The calculated values of $K_{ads}$ and $\Delta G^0_{ads}$ are given in Table 3.3.4. Generally, the value of $K_{ads}$ represents the affinity of inhibitor for adsorption on the metallic surface and a high value of $K_{ads}$ is consistent with high adsorption ability. In the present study the values of $K_{ads}$ for the studied inhibitors follow the order DHPC-3 > DHPC-2 > DHPC-1, which is in accordance with the order of inhibition efficiency.

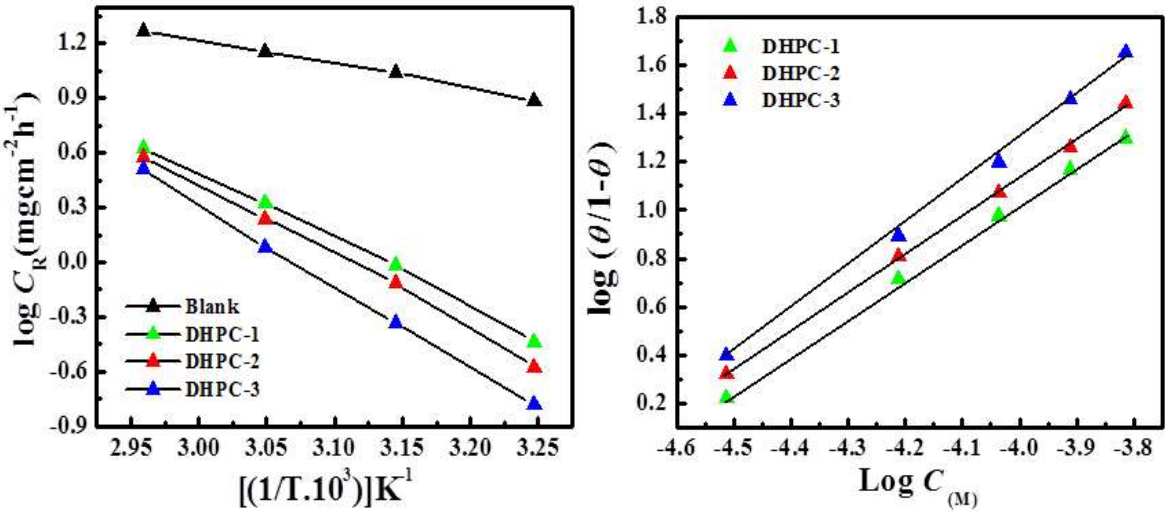


**Figure 3.3.1:** (a) Arrhenius plots for the corrosion of mild steel in 1 M HCl in the presence of the studied inhibitors (b) Langmuir adsorption isotherms for mild steel in 1 M HCl in the presence of the studied DHPCs at different concentration

The large negative values of $\Delta G^0_{ads}$ for the studied inhibitors indicate that these compounds possessed strong tendency to adsorb spontaneously on the mild steel surface [Amin and Ibrahim (2011); Issaadi *et al.* (2011)]. Literature survey reveals that the values of $\Delta G^0_{ads}$ in between -20 kJ mol$^{-1}$ to -40 kJ mol$^{-1}$ are consistent with physiochemisorption. In our present case, the values of $\Delta G^0_{ads}$ varies from -34.66 kJ mol$^{-1}$ to 38.19 kJ mol$^{-1}$ suggesting that the adsorption of the investigated inhibitors on mild steel surface involves electrostatic interaction between charged inhibitors and charged mild steel surface (physisorption) as well as charge sharing or transfer from the inhibitor molecules to the

metal surface to form a coordinate type of bond (chemisorption) [Amin *et al.* (2011); Bentiss *et al.* (2005)].

**Table 3.3.4:** The values of $K_{ads}$ and $\Delta G^{\circ}_{ads}$ for mild steel in 1 M HCl in the absence and presence of optimum concentration of DHPCs at different temperatures.

| **inhibitor** | **$K_{ads}$ ($10^4$ $M^{-1}$)** | | | | **$-\Delta G^{\circ}_{ads}$ (k J/mol)** | | | |
|---|---|---|---|---|---|---|---|---|
| | 308 | 318 | 328 | 338 | 308 | 318 | 328 | 338 |
| **DHPC-1** | 2.38 | 1.24 | 0.69 | 0.40 | 36.10 | 35.56 | 35.10 | 34.66 |
| **DHPC-2** | 3.32 | 1.60 | 0.87 | 0.46 | 36.96 | 36.22 | 35.70 | 35.05 |
| **DHPC-3** | 5.38 | 2.70 | 1.31 | 0.57 | 38.19 | 37.61 | 36.82 | 35.61 |

### 3.3.4: Potentiodynamic polarization study

The potentiodynamic polarization study was carried out in the absence and presence of different concentrations of the investigated inhibitors to gather information about kinetics of corrosion reactions. The polarization curves for mild steel dissolution in 1 M HCl with and without inhibitors are shown in Figure 3.3.2. The values of potentiodynamic polarization parameters namely, corrosion potential ($E_{corr}$), corrosion current density ($i_{corr}$), anodic and cathodic Tafel slopes ($\beta_a$, $\beta_c$) were obtained from Tafel curves. The polarization parameters along with the calculated inhibition efficiency at various concentrations of all the studied inhibitors are given in Table 3.3.5. From the results in Figure 3.3.2 and Table 3.3.5, it is observed that all the three inhibitors considerably reduced the corrosion current densities for both anodic and cathodic half-reactions, suggesting that both anodic dissolution of mild steel and cathodic reduction of hydrogen ions were inhibited. Obviously, greater decrease in the values of $i_{corr}$ was observed at high inhibitors concentration.

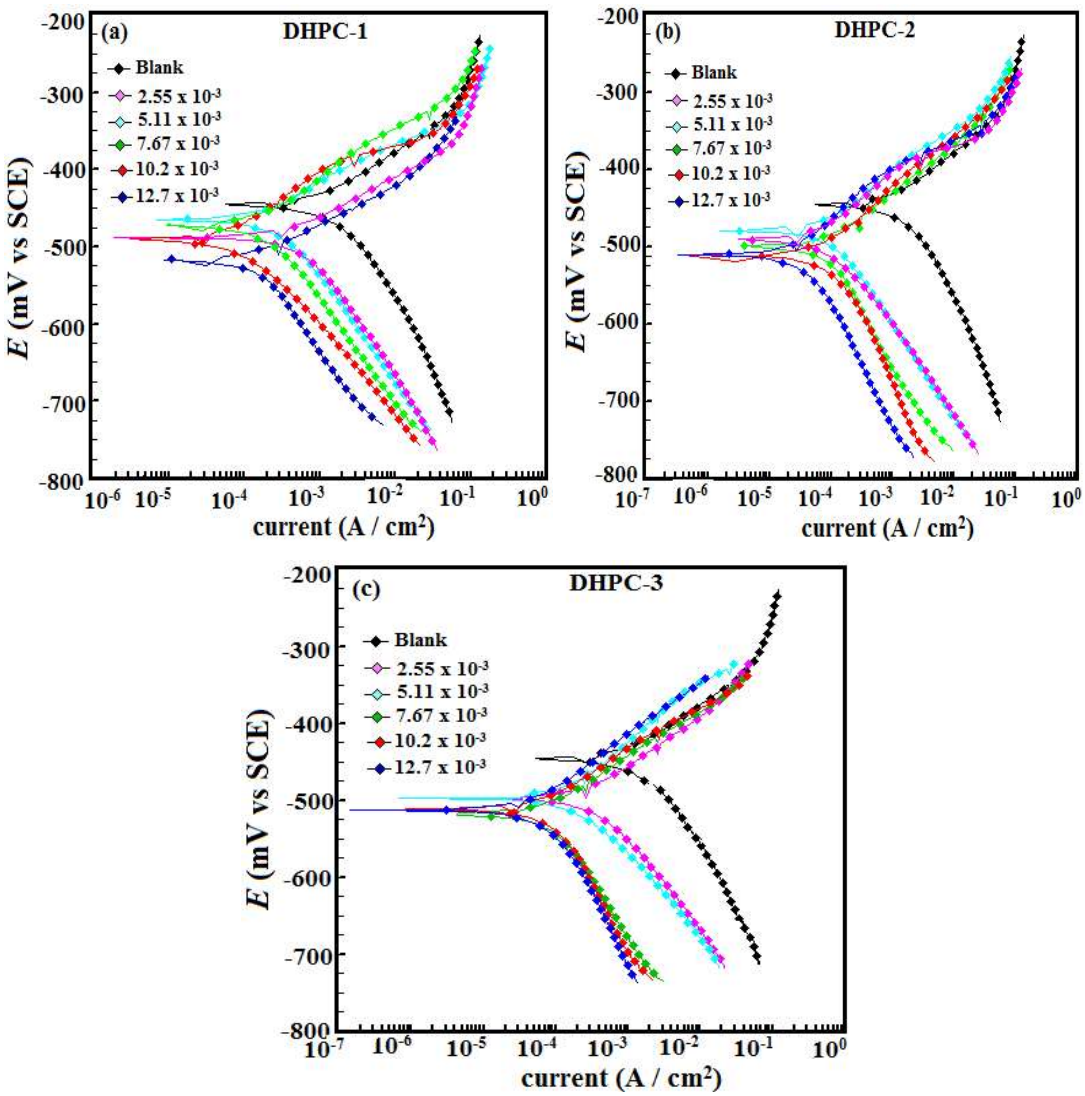


**Figure 3.3.2:** Polarization curves recorded for mild steel in the absence and presence of different concentrations DHPCs.

In general, an inhibitor can be classified as anodic or cathodic type, if the shift in the $E_{corr}$ is higher than 85 mV with respect to $E_{corr}$ of the blank, and as a mixed type inhibitor, if shift in $E_{corr}$ is lower 85 mV [Yıldız *et al.* (2014); Solmaz (2014)]. In our present investigation maximum displacement in the $E_{corr}$ values were 72 mV for DHPC-1, 70 mV for DHPC-2 and 72 mV for DHPC-3. It can also be observed from the results in Table 3.3.5 that the change in the values of $\beta_c$ are more prominent as compared to that of $\beta_a$, suggesting that the studied compounds mixed type inhibitors with predominantly cathodic inhibitive effects.

**Table 3.3.5:** Tafel polarization parameters for mild steel in 1 M HCl solution in the absence and presence of different concentrations of DHPCs.

| Inhibitor | Conc molL$^{-1}$ | $E_{corr}$ (mV/ SCE) | $\beta_a$ ($\mu$A/cm$^2$) | $\beta_c$ (mV/dec) | $i_{corr}$ (mV/dec) | $\eta$% |
|---|---|---|---|---|---|---|
| **Blank** | --- | -445 | 70.5 | 114.6 | 1150 | ---- |
| **DHPC-1** | 2.55 x 10$^{-5}$ | -487 | 62.0 | 129.5 | 438.6 | 61.68 |
| | 5.11 x 10$^{-5}$ | -472 | 74.5 | 110.3 | 156.0 | 86.43 |
| | 7.67 x 10$^{-5}$ | -474 | 57.9 | 105.5 | 114.3 | 90.06 |
| | 10.2 x 10$^{-5}$ | -491 | 74.4 | 84.6 | 67.6 | 94.12 |
| | 12.7 x 10$^{-5}$ | -517 | 65.4 | 60.4 | 46.8 | 95.93 |
| **DHPC-2** | 2.55 x 10$^{-5}$ | -507 | 68.7 | 144.4 | 384.0 | 66.60 |
| | 5.11 x 10$^{-5}$ | -496 | 76.6 | 129.7 | 154.3 | 86.58 |
| | 7.67 x 10$^{-5}$ | -509 | 69.5 | 122.7 | 94.2 | 91.80 |
| | 10.2 x 10$^{-5}$ | -515 | 110.0 | 120.6 | 42.6 | 96.29 |
| | 12.7 x 10$^{-5}$ | -513 | 69.5 | 162.3 | 28.4 | 97.53 |
| **DHPC-3** | 2.55 x 10$^{-5}$ | -497 | 74.0 | 106.6 | 286.3 | 75.10 |
| | 5.11 x 10$^{-5}$ | -496 | 91.6 | 88.7 | 144.0 | 87.47 |
| | 7.67 x 10$^{-5}$ | -517 | 74.7 | 156.4 | 78.4 | 93.18 |
| | 10.2 x 10$^{-5}$ | -511 | 72.4 | 142.7 | 34.6 | 96.99 |
| | 12.7 x 10$^{-5}$ | -512 | 88.5 | 143.7 | 22.6 | 98.03 |

### 3.3.5. Electrochemical impedance spectroscopy (EIS)

The EIS is a widely used technique to understanding the mechanism of corrosion, passivation and charge transfer at the metal/electrolyte interface. The Nyquist curves for mild steel corrosion in 1 M HCl without and with various concentrations of the studied inhibitors obtained after 30 min immersion time are given Figure 3.3.3. It is noticeable that the shapes of Nyquist plots are similar for all the systems, which suggest that presence of inhibitors did not cause any significant change in the corrosion mechanism. In the present study, the Nyquist plots give imperfect capacitive semicircle, which is often associated with different phenomena such as roughness and other forms of inhomogeneities of the metal surface, distribution of the surface active sites, grain boundaries and presence of impurities [Christodoulou *et al.* (2012)]. The electrical equivalent circuit consists of the solution resistance ($R_s$), the charge transfer resistance ($R_{ct}$) and a constant phase element (CPE). In the present case, a CPE was used rather than pure double layer capacitance ($C_{dl}$) in order to take into account the mild steel surface roughness and heterogeneities, impurities, formation of porous layer, dislocation, adsorption of inhibitors, and grain boundaries. The impedance of the CPE (ZCPE) can be represented as [R. A. Bustamante *et al.* (2009); D. K. Yadav and M. A. Quraishi (2012)]. The calculated EIS parameters such as $R_s$, $R_{ct}$, $n$, $C_{dl}$, $\eta$% and surface coverage ($\theta$) are reported in Table 3.3.6. The results in Table 3.3.6 show that the values of Rct increase with increase in inhibitors concentration. The increased value of $R_{ct}$ in the presence of inhibitors is as a result of the formation of protective adsorption film on the steel surface, which isolates the metal from the aggressive acid solution [Roy *et al.* (2014); Gopi *et al.* (2015)].

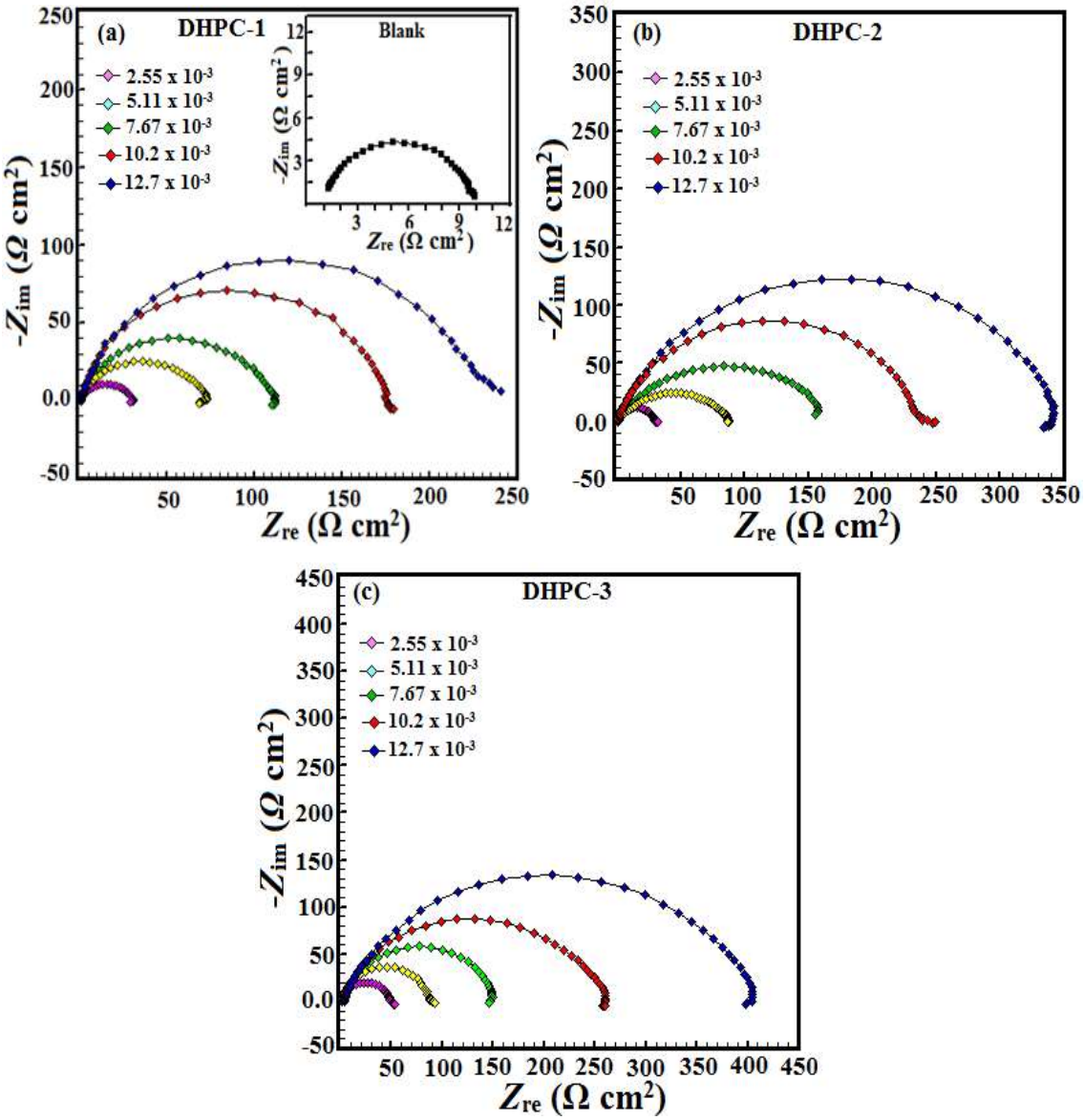


**Figure 3.3.3**: Nyquist plots recorded for mild steel in 1 M HCl in the absence and presence of different concentrations of (a) DHPC-1, (b) DHPC-2, and (c) DHPC-

The decreased value of $C_{dl}$ in the presence of the investigated inhibitors suggests a decrease in the dielectric constant and an increase in the thickness of the electrical double layer. Moreover, it is further observed that the increase in the values of $R_{ct}$ and decrease in the values of $C_{dl}$ is more pronounced at higher inhibitors concentration [Roy et *al.* (2014); Gopi *et al.* (2015)].

**Table 3.3.6:** EIS parameters obtained for mild steel in 1 M HCl in the absence and presence of different concentrations of DHPCs

| Inhibitor | Conc molL$^{-1}$ | $R_s$ ($\Omega$ cm$^2$) | $R_{ct}$ ($\Omega$ cm$^2$) | $n$ | $C_{dl}$ ($\mu F$ cm$^{-2}$) | $\eta$% |
|---|---|---|---|---|---|---|
| **Blank** | --- | 1.12 | 9.58 | 0.827 | 106.21 | ---- |
| **DHPC-1** | 2.55 x 10$^{-5}$ | 0.917 | 26.28 | 0.839 | 67.25 | 63.54 |
| | 5.11 x 10$^{-5}$ | 0.925 | 69.77 | 0.815 | 59.92 | 86.26 |
| | 7.67 x 10$^{-5}$ | 1.124 | 107.56 | 0.847 | 45.50 | 91.09 |
| | 10.2 x 10$^{-5}$ | 0.784 | 175.2 | 0.892 | 44.86 | 94.53 |
| | 12.7 x 10$^{-5}$ | 0.956 | 245.4 | 0.845 | 43.42 | 96.09 |
| **DHPC-2** | 2.55 x 10$^{-5}$ | 0.811 | 30.62 | 0.835 | 59.36 | 69.53 |
| | 5.11 x 10$^{-5}$ | 1.047 | 85.38 | 0.863 | 52.42 | 88.77 |
| | 7.67 x 10$^{-5}$ | 1.115 | 148.4 | 0.837 | 39.61 | 93.54 |
| | 10.2 x 10$^{-5}$ | 0.804 | 241.7 | 0.808 | 33.27 | 96.03 |
| | 12.7 x 10$^{-5}$ | 0.844 | 338.0 | 0.812 | 28.56 | 97.16 |
| **DHPC-3** | 2.55 x 10$^{-5}$ | 1.047 | 39.50 | 0.890 | 54.47 | 75.74 |
| | 5.11 x 10$^{-5}$ | 1.019 | 88.79 | 0.886 | 45.63 | 89.21 |
| | 7.67 x 10$^{-5}$ | 0.802 | 152.9 | 0.825 | 32.84 | 93.73 |
| | 10.2 x 10$^{-5}$ | 0.948 | 253.9 | 0.810 | 27.87 | 96.22 |
| | 12.7 x 10$^{-5}$ | 1.186 | 390.4 | 0.890 | 23.11 | 97.54 |

The Bode phase and impedance plots for mild steel in the absence and presence of different concentrations of the studied compounds are shown Figure 3.3.4.

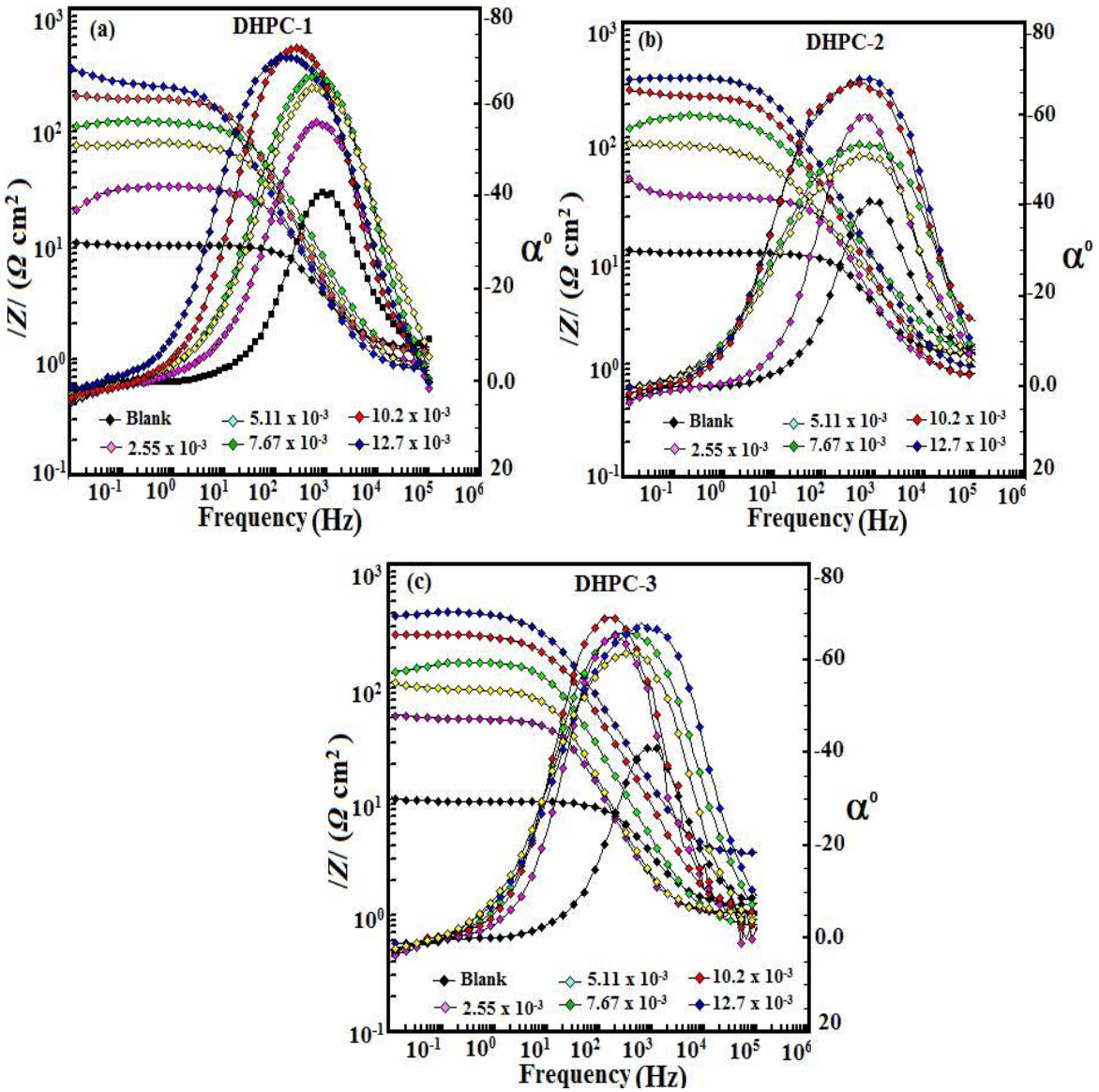


**Figure 3.3.4:** Bode impedance modulus (log *f* vs log |*Z*|) and phase angle (log *f* vs $\alpha^0$) plots for mild steel in 1 M HCl in the absence and presence of different of different concentrations of (a) DHPC-1, (b) DHPC-2, and (c) DHPC-3

Careful inspection of the Bode plots showed that the values of phase angle increase in the presence of inhibitors as compared to that of the blank acid solution. The relatively high values of phase angles in presence of the inhibitors is attributed to increased surface smoothness of the mild steel specimens, which may be due to adsorption of the inhibitors on the steel surface [Verma *et al.* (2015a); Ebenso *et al.* (2012b)]. However, the ideal capacitive behavior of electric double layer was not

observed in the present study, as the value of phase angle and slope could not achieved at $90^0$ and -1, respectively [Verma *et al.* (2015a); Ebenso *et al.* (2012a)]. The deviation from ideal capacitive behavior in this study is due to surface inhomogeneities of structural and interfacial origin.

### 3.3.6. Scanning electron microscopy (SEM)

SEM images shown in Figure 3.3.5 revealed that the mild steel surface immersed for 3h in the blank acid solution [Figure 3.3.5(a)] showed highly corroded and damaged surface with mountain like appearance, which is due to the free acid corrosion of mild steel in the absence of the inhibitors.

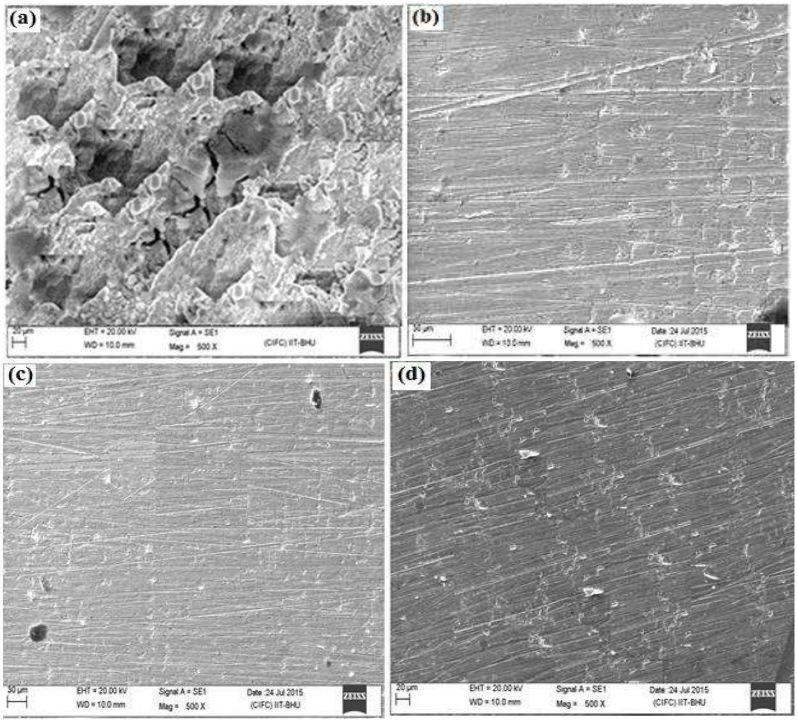


**Figure 3.3.5:** SEM images of mild steel surfaces in 1 M HCl in the absence of DHPCs (a), and in 1 M HCl in the presence of optimum concentration of DHPC-1 (b), DHPC-2 and (c), DHPC-3 (d).

However, in the presence of the inhibitors [Figure 3.3.5(b-d)], the surface morphology of the mild steel specimens were remarkably smoothened, which may be as a

result of the formation of the protective film of the inhibitor molecules on the mild steel surface.

### 3.3.7. Atomic force microscopy (AFM)

The surface of mild steel specimen in the absence of inhibitors was highly corroded, rough and inhomogeneous as shown in Figure 3.3.6(a).

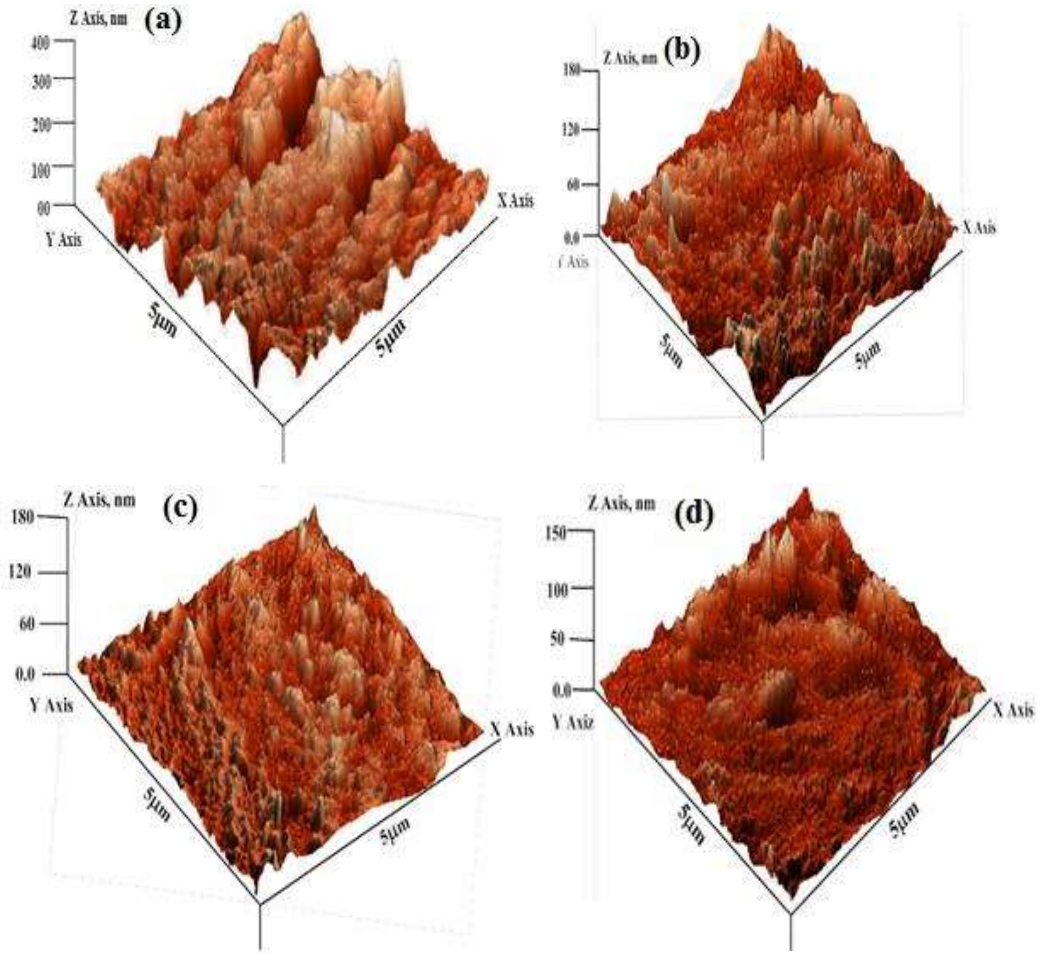


**Figure 3.3.6:** AFM images of mild steel surfaces in 1 M HCl in the absence of DHPCs (a), and in 1 M HCl containing optimum concentration of DHPC-1 (b)DHPC-2 and (c), DHPC-3(d)

For the mild steel specimen corroded in free acid solution without inhibitors, the calculated surface roughness is 392 nm. However, in the presence of optimum concentration of the studied inhibitors there is significant improvement in the surface

smoothness, which is attributed to the adsorption of the inhibitors on mild steel surface and consequently isolation of the metal surface from corrosive medium. The calculated surface roughness decreased to 156, 134, and 108 nm in the presence of DHPC-1, DHPC-2 and DHPC-3, respectively. From the AFM images shown in Figure 3.3.6, it can be observed that the degree of surface smoothness is in the order DHPC-3 > DHPC-2 > DHPC-1, which is in accordance with the order of the experimental inhibition efficiencies.

### 3.3.8. Quantum chemical calculations

The ground state optimized structures of the studied compounds are shown in Figure 3.3.7. The most stable geometries of the three DHPCs correspond to the molecular structures in which the benzenethiolyl group is twisted out of plane and non-coplanar with the chromenopyridine ring. Electron density isosurfaces of the highest occupied molecular orbital (HOMO) and lowest unoccupied molecular orbital (LUMO) of the studied DHPCs are also shown in Figure 3.3.8. The HOMO provides information about the molecular orbitals of the inhibitor that may interact with atomic orbitals of the metal via charge donation to the appropriate vacant or partially filled metallic orbitals. The HOMOs of the three compounds comprise both σ- and π-type orbitals and distributed over the entire rings contained in the molecules. In all the three DHPCs, the $–NH_2$ group at the 4-position on the pyridine ring makes little or no contributions to the HOMO. In DHPC-3, the N-atom in the pyridine ring does not contribute to the HOMO. The $-NO_2$ group on the chromene ring of DHPC-1 does not seem to contribute to the HOMO. In all the three compounds, the S-atom of the benzenethiolyl group contributes significantly to the HOMO and shows the tendency of donating charges to the appropriate vacant orbitals of Fe via σ-type HOMOs.

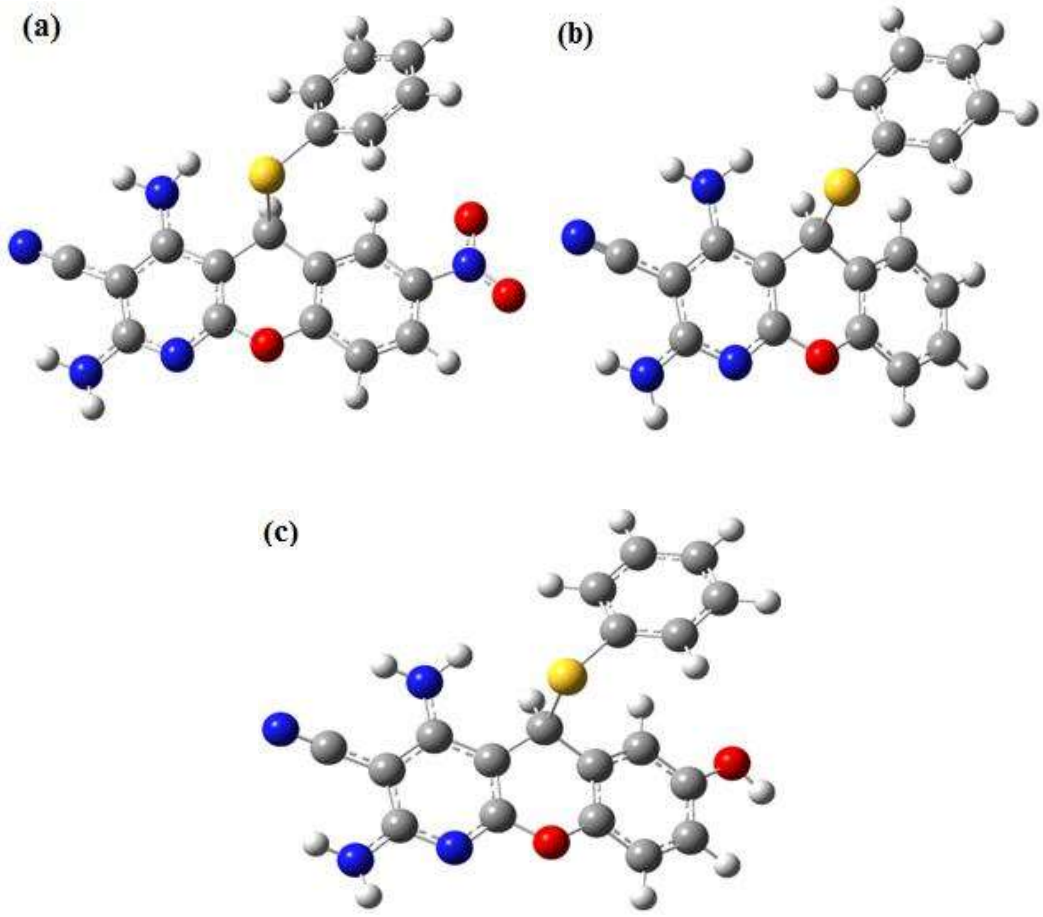


**Figure 3.3.7:** Optimized molecular structures of (a) DHPC-1, (b) DHPC-2, and (c) DHPC-3

The LUMO provides information about the molecular orbitals of the inhibitor that may interact with atomic orbitals of the metal by accepting charges from the occupied orbitals of the metallic atom in a retro-donation step. In all the three compounds, the C-atoms in the chromene ring are well involved in the LUMO. The LUMO is also well distributed on the benzenethiolyl group in both DHPC-2 and DHPC-3. However, the benzenethiolyl group does not contribute to the LUMO in DHPC-1. This observation can be attributed to the electron-withdrawing effect of the $–NO_2$ group on the chromene ring of DHPC-1, which may pull the electron density of the benzenethiolyl group towards the chromene ring, and inductively assisted by the highly electronegative S-atom.

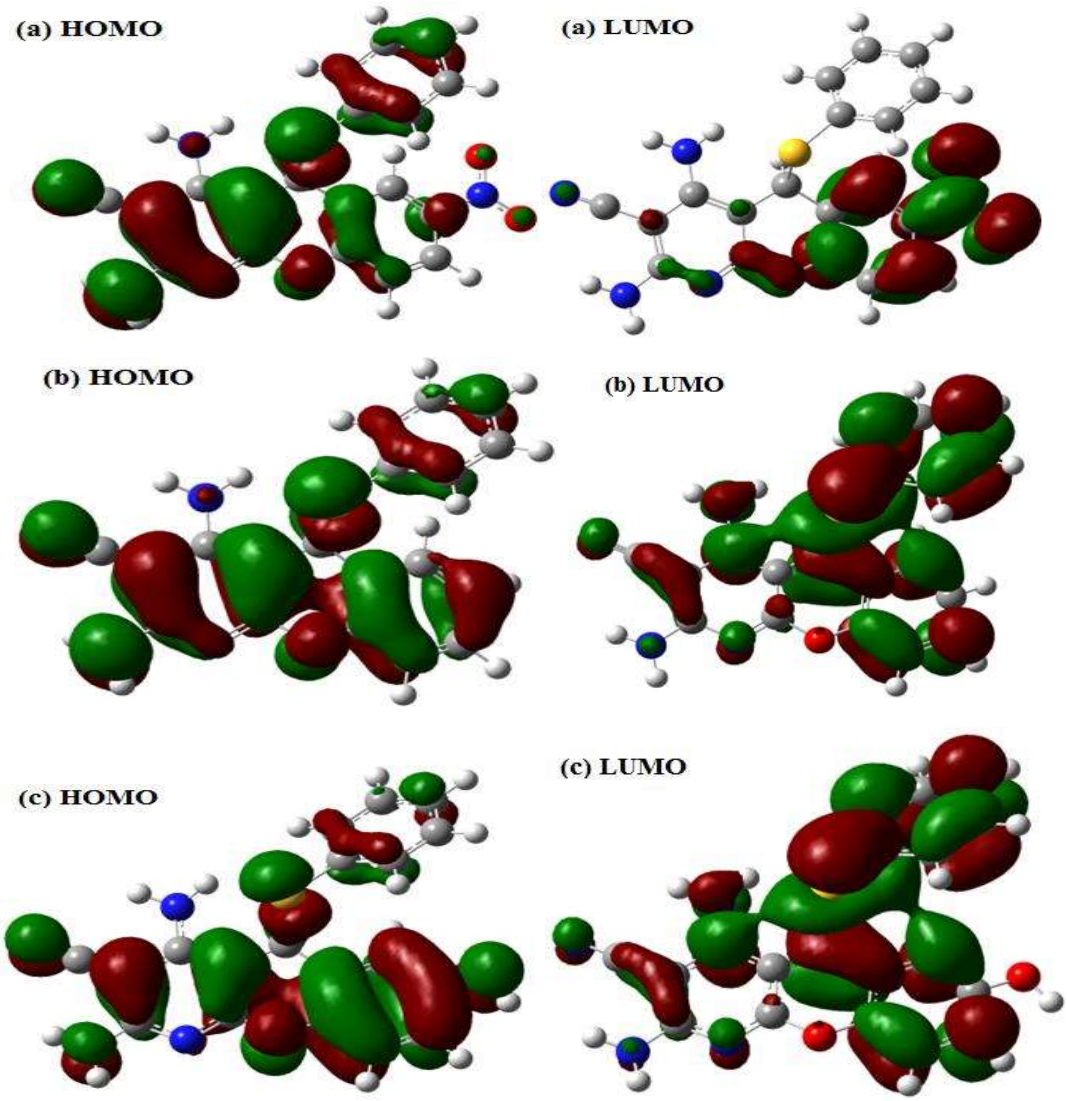


**Figure 3.3.8:** The frontier molecular orbital (left-hand side: HOMO; and right-hand side: LUMO) of the studied DHPCs (a) DHPC-1 (b) DHPC-2, and (c) DHPC-3.

The N-containing substituent groups on the pyridine ring in DHPC-1 do not contribute to the LUMO, suggesting that these groups cannot participate in backward-donation of charges during the donor-acceptor interactions between DHPC-1 molecule and Fe. This generalization cannot be made for DHPC-2 and DHPC-3. The values of some relevant quantum chemical parameters for the studied inhibitor molecules are listed in Table 3.3.7. The donor-acceptor interactions between an inhibitor molecule and a metal atom are usually correlated with the FMO energies and other related reactivity indices. Generally, the higher the $E_{HOMO}$, the better the tendency of an inhibitor molecule to

donate electrons to the metal, and the lower the $E_{LUMO}$ the better the tendency of an inhibitor molecule to accept electrons from the metal. A low value of the energy gap ($\Delta E$) is also an indication of high reactivity of the inhibitor molecule. For a group of inhibitor molecules with similar molecular architectures, the compound with a higher $E_{HOMO}$, a lower $E_{LUMO}$ and a lower $\Delta E$ usually exhibits higher inhibition efficiency. The results in Table 3.3.7 show that the values of $E_{HOMO}$ for the three compounds are in the order: DHPC-3 > DHPC-2 > DHPC-1, which is in agreement with the order of inhibition efficiency of the compounds. This observation suggests that the higher the tendency of a DHPC molecule to donate its least stable electron(s) to the appropriate vacant orbitals of the metal atom, the higher the inhibition efficiency. The values of $E_{LUMO}$ and $\Delta E$ listed in Table 3.3.7 do not agree with the observed order of inhibition efficiency. Global electronegativity ($\chi$) can be used as a measure of the tendency of a molecule to retain its own electrons during donor/acceptor interactions that lead to corrosion inhibition. It is expected that a low value of $\chi$ will inform high inhibition performance. The results in Table 3.3.7 reveal that the order of increasing $\chi$ values is DHPC-3 < DHCP-2 < DHPC-1, which suggests highest inhibition efficiency for DHPC-3, and the trend is in agreement with the observed inhibition efficiency. The order of dipole moments of the studied inhibitors is DHPC-3 > DHPC-2 > DHPC-1, which is in agreement with the order of inhibition efficiency of the compounds and suggests that higher dipole moment favors higher inhibition potential. The enhanced inhibition performance of a molecule with a high dipole moment has been attributed to increased dipole-dipole interactions between the inhibitor molecule and charged metal surface [Sasikumar *et al.* (2015); Nooshabadi *et al.* (2015); Oguzie *et al.* (2010); Arab (2008)]. The trend of the values of $\Delta N$ for the studied compounds as listed in Table 3.3.7 is DHPC-3 > DHPC-2 > DHPC-1. This trend is also in agreement with the order of experimental inhibition efficiency of the

compounds. This observation implies that the tendency of a DHPC to inhibit metal corrosion is dependent on its ability to donate a high fraction of electrons to the metal. The values of $\Delta N$ in the present study are less than 3.6, which according to Lukovits's study [Lukovits *et al.* (2001)] suggest that the inhibition efficiency of DHPCs will increase with increasing electron-donating ability to the metal surface.

**Table 3.3.7:** Some relevant quantum chemical parameters of the studied compounds

| Compound | $E_{HOMO}$ (eV) | $E_{LUMO}$ (eV) | $\Delta E$ (eV) | $\chi$(eV) | $\mu$ (Debye) | $\Delta N$ |
|---|---|---|---|---|---|---|
| **DHPC-1** | -6.22 | -2.42 | 3.80 | 4.32 | 1.75 | 0.70 |
| **DHPC-2** | -5.86 | -1.15 | 4.71 | 3.50 | 4.31 | 0.74 |
| **DHPC-3** | -5.66 | -1.14 | 4.53 | 3.40 | 4.85 | 0.80 |

The electron density isosurfaces for $f^+$ and $f^-$ Fukui indices that correspond to nucleophilic and electrophilic attacks respectively are shown in Figure 3.3.9. The graphical representations of $f^+$ Fukui functions for the studied compounds show that the most susceptible sites of nucleophilic attacks in DHPC-1 are located on the $-NO_2$ substituent on the chromene ring and some neighboring C-atoms in the ring especially those that are adjacent to the electronegative O-atom in the chromene ring. The -C≡N substituent on the pyridine ring is also susceptible to nucleophilic attacks in all the three DHPCs.

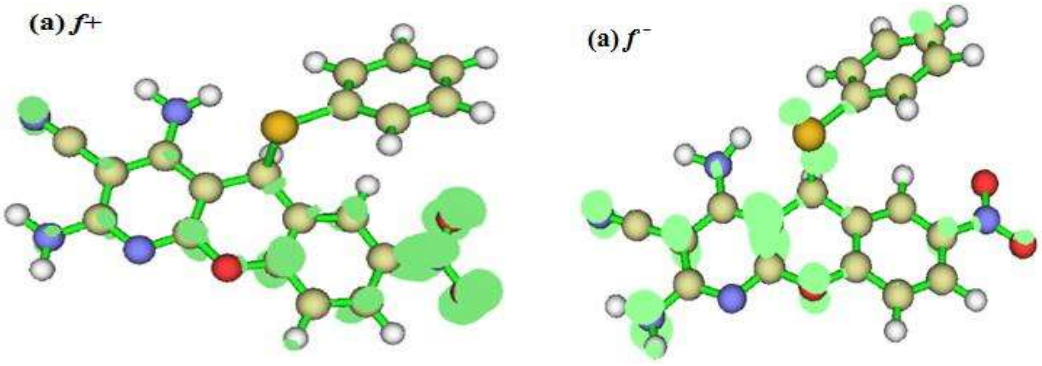

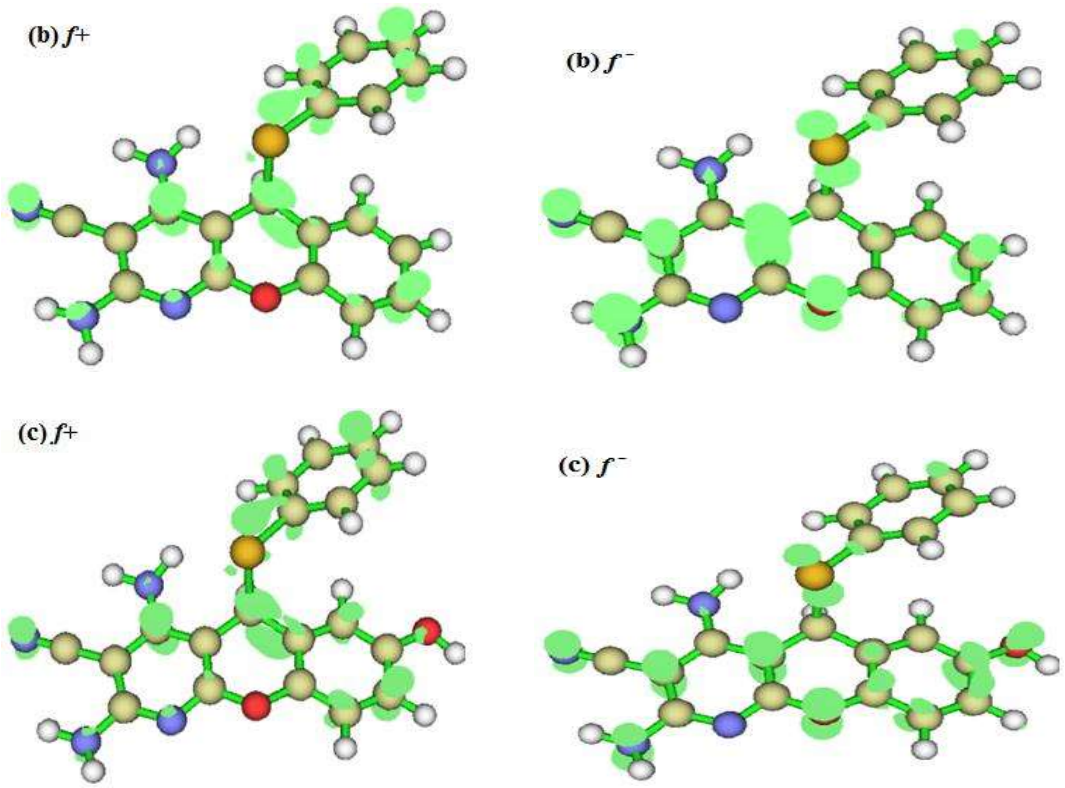


**Figure 3.3.9:** Fukui indices $f^+$ and $f^-$ corresponding to the atomics sites for the nucleophilic and electrophilic attacks respectively in (a) DHPC-1, (b) DHPC-2, and (c) DHPC-3 (*isosurface value = 0.003*).

The prospective sites of nucleophilic attacks in DHPC-2 and DHPC-3 include mainly the C-4 atom of the pyridine ring, the S-C region of the benzenethiolyl group, and the C-C region of the chromene ring adjacent to the benzenthiolyl group. The electron density distributions for the $f^-$ Fukui indices reveal that the sites of electrophilic attacks in the studied DHPCs include essentially the O-atom of the chromene ring, the N-atom of the $–NH_2$ substituent at the 2-position of the pyridine ring, the –N of the -C≡N substituent and the adjacent C-atom in the pyridine ring, the S-atom of the benzenthiolyl group, and the π-electron (C=C) region shared by the fused pyridine and chromene rings. The O-atom of the –OH substituent on chromene ring in DHPC-3 and the adjacent C=C region are also susceptible sites for electrophilic attack.

### 3.3.9. Molecular dynamics simulations studies

The adsorption behavior of the studied inhibitors on mild steel surface was also investigated using molecular dynamics simulation, which has emerged as a powerful tool to study the adsorption nature of the inhibitor molecule on metallic surface [Saha *et al.* (2015); Zhang *et al.* (2012)]. The molecular dynamics simulation has been used to describe the most favorable conformation of the adsorbed inhibitor molecule on the iron surface. Figure 3.3.10 represents the side and top views of the most stable adsorption models of (a) DHPC-1, (b) DHPC-2, and (c) DHPC-3 on Fe (110) surface using quench molecular dynamic and calculated parameters are listed in the Table 3.3.8. It is clear from Figure 3.3.10 that all the studied compounds adsorbed on the metallic surface by flat or parallel orientation, which suggests the strong interactions between the inhibitor molecules and Fe (110) surface. The values of interaction energy ($E_{\text{interaction}}$) for the studied inhibitors follow the order DHPC-3 > DHPC-2 > DHPC-1, which is agreement with the order of inhibition efficiency of the molecules. The high negative values of interaction energies suggest that the DHPCs spontaneously and strongly adsorb on Fe (110) surface [Sasikumar *et al.* (2015); Khaled and El-Maghraby (2014)]. The highest value of $E_{\text{interaction}}$ obtained for DHPC-3 among the studied inhibitors implies that it is most strongly adsorbed inhibitor on the metallic surface leading to highest inhibition efficiency. The trend of $E_{\text{interaction}}$ obtained for the studied compounds are in good agreement with the order of experimental inhibition efficiency. The values of binding energies ($E_{\text{binding}}$), which describe the strength of binding between inhibitor molecules and Fe (110) surface are in the order DHPC-3 > DHPC-2 > DHPC-1.

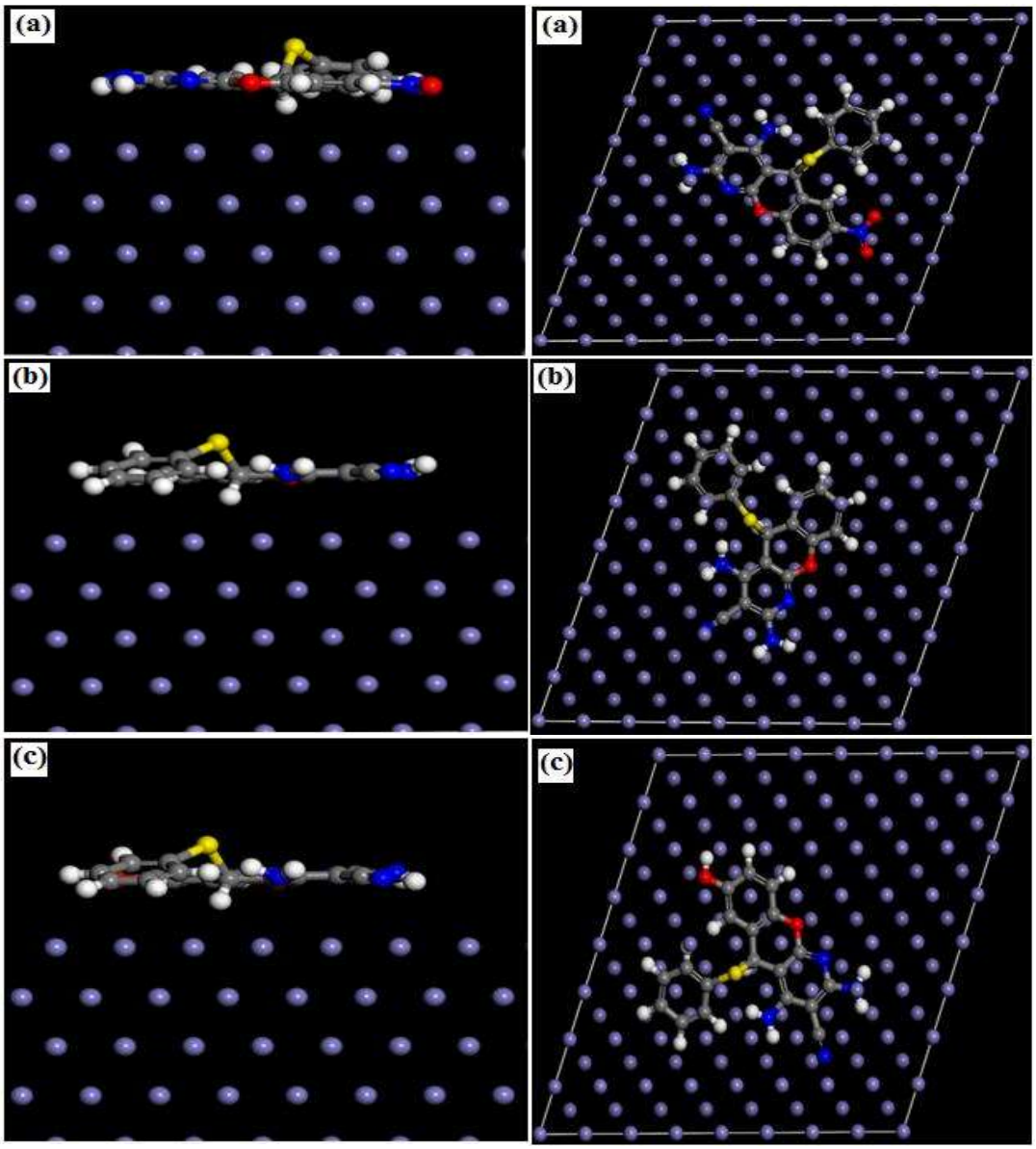


**Figure 3.3.10:** Side and top views of the most stable adsorption models of (a) DHPC-1, (b) DHPC-2, and (c) DHPC-3 on Fe (110) surface using quench molecular dynamic

The values of binding energies ($E_{binding}$) which describes the strength of binding between inhibitor molecules and Fe (110) surface also obeyed the order: DHPC-3 > DHPC-2 > DHPC-1. This finding suggests that DHPC-3 has maximum tendency to adsorb on mild steel surface which resulted in the maximum inhibition efficiency obtained for DHPC-3 [Khaled and El-Maghraby (2014); Khaled (2010); Verma *et al.* (2016a)].

**Table 3.3.8:** Interaction energies between the inhibitors and Fe (110) surface (kcal/mol)

| Systems | $E_{interaction}$ | $E_{binding}$ |
|---|---|---|
| **Fe (110) + DHPC-1** | -154.83 | 154.83 |
| **Fe (110) + DHPC-2** | -162.77 | 162.77 |
| **Fe (110) + DHPC-3** | -188.09 | 188.09 |

## 3.4. 3-amino alkylated indoles as corrosion inhibitors

Literature survey reveals that indole and its derivatives act as efficient metallic corrosion inhibitors in different electrolytic media [El-Shafei *et al.* (2004); Khaled (2008); Lowmunkhong *et al.* (2010); Lebrini *et al.* (2010); Quartarone *et al.* (2008)]. These compounds inhibit corrosion by getting adsorbed at the metal/ electrolyte interface through indole moiety which can acts as adsorption center. In the present study, the effect of the type of amine (opened chain or cyclic) as well as ring size of cyclic amine on the corrosion inhibition efficiency of three newly synthesized 3-amino alkylated indoles (AAIs) namely, N-((1H-indol-3-yl)(phenyl)methyl)-N-ethylethanamine (AAI-1), 3-(phenyl(pyrrolidin-1-yl)methyl)-1H-indole (AAI-2) and 3-(phenyl(piperidin-1-yl)methyl)-1H-indole (AAI-3) on mild steel corrosion in 1 M HCl solution has been investigated for the first time. The corrosion inhibition performances of the three newly synthesized AAIs were determined using weight loss, electrochemical impedance spectroscopy (EIS), potentiodynamic polarization, scanning electron microscopy (SEM), and atomic force microscopy (AFM) techniques. Quantum chemical calculations and molecular dynamics simulations studies were also carried out to provide more insights into the theoretical explanations of the inhibition activities of the studied compounds. IUPAC names, chemical structures, and abbreviations of the studied inhibitors are given in Table 3.4.1.

### 3.4.1. Gravimetric measurements

Table 3.4.2 represents the parameters derived from the weight loss experiments after 3 h immersion time in absence and presence different concentrations of the investigated inhibitors. It can be seen from the results that inhibition efficiency increases with increasing concentration of all inhibitors and maximum values of inhibition efficiencies of 94.34% for AAI-1, 96.08% for AAI-2 and 96.95% for AAI-3 were obtained at 0.862 mM concentration. However, careful examination of the results depicted in Table 3.4.2 showed

that very slight increase in the inhibition efficiency was observed on increasing inhibitors concentration from 0.689 mM to 0.862 mM suggesting that 0.689 mM is the optimum concentration. Increase in the inhibitors concentration resulted in the increased surface coverage which ultimately increases the inhibition efficiency. The higher inhibition efficiency of AAI-2 as compare to AAI-1 could be as a result of larger surface coverage by the pyrrolidine ring because of its ring structure present in AAI-2 as compare to its open chain structural analogues of AAI-1. While, the higher inhibition efficiency of AAI-3 as compare to AAI-2 can be explained on the basis of size of the heterocyclic rings. AAI-3 possesses piperdine ring which has comparatively larger molecular size and cover the larger surface area as compare to pyrrolidine ring present in the AAI-2 [Ebenso *et al.* (1999); Umoren and Gasem (2014)]. From these results it can be concluded that inhibition efficiency of 3-amino alkylated indoles (AAIs) increases on introducing the ring in the inhibitor molecule as well as on increasing the ring size (or decreasing the ring strain). The increased inhibition efficiency of the AAIs, with introducing the ring and increasing the length of hydrophobic carbon/alkyl chain is attributed due to repulsion between the non-polar hydrophobic chain and the polar water phase, which in turn force the AAIs to adsorb at metal and electrolyte interfaces in order to decrease that repulsion [Negm and Zaki (2008); Chen *et al.* (2015)]. Further, in presence of surface active molecules (inhibitors) in the solution cause distortion of the solvent liquids structure and thereby increase the free energy of the system. As a compromise, the AAIs concentrate at metal/ electrolyte interfaces because there, the thermodynamic best arrangement was possible.

**Table 3.4.1:** IUPAC names, molecular structures, and abbreviations data of studied AAIs

| S.No. | IUPAC name of Inhibitors | Chemical structure | Abbreviation |
|---|---|---|---|
| 1 | N-((1H-indol-3-yl)(phenyl)methyl)-N-ethylethanamine | 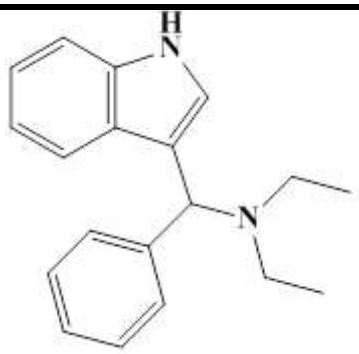 | **(AAI-1)** |
| 2 | 3-(phenyl(pyrrolidin-1-yl)methyl)-1H-indole | 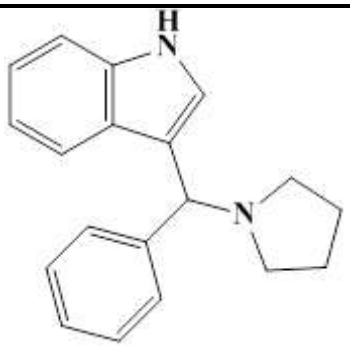 | **(AAI-2)** |
| 3 | 3-(phenyl(piperidin-1-yl)methyl)-1H-indole | 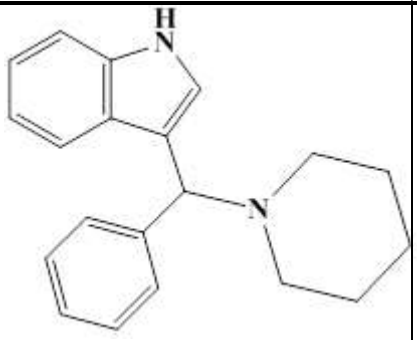 | **(AAI-3)** |

The AAIs adsorb on the metal/ electrolyte interface in such a way that polar part of the molecules oriented toward metallic surface leaving the nonpolar hydrophobic alkyl part into the solution which repel the aqueous corrosion fluid and thereby inhibit corrosion [Al-Sabagh *et al.* (2012); Cai *et al.* (2012); Mahmoud (2007)]. The molecular structure and IUPAC name of the inhibitors used are given in Table 3.1.1.

**Table 3.4.2:** The weight loss parameters obtained for mild steel in 1 M HCl containing different concentrations of AAIs

| inhibitor | Conc (mM) | Weight loss (mg) | $C_R$ (mg $cm^{-2}$ $h^{-1}$) | $\Theta$ | $\eta$% |
|---|---|---|---|---|---|
| **Blank** | 0.0 | 230 | 7.66 | --- | --- |
| | 0.172 | 91 | 3.033 | 0.6043 | 60.43 |
| | 0.345 | 37 | 1.233 | 0.8391 | 83.91 |
| | 0.517 | 21 | 0.700 | 0.9086 | 90.86 |
| | 0.689 | 14 | 0.466 | 0.9391 | 93.91 |
| | 0.862 | 13 | 0.433 | 0.9434 | 94.34 |
| **AAI-2** | 0.172 | 68 | 2.266 | 0.7043 | 70.43 |
| | 0.345 | 28 | 0.933 | 0.8782 | 87.82 |
| | 0.517 | 16 | 0.533 | 0.9304 | 93.04 |
| | 0.689 | 10 | 0.333 | 0.9565 | 95.65 |
| | 0.862 | 9 | 0.300 | 0.9608 | 96.08 |
| **AAI-3** | 0.172 | 58 | 1.933 | 0.7478 | 74.78 |
| | 0.345 | 25 | 0.833 | 0.8913 | 89.13 |
| | 0.517 | 13 | 0.433 | 0.9434 | 94.34 |
| | 0.689 | 8 | 0.266 | 0.9652 | 96.52 |
| | 0.862 | 7 | 0.233 | 0.9695 | 96.95 |

### 3.4.2. Effect of solution temperature

In order to study the effect of temperature on the corrosion inhibition efficiency of 3-amino alkylated indoles on mild steel corrosion in 1M HCl, the weight loss experiments were performed in absence and presence of optimum concentrations of the studied inhibitors at different temperature ranging from 308 to 338K. The values of corrosion rates ($C_R$) and percentage inhibition efficiency ($\eta$%) obtained at different temperature for studied inhibitors are given in the Table 3.4.3.

**Table 3.4.3:** Variation of $C_R$ and $\eta$ % with temperature in absence and presence of optimum concentration of AAIs in 1M HCl.

| Temperature (K) | Corrosion rate ($C_R$) (mg cm$^{-2}$ h$^{-1}$) and Inhibition efficiency ($\eta$%) | | | | | | | |
|---|---|---|---|---|---|---|---|---|
| | Blank | | AAI-1 | | AAI-2 | | AAI-3 | |
| | $C_R$ | $\eta$% | $C_R$ | $\eta$% | $C_R$ | $\eta$% | $C_R$ | $\eta$% |
| **308** | 7.66 | --- | 0.46 | 93.99 | 0.33 | 95.69 | 0.26 | 96.60 |
| **318** | 11.0 | --- | 1.30 | 88.81 | 1.00 | 90.90 | 0.80 | 92.72 |
| **328** | 14.3 | --- | 3.10 | 78.32 | 2.46 | 82.79 | 1.93 | 86.50 |
| **338** | 18.6 | --- | 6.50 | 65.05 | 5.43 | 70.80 | 4.86 | 73.87 |

It can be seen from the results that $\eta$% decreases and $C_R$ increases with increasing the solution temperature. The increased $C_R$ at elevated temperature might be attributed due to rapid etching, desorption and decomposition and/or rearrangement of the inhibitors molecules [Verma *et al.* (2015a)]. The temperature dependency of $C_R$ can be best represented by Arrhenius equation, where the natural logarithm of $C_R$ is a linear function of $1/T$ [Verma *et al.* (2015b)]: The activation energy for metallic corrosion is the minimum amount of energy that is required in order to produce the corrosion products, such as rust and scales [Murulana *et al.* (2015); Noor and Al-Moubaraki (2008)]. High values of $E_a$ are generally associated with low corrosion rates while low values of $E_a$ are associated with high corrosion rates.

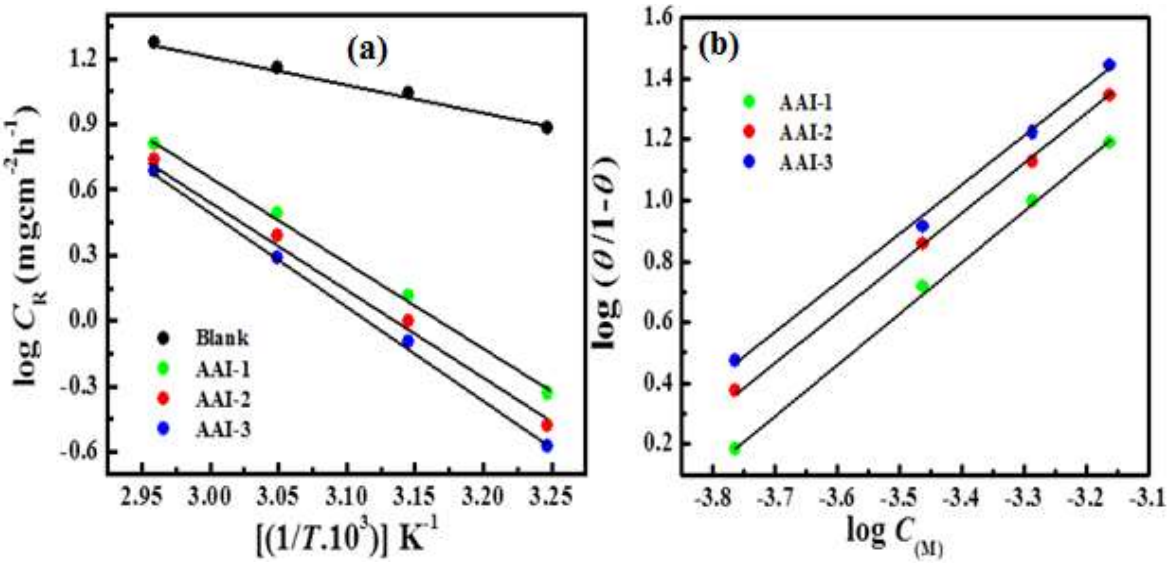


**Figure 3.4.1:** (a) Arrhenius plots of log $C_R$ vs. 1000/$T$ (b) Langmuir isotherm plot for the adsorption of the AAIs on mild steel surface in 1M HCl

Figure 3.4.1(a) represents the Arrhenius plots from the intercepts of which values of $E_a$ are calculated. The calculated values of $E_a$ were 76.072 kJmol$^{-1}$, 80.461 kJmol$^{-1}$ and 83.145 kJmol$^{-1}$ for AAI-1, AAI-2 and AAI-3, respectively. These results showed that values of $E_a$ are higher in presence of inhibitors as compare to in their absence (28.48 kJmol$^{-1}$). The increased values of $E_a$ in presence of AAIs suggest the physical adsorption that occurs during first stage of the adsorption processes. [Solmaz (2014a); Solmaz (2014b)]. However, it is well known that the adsorption behavior of most of the organic inhibitors involve both physical as well as chemical processes [Solmaz (2014a); Solmaz (2014b); [Ghareba and Omanovic (2010)]. Therefore, it is concluded that, the adsorption of these molecules on the mild steel surface from HCl solution takes place through both physical and chemical processes simultaneously with domination of physical one.

### 3.4.3. Adsorption isotherm

In order to understand the nature of adsorption of inhibitors on steel surface several isotherms such as Langmuir, Temkin and Frumkin etc. were tested. The Langmuir

isotherm gave the best fit as the numerical values of $R^2$ were close to unity for all studied inhibitors.

**Table 3.4.4:** The values of $K_{ads}$ and $\Delta G^{\circ}_{ads}$ for mild steel in absence and presence of optimum concentration of AAIs in 1M HCl at different studied temperature

| inhibitor | $K_{ads}$ ($10^4$ $M^{-1}$) | | | | $-\Delta G^{\circ}_{ads}$ (k J $mol^{-1}$) | | | |
|---|---|---|---|---|---|---|---|---|
| | 308 | 318 | 328 | 338 | 308 | 318 | 328 | 338 |
| **AAI-1** | 1.85 | 0.89 | 0.43 | 0.22 | 35.45 | 34.68 | 33.80 | 32.98 |
| **AAI-2** | 2.63 | 1.11 | 0.54 | 0.29 | 36.36 | 35.27 | 34.40 | 33.72 |
| **AAI-3** | 3.32 | 1.52 | 0.76 | 0.34 | 36.96 | 36.10 | 35.36 | 34.15 |

The values of surface coverage ($\theta$) obtained at different concentrations of the AAIs from weight loss experiments were used to obtain the Langmuir adsorption isotherm plots [Figure 3.4.a(b)]. The values of $K_{ads}$ and the standard free energy of adsorption ($\Delta G^0_{ads}$) were calculated by standard method described earlier [Hamdy, and El-Gendy (2013)]. The calculated values of $K_{ads}$ and $\Delta G^0_{ads}$ are given in Table 3.4.4. High values of $K_{ads}$ suggest that the adsorption of the AAIs on mild steel surface is strongly feasible [Fu *et al.* (2011)]. Previous, studies have shown that the value of $\Delta G^0_{ads}$ around -40 kJ $mol^{-1}$ or more negative supports (chemisorption) [Goulart *et al.* (2013); Amin and Ibrahim (2011)]. While the value of $\Delta G^0_{ads}$ around -20 kJ $mol^{-1}$ or less negative suggested electrostatic interaction between charged inhibitor molecule and metallic surface (physisorption) [Goulart *et al.* (2013); Amin and Ibrahim (2011)]. Results depicted in Table 3.4.4 showed that values of $\Delta G^0_{ads}$ in the present study at different temperatures vary from -32.98 to -36.96 kJ $mol^{-1}$ suggesting that adsorption of the AAIs on mild steel surface is a combination of chemisorption and physisorption [Amin *et al.* (2011); Bentiss *et al.* (2005)].

### 3.4.4. Potentiodynamic polarization study

Potentiodynamic polarization studies were carried out in the absence and presence of different concentrations of the investigated inhibitors in order to understand the process of anodic oxidative metallic dissolution and cathodic reductive hydrogen evolution.

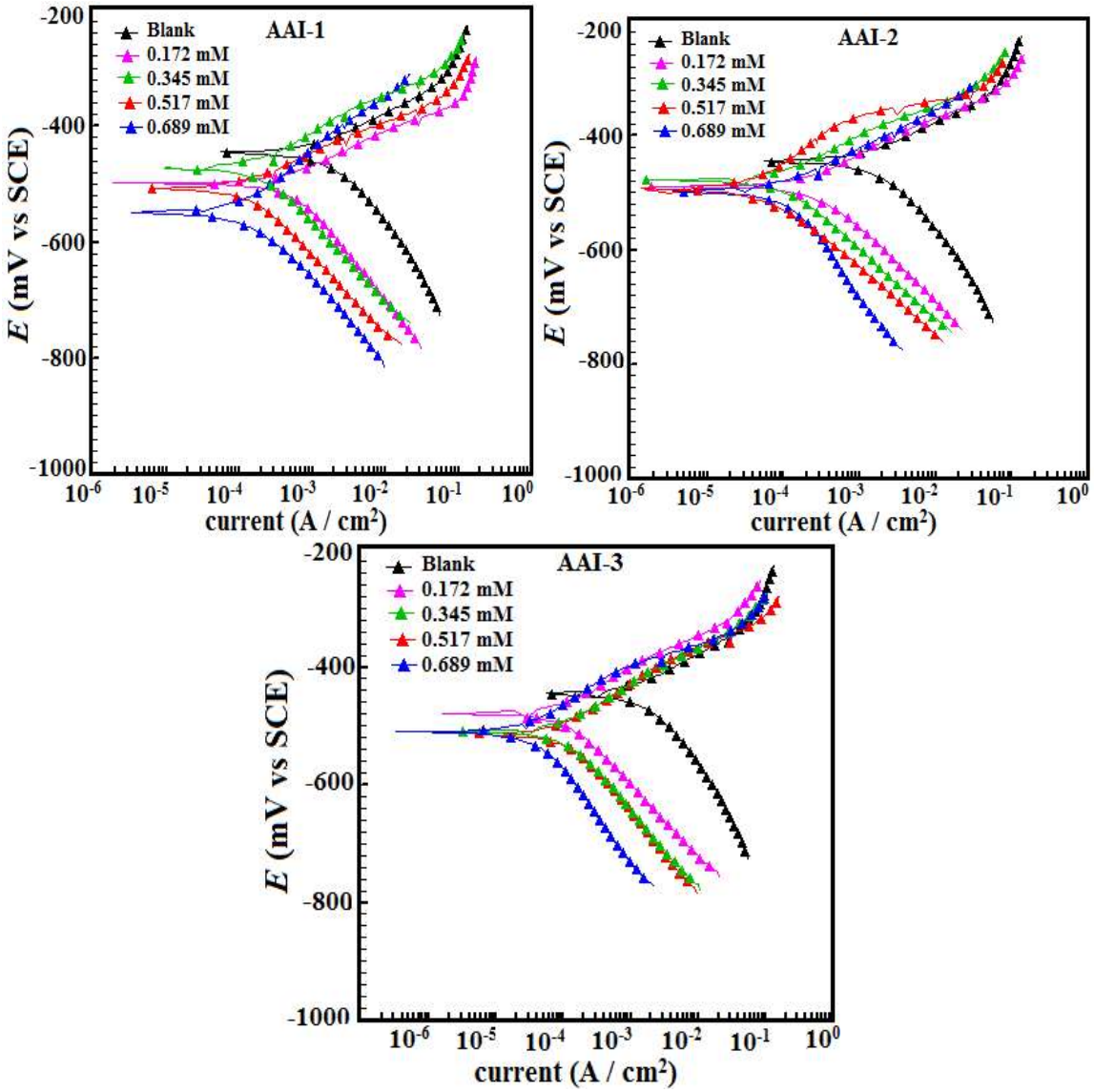


**Figure 3.4.2:** Polarization curves recorded for mild steel in the absence and presence of different concentrations of AAIs

The potentiodynamic polarization curves for mild steel in absence and presence inhibitors are shown in Figure 3.4.2. The values of potentiodynamic polarization

parameters such as corrosion potential ($E_{corr}$), corrosion current density ($i_{corr}$), anodic and cathodic Tafel slopes ($\beta_a$, $\beta_c$) were obtained from the polarization curves through extrapolation method and are included in Table 3.4.5. It can be seen from the results (Table 3.4.5 and Figure 3.4.2) that presence of AAIs significantly reduce the values of corrosion current densities for both anodic and cathodic half reactions. This finding indicates that inhibitors undertaken in the present study successfully inhibit both anodic oxidative dissolution of mild steel and cathodic reductive evolution of hydrogen [Zhao *et al.* (2015)]. The decreased values of $i_{corr}$ in presence of inhibitors are attributed due to blocking of the active centers present on the metallic surface [Bentiss *et al.* (2004)].

**Table 3.4.5:** Tafel polarization parameters for mild steel in 1 M HCl solution in absence and presence of different concentrations of AAIs.

| **Inhibitor** | **Conc (mM)** | **$E_{corr}$ (mV/SCE)** | **$\beta_a$ ($\mu A/cm^2$)** | **$\beta_c$ (mV/dec)** | **$i_{corr}$ (mV/dec)** | **$\eta$%** |
|---|---|---|---|---|---|---|
| **Blank** | --- | -445 | 70.5 | 114.6 | 1150 | ---- |
| **AAI-1** | 0.172 | -498 | 70.5 | 151.3 | 473.4 | 58.83 |
| | 0.345 | -472 | 72.6 | 99.2 | 201.7 | 82.46 |
| | 0.517 | -549 | 83.8 | 126.8 | 136.2 | 88.15 |
| | 0.689 | -508 | 66.7 | 125.3 | 85.6 | 92.55 |
| **AAI-2** | 0.172 | -489 | 79.8 | 107.5 | 332.8 | 71.06 |
| | 0.345 | -498 | 73.3 | 143.9 | 178.6 | 84.46 |
| | 0.517 | -479 | 71.6 | 100.9 | 96.0 | 91.65 |
| | 0.689 | -495 | 71.1 | 157.2 | 58.9 | 94.87 |
| **AAI-3** | 0.172 | -498 | 79.6 | 107.4 | 296.7 | 74.20 |
| | 0.345 | -496 | 74.1 | 88.1 | 146.2 | 87.28 |
| | 0.517 | -514 | 90.6 | 128.4 | 74.4 | 93.53 |
| | 0.689 | -410 | 75.2 | 108.3 | 25.5 | 97.78 |

It is obvious from the Figure 3.4.2 that in presence of inhibitors the corrosion potential shifted toward more negative direction. Further, it can be observed from the results shown in Table 3.4.5 that values of $\beta_c$ are more affected by inhibitors as compared to the values of $\beta_a$ when compared to the values of $\beta_a$ and $\beta_c$ of free acid solution indicating that investigated inhibitors act as predominantly cathodic type inhibitors [Verma *et al.* (2015d)].

### 3.4.5. Electrochemical impedance spectroscopy (EIS) study

The influence of the investigated compounds on the corrosion behaviour of mild steel in 1M HCl was also studied by EIS method.

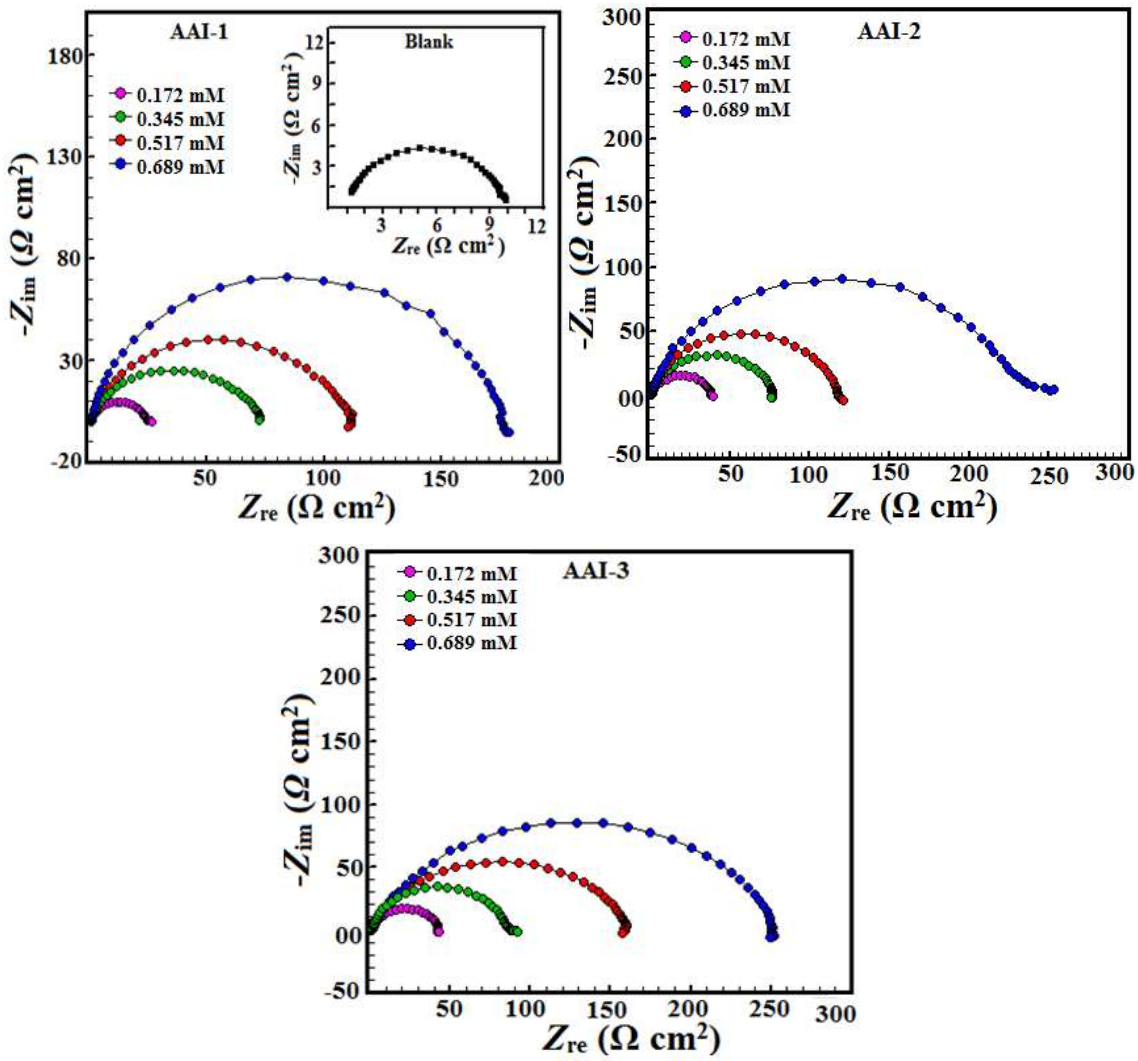


**Figure 3.4.3:** Nyquist plots recorded for mild steel in 1 M HCl in the absence and presence of different concentrations of AAIs

The Nyquist plots obtained from the EIS for mild steel in 1M HCl in without and with different concentrations of studied inhibitors is shown in Figure 3.4.3. Inspection of the Figure 3.4.3(a) show that the value of impedance modulus for uninhibited specimen was much smaller than that for inhibited specimen.

**Table 3.4.6:** EIS parameters obtained for mild steel in 1 M HCl in absence and presence of different concentrations of AAIs

| Inhibitor | Conc (mM) | $R_s$ ($\Omega$ cm$^2$) | $R_p$ ($\Omega$ cm$^2$) | $n$ | $Y_0$ ($\mu$F cm−2) | $C_{dl}$ ($\mu F$ cm$^{-2}$) | $\eta$% |
|---|---|---|---|---|---|---|---|
| **Blank** | --- | 1.12 | 10.7 | 0.827 | 482.2 | 106.21 | ---- |
| **AAI-1** | 0.172 | 0.796 | 24.73 | 0.846 | 140.3 | 53.58 | 56.73 |
| | 0.345 | 0.765 | 70.02 | 0.832 | 128.5 | 50.65 | 84.71 |
| | 0.517 | 1.059 | 107.0 | 0.848 | 108.3 | 44.19 | 90.00 |
| | 0.689 | 1.181 | 175.4 | 0.832 | 91.8 | 42.22 | 93.89 |
| **AAI-2** | 0.172 | 0.987 | 31.97 | 0.842 | 138.7 | 51.71 | 66.53 |
| | 0.345 | 0.743 | 75.89 | 0.843 | 115.8 | 48.41 | 85.90 |
| | 0.517 | 0.892 | 121.3 | 0.866 | 96.21 | 43.52 | 91.17 |
| | 0.689 | 0.811 | 234.3 | 0.845 | 84.3 | 41.07 | 95.43 |
| **AAI-3** | 0.172 | 0.810 | 41.72 | 0.839 | 131.8 | 48.25 | 74.35 |
| | 0.345 | 0.741 | 90.44 | 0.832 | 110.3 | 43.48 | 88.16 |
| | 0.517 | 0.696 | 155.5 | 0.829 | 87.8 | 32.16 | 93.11 |
| | 0.689 | 1.362 | 256.6 | 0.836 | 63.7 | 29.82 | 95.83 |

Further, it is also observed that the impedance modulus gradually increases with increasing the concentration of the inhibitors. It is also obvious from It is obvious from

Figure 3.4.3(a) that the Nyquist plot in absence of inhibitors shows a slightly depressed single semicircle capacitive loop and only one time constant was obtained in the Bode plots (single maxima in Bode plots). This finding suggests that corrosion of mild steel in acid solution in the absence of inhibitors is mainly controlled by charge transfer process [Ghareba and Omanovic (2010); Hamdy, and El-Gendy (2013)]. In the Nyquist plots, the difference in real impedance at lower and high frequencies is commonly considered as a charge transfer resistance ($R_{ct}$) [Roy *et al.* (2014); Solmaz *et al.* (2008); Ozcan et al. (2004)]. The charge transfer resistance must be corresponding to the resistance between metal and OHP (outer Helmholtz plane). And therefore, in the present investigation, the polarization resistance ($R_p$) which includes charge transfer resistance ($R_{ct}$), diffuse layer resistance ($R_d$), accumulation resistance ($R_a$), film resistance ($R_f$) etc. is taken into the account [Roy *et al.* (2014); Solmaz *et al.* (2008); Ozcan *et al.* (2004); Solmaz (2010); El Achouri *et al.* (2001)]. The circuit comprises of a constant phase elements (*CPE*), a charge transfer resistance ($R_p$) and a solution resistance ($R_s$). Generally, double layer formed by adsorption of inhibitors on the metallic surface behaves as CPE rather than pure capacitor and therefore, the capacitor was replaced by *CPE* to fit the semicircle impedance data more accurately [Yadav and Quraishi (2012); R. A. Bustamante *et al.* (2009)].

Figure 3.4.4 represents the Bode impedance and phase angle plots in absence and presence of different concentrations of the studied inhibitors. An ideal capacitor is characterized by a fixed value of slope (unity) and phase angle ($-90^0$) in Bode plot [Verma *et al.* (2016b); Ebenso *et al.* (2012b)]. The deviation from the ideal capacitive behavior can be attributed to the surface inhomogeneity of structural and interfacial origin. Generally, the value of phase angle increases with increasing the metal surface

smoothness. Careful visualization of the Bode plots shows that value of phase angle for free corroding specimen is much smaller (≈$40^0$) as compare to the values of phase angles for inhibited specimens. The increased values of phase angle in presence of different concentrations of the suggest that surface roughness of mild steel surface decreased due to formation of protective film by inhibitors [Verma *et al.* (2016b); Ebenso *et al.* (2012b)].

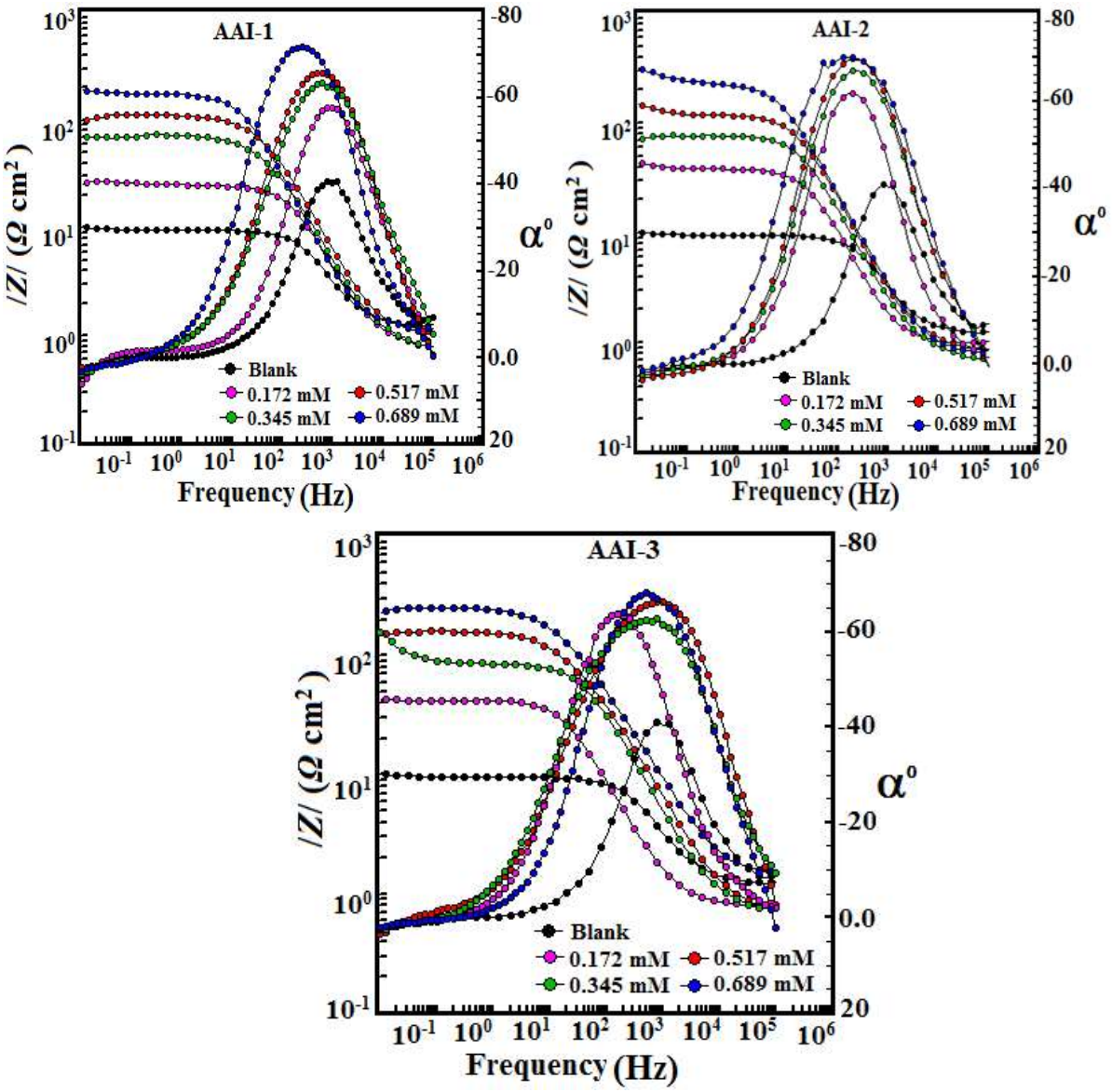

**Figure 3.4.4:** Bode impedance modulus ($\log f$ vs $\log |Z|$) and phase angle ($\log f$ vs $\alpha^0$) plots for mild steel in 1 M HCl in the absence and different of different concentrations of AAIs.

### 3.4.6. Scanning electron microscopy (SEM)

The adsorption of the AAIs on metallic surface was also supported by SEM analysis. The SEM images of mild steel specimens in absence and presence of optimum concentrations of the studied inhibitors after 3h immersion time are given in Figure 3.4.5.

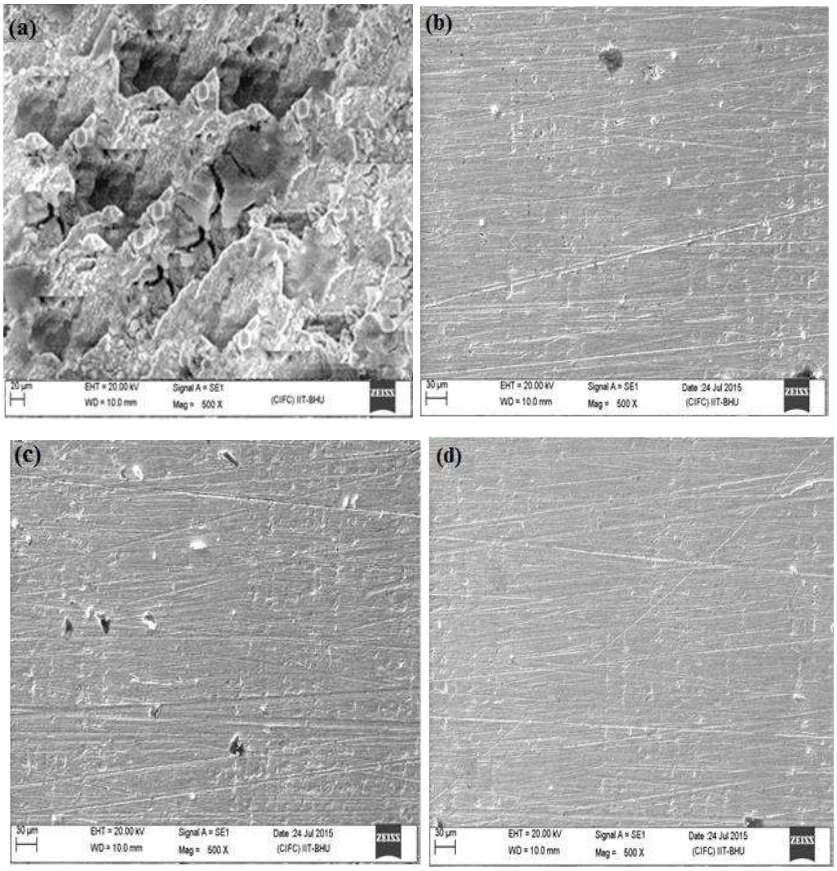


**Figure 3.4.5:** SEM images of mild steel surfaces in 1 M HCl in the absence of AAIs (a), and in 1 M HCl in the presence of optimum concentration of AAI-1 (b), AAI-2 and (c), AAI-3(d)

It can be seen that SEM micrograph of mild steel in absence of inhibitors [Figure 3.4.5(a)] is more corroded and damaged showing Mountain like appearance due to free acid corrosion in absence of inhibitors. However, in presence of optimum concentrations of inhibitors [Figure 3.4.5(b-d)], the SEM micrographs show very remarkable change in

the surface morphologies. The increased surface smoothness in presence of inhibitors is attributed due to adsorption of inhibitors on the metallic surfaces.

### 3.4.7. Atomic force microscopy (AFM) study

Figure 3.4.6 shows the three dimensional views of the mild steel surfaces in the absence and presence of optimum concentration of each of the three studied inhibitors.

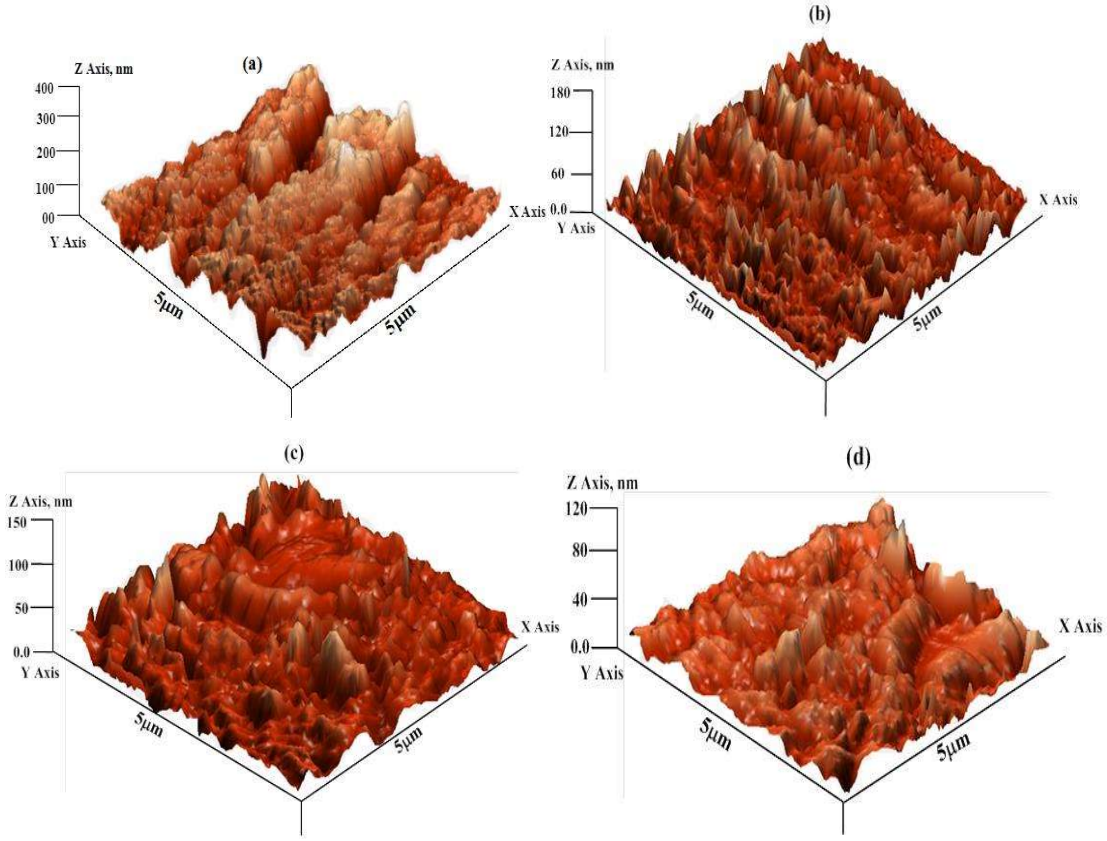


**Figure 3.4.6:** AFM images of mild steel surfaces in 1 M HCl in the absence of AAIs (a), and in 1 M HCl in the containing optimum concentration of AAI-1 (b), AAI-2 and (c), AAI-3(d).

Figure 3.4.6(a), which is highly corroded, rough, and inhomogeneous depicts the surface of mild steel retrieved from the uninhibited acid solution. The calculated average surface roughness of the uninhibited mild steel specimen was 392 nm. However, in the presence of optimum concentration of studied inhibitors, surface morphology of mild

steel specimens from the inhibitors containing aggressive media [Figure 3.4.6(5b-d)] remarkably improved owing to the formation of protective film on the surface. The calculated average surface roughnesses were 176, 143, and 118 nm in the presence of optimum concentration of AAI-1, AAI-2and AAI-3, respectively. The increased surface smoothness further suggested the formation of protective film of the inhibitors molecules on the steel surface, which prevents the metal from aggressive (direct) acid attack.

### 3.4.8. Quantum chemical calculations

The optimized molecular structures and the corresponding HOMO and LUMO electron density surfaces of the studied compounds are shown in Figures 3.4.7 and 3.4.8. The electron distribution of HOMO gives information about the centers or the sites that are most likely to donate the electrons to the corresponding orbital of the acceptor molecule, whereas the electron distribution of the LUMO provides information about the centers of the molecule that are more likely to accept the electron from an appropriate donor molecule. Figure 3.4.8 shows that the electron density of the HOMO mainly localized only over the indole rings in the AAI-1 and AAI-2, while for AAI-3 the electron density localized over the indole as well as phenyl rings. From the frontier molecular electron distribution it can be seen that as compare to AAI-1 and AAI-2, the involvement of the phenyl ring of AAI-3 helps in a greater electron transfer and therefore could adsorb more effectively on steel. The diethylamine and pyrrolidine residues of AAI-1 and AAI-2, respectively makes small contributions to the LUMO, as the electron density mainly localized over indole and phenyl rings. While the effectiveness of AAI-3 is due to the fact that piperdine ring make huge contribution to LUMO distribution.

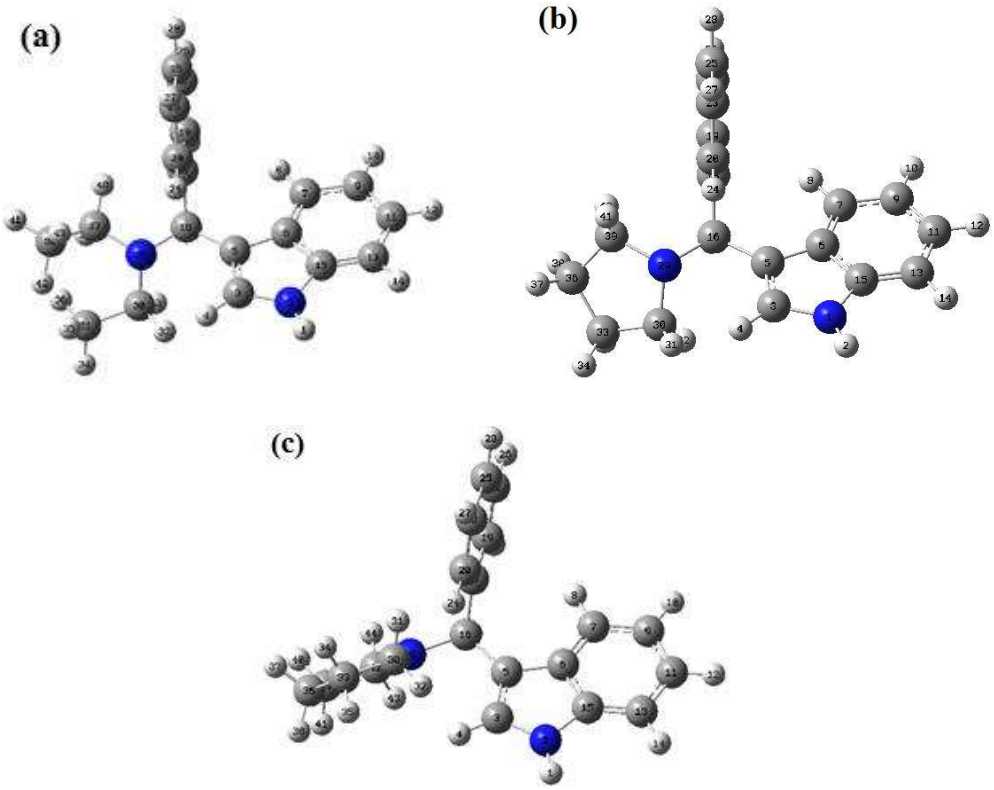


**Figure 3.4.7:** Optimized molecular structures of studied AAIs, (a) AAI-1, (b) AAI-2 and (c) AAI-3

The calculated values of some common quantum chemical calculations parameters are listed in Table 3.4.7. On the basis of earlier reports available in the literature it can be concluded that the value of $E_{HOMO}$ of a molecule is a measure of the tendency to donate its HOMO electrons to the corresponding acceptor molecule [Verma *et al.* (2015b); Saha *et al.* (2015)]. The value of $E_{HOMO}$ of the studied compounds follows the order: AAI-3 > AAI-2 > AAI-1, which is in accordance with the order of inhibition efficiency obtained experimentally. On the other hand, the $E_{LUMO}$ is a parameter that defines the affinity of molecule to accept electrons into its LUMO from appropriate donor molecule [Verma *et al.* (2015b); Saha *et al.* (2015)].

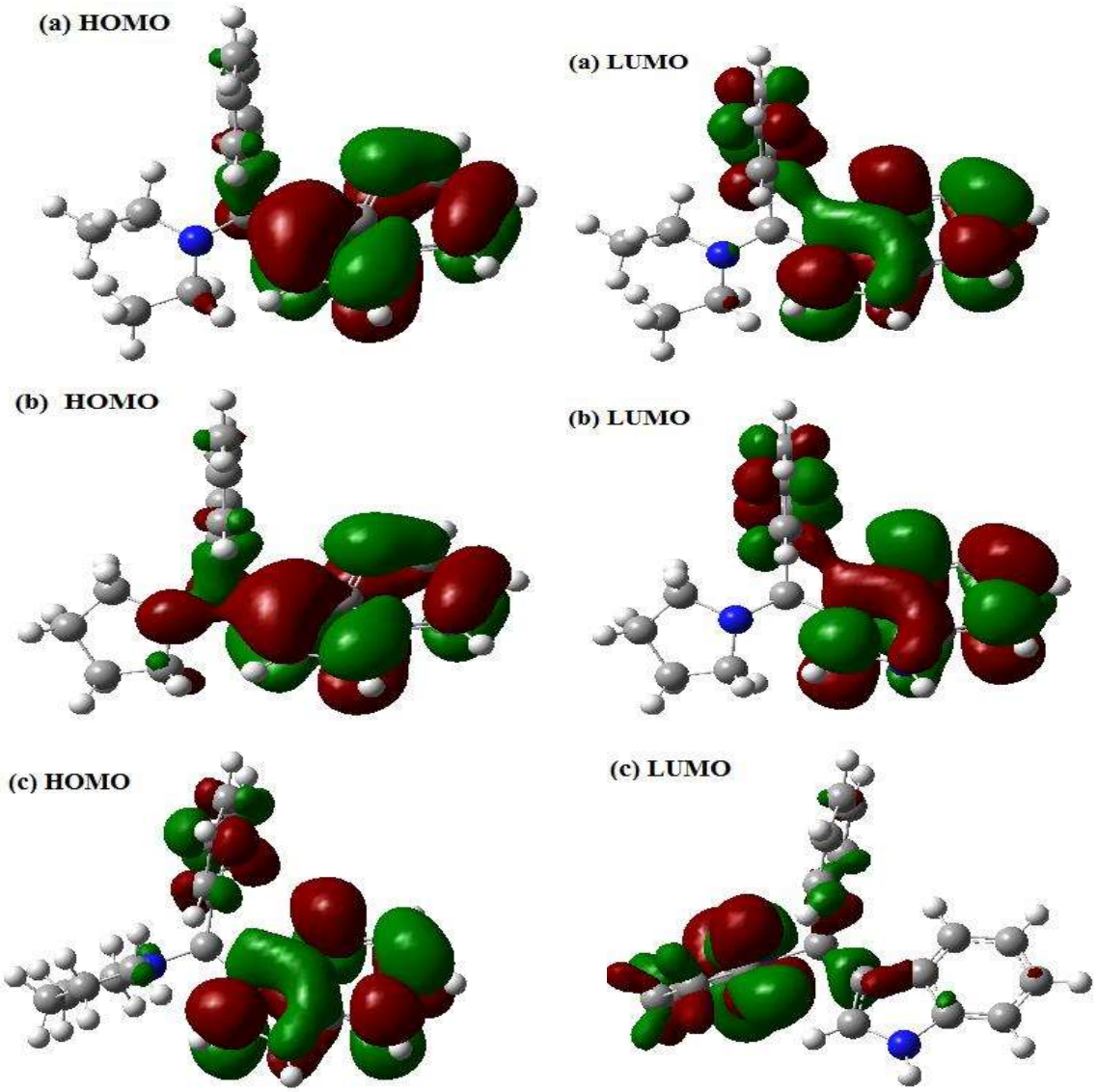


**Figure 3.4.8:** The frontier molecular orbital (left-hand side: HOMO; and right-hand side: LUMO) of the studied APQDs (a) AAI-1 (b) AAI-2 and (c) AAI-3.

The energy gap $\Delta E$ ($E_{LUMO}$-$E_{HOMO}$) is another very important parameter which can be used to predict the reactivity of molecules. Generally a molecule with low value of $\Delta E$ associated with high chemical reactivity and therefore high inhibition efficiency [Verma *et al.* (2015c); Herrag *et al.* (2010)]. The trends of the $\Delta E$ obtained in the present study for investigated inhibitors are in good agreement with the order of experimental inhibition efficiencies. The global electronegativity ($\chi$) is another important reactivity parameter that can be utilized to explain the electron holding capacity of the molecule.

Generally, higher value of $\chi$ is consistent with low electron transfer by the molecule and therefore low inhibition efficiency. In our present study, the values of $\chi$ obey the order (Table 3.4.7): AAI-1 > AAI-2 > AAI-3, which indicates that AAI-1 has lowest and AAI-3 has highest tendency of electrons donation to the appropriate acceptor (Fe) molecule. Further, inspection of the tabulated data show that the values of $\chi$ decreases with increasing the softness ($\sigma$) and decreasing the hardness ($\eta$) of the inhibitors molecules. And therefore it can be concluded that electrons donation from inhibitors to metal increases with increasing the softness and decreases with increasing the hardness of the inhibitors. The values of the fraction of electron transferred ($\Delta N$) form inhibitors to the metal were calculated and listed in Table 3.4.7 for all studied inhibitors. In the present case the $\Delta N$ values obey the order: AAI-3 > AAI-2 > AAI-1, which suggests that the maximum fraction of electron transfer occur in case of AAI-3 which the lowest fraction of electrons transfer occur in case of AAI-1 among the studied inhibitors suggesting that AAI-3 would absorb most effectively on steel surface. The entire quantum chemical calculations results show that corrosion inhibition in the present study occur via electron transfer from high electron density of the inhibitors to the surface Fe atoms.

**Table 3.4.7:** Quantum chemical parameters derived from the B3LYP/6-31+G(d,p) method

| **Inhibitors↓** | $\mu$ **(Debye)** | $E_{HOMO}$ **(eV)** | $E_{LUMO}$ **(eV)** | $\Delta E$ **(eV)** | $\eta$ **(eV)** | $\Sigma$ **(eV)** | $\chi$ **(eV)** | $\Delta N$ |
|---|---|---|---|---|---|---|---|---|
| **AAI-1** | 1.6927 | -8.574 | -5.121 | 3.453 | 1.726 | 0.579 | 6.848 | 0.043 |
| **AAI-2** | 1.9680 | -8.562 | -5.112 | 3.450 | 1.725 | 0.579 | 6.837 | 0.047 |
| **AAI-3** | 2.3671 | -7.803 | -5.123 | 2.680 | 1.335 | 0.749 | 6.463 | 0.200 |

### 3.4.9. Molecular dynamics simulations

Recently, MD simulation has emerged as an indispensable tool in the characterization of the adsorption behavior of the inhibitor molecules on the metallic surface [Xu *et al.* (2014)]. MD simulations can reasonably provide information of the most favorable configuration of adsorbed inhibitor molecule on the metal surface and have become a well-established tool in computational chemistry. In our present paper, MD simulations were carried out to study the adsorption characteristics of investigated inhibitors on the Fe (110) surface. The equilibrium configurations for all inhibitors are represented in Figure 3.4.9. Careful inspection of the Figure 3.4.9 shows that during the MD simulation process, the AAIs moved gradually near the Fe (110) surface with almost flat orientation. And, therefore it has been concluded that investigated inhibitors can be adsorbed on the mild steel surface through the phenyl and indole rings moieties. Furthermore, it has been reported that empty d-orbitals of the surface Fe atoms can facilitate the adsorption process by accepting the electrons from the inhibitors molecules. In the studied compounds, the nonbonding electrons of the N atoms and π- electrons of the indole and phenyl moieties provide sufficient electronic density to transfer in the empty d-orbitals of the surface Fe atoms in order to form a stable coordinate bond. Generally, the adsorption energy is the energy released (or needed) when the relaxed adsorbate component is adsorbed on the substrate. The values of interaction energy ($E_{\text{interaction}}$) and binding energy ($E_{\text{binding}}$) between studied inhibitors and Fe (110) surface were evaluated when systems reach equilibrium. It can be seen from Table 3.4.8 that values of $E_{\text{Fe-AAIs}}$ ($E_{\text{interaction}}$) are negative for all studied inhibitors which suggest that adsorption of these compounds on Fe (110) surface can take place spontaneously [John et al. (2011); Caleyo *et al.* (2009)].

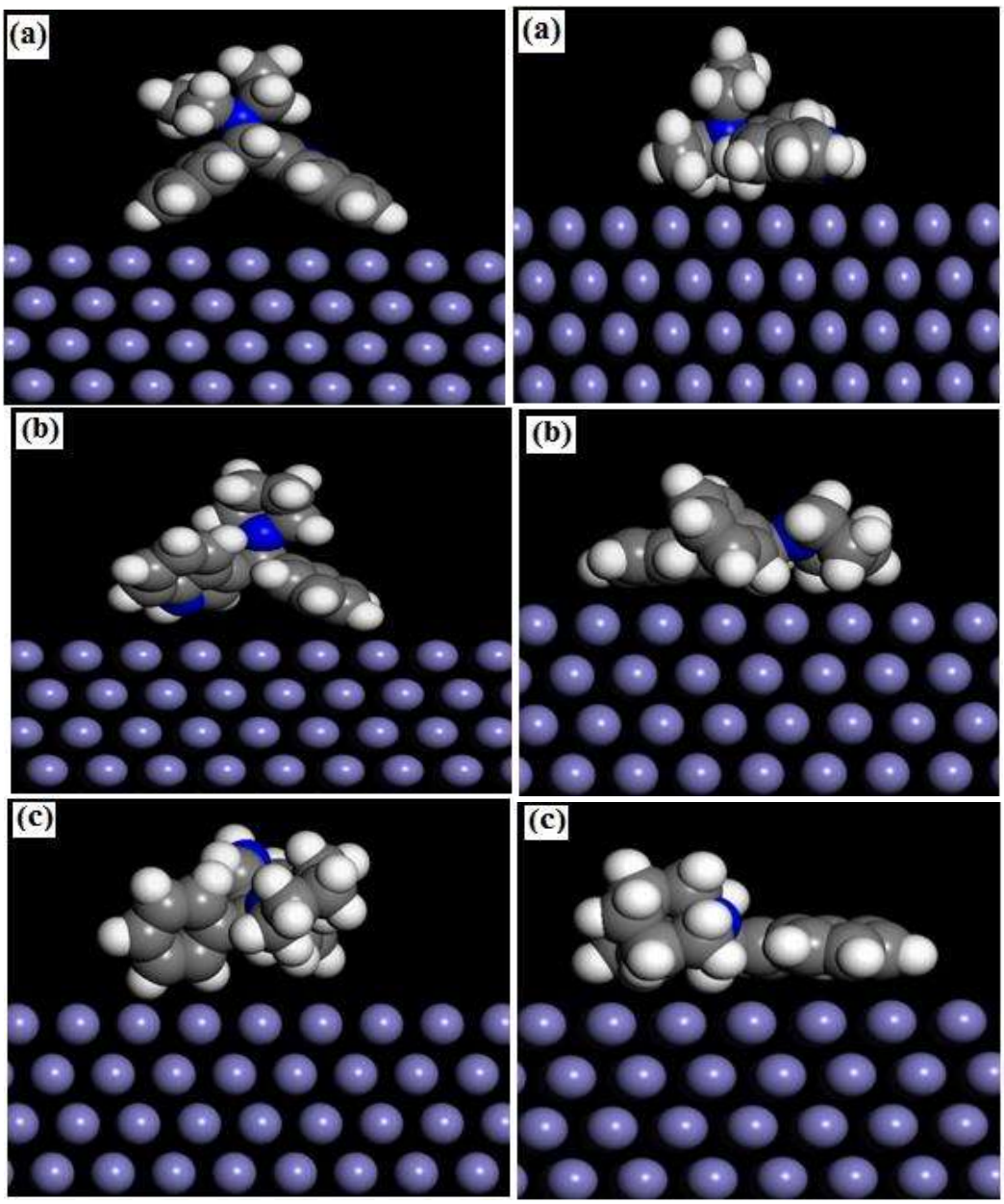


**Figure 3.4.9:** Side view equilibrium adsorption of AAI-1, AAI-2, and AAI-3 on Fe (110) surface (left hand side: before; and right hand side: after molecular dynamics simulations)

Moreover, it can also be observed from the results that AAI-3 has maximum negative value of $E_{interaction}$ suggesting that it can be adsorbed on Fe surface most strongly and most efficiently and possess better inhibition efficiency among the studied inhibitors [John et al. (2011); Caleyo *et al.* (2009)]. The value of the binding energies ($E_{binding}$) for different studied inhibitors follows the order: AAI-3 > AAI-2 > AAI-1, which is in accordance with order of their inhibition efficiencies obtained experimentally.

**Table 3.4.8:** Interaction energies between the inhibitors and Fe (110) surface (Kcal/mol)

| Inhibitor | $E_{binding}$ | $E_{interaction}$ ($-E_{binding}$) |
|---|---|---|
| **AAI-1** | 137.53 | -137.53 |
| **AAI-2** | 142.79 | -142.79 |
| **AAI-3** | 144.82 | -144.82 |